Synthesis and Application of Graphene Decorated Nanocomposites for Photovoltaics and Printed Electronics

by

Nasim Bakhshi Zadeh

A thesis
presented to the University of Waterloo
in fulfillment of the
thesis requirement for the degree of
Doctor of Philosophy
in
Electrical and Computer Engineering

Waterloo, Ontario, Canada, 2019

AUTHOR'S DECLARATION

I hereby declare that I am the sole author of this thesis. This is a true copy of the thesis, including any required final revisions, as accepted by my examiners.

I understand that my thesis may be made electronically available to the public.

Abstract

Improving the yield performance of commercial solar cells has been a major topic of interest for many research studies as different processing parameters are extensively explored. Screen printing metallization is the most widely-used technique to form the metallic contacts in commercial silicon solar cells. Among various process parameters in screen printing technology, firing step is considered to be a major cost-determining stage as a high amount of thermal budget is consumed during high temperature sintering process. Bending of the cell (deflection) due to residual stress produced in firing step is also considered as a very serious problem for reliability of the module. Another important concern in conventional metallic pastes used in screen printing technique is the presence of lead which is not an environmentally friendly material.

Lead free Electrically Conductive Adhesives (ECAs) which have been of particular interest in electronic packaging applications are considered as an interesting alternative and their possibility to replace conventional metallic pastes in screen printing technology is systematically investigated in this research. In addition to be environmentally friendly, ECAs provide low processing temperature which is beneficial for developing ultra-thin solar cells, decreasing cost and increasing the yield performance of the solar cells.

After establishing the screen printing process to print conductive materials, different conductive nanocomposites were synthesized using ECA and silver nanowires. Conductivity measurements revealed that addition of even a very small amount of silver nanowires could improve the conductivity of the nanocomposite for around 70%. Morphology characterization analysis confirmed the influence of silver nanowires in improving the electrical properties of the paste by tunneling effect. Despite the significant improvement in conductivity of the nanocomposite which made it an appealing alternative for printed electronics, its conductivity was still lower than the conventional metallic pastes used in the solar cell fabrication. To reach a comparable conductivity, two dimensional graphene sheets that have outstanding electrical and structural properties were used. Material synthesis and curing profile are optimized to improve the electrical property of the developed nanocomposites which resulted in the highest boost in conductivity, over 2 orders of magnitude of ECA. Different characterization techniques were utilized to study the curing kinetics and thermal stability of the developed materials.

A detailed residual stress analysis was also conducted on all developed nanocomposites as well as the metallic paste printed substrates and results revealed that the amount of residual stress induced in substrates was one order of magnitude lower in nanocomposite printed wafers in comparison with the metallic printed ones. Also, the amount of increase in residual stress by decreasing the wafer thickness was small in the case of using nanocomposite paste. It was also shown that the amount of bending increased with decreasing the thickness of substrate in all samples; however, it was much lower in nanocomposite printed wafers confirming that the developed nanocomposites could be a promising alternative in screen printing metallization of ultra-thin wafers.

Effective Work Function (EWF) was introduced for the multi-phase nanocomposite being used as electrodes in electronic devices. Based on the theoretical studies on tunneling phenomenon and the potential barrier height measurement analysis on MOS devices, IV method was illustrated and used for the first time to measure the EWF of the multi-phase graphene-decorated nanocomposite. The results were verified using two other techniques: UPS spectroscopy and TLM. The results from all measurements were in reasonable agreement confirming the accuracy of results obtained from all three methods. However the existing small difference between the EWF values was attributed to the heterogeneous nature of the nanocomposite at the interface confirming the necessity of using the effective work function definition.

Finally, highly conductive graphene-decorated nanocomposite as well as the evaporated Al were used as the back contact of two solar cells. Solar cells were fabricated and characterized using different techniques. Quantum efficiency, illuminated IV and Dark IV results from both cells were in an excellent agreement with each. In general, the obtained close performance results as well as the equal obtained efficiencies for both cells confirmed a very satisfactory achievement for a standard technology baseline development.

Acknowledgements

I would like to thank my advisor, Professor Siva Sivoththaman for trusting me and believing in me even though I came from a different technical background. I deeply appreciate him for understanding my situation while I was working off campus for the past 4 years. His guidance and support through all these years helped me accomplishing this research work.

I would also like to offer my thanks to the members of my dissertation committee, Professor Aziz, Professor Wen, Professor Jayaram, and Professor Kherani for their constructive questions and suggestions that all helped elevate the quality of this work.

I would like to thank all my colleagues for all their help and support especially Dr. Roohen Tarighat for his helps and advice on my research.

Dedication

To my best friend, my love and my husband, Ali for his patience, pure love and endless support.

To my dear brother, my inspiration, Amin.

To my sisters and my soul mates, Shadi Taghavi and Negar Rasti.

To my beloved parents for their prayers, love and support which has always got me through in my deepest and darkest moments. They are indeed the reason of what I become today.

Table of Contents

List of Figures

List of Tables

List of Acronyms

A_o	fractional open area in the screen
A_c	area of the contact which is covered by the thin film
A^*	effective Richardson constant
ACA	anisotropic conductive adhesives
α_t	thermal coefficient of expansion of Si
α_b	thermal coefficient of expansion of conductive film
ARC	antireflection coating
BSF	back surface field
D	diameter of the contact spot
δ	cell deflection (bending)
d_i	distance between contacts
DSC	differential scanning calorimetry
EB_{Max}	maximum measured binding energy (secondary electron cut-off)
EB_{Min}	minimum measured binding energy
ECA	electrical conductive adhesive
$E_{g,Si}$	silicon band gap
EH	electron-hole
EWF	effective work function
E_t	elastic modules of Si
E_b	elastic modules of conductive film
ε_s	semiconductor permittivity
FF	fill factor
H	cell thickness
h	conductive film thickness
h	plank's constant
hv	photon energy that bombards the sample
ICA	isotropic conductive adhesives
IV	current-voltage
K	Boltzmann constant
L	cell length
L_T	transfer length
m^*	electron effective mass
N	doping concentration
NCOMP-GN-Cell	cell with graphene nanocomposite back contact

NCOMP-1wt%GN	nanocomposite with 1wt% of graphene
NCOMP-0.05WT%AG	nanocomposite with 0.05wt% of silver nanowires cured for 10 mins
NCOMP-0.05wt%Ag-2	nanocomposite with 0.05wt% of silver nanowires cured for 60 mins
NCOMP-0.1WT%AG	nanocomposite with 0.1wt% of silver nanowires cured for 10 mins
NCOMP-0.1wt%Ag-2	nanocomposite with 0.1wt% of silver nanowires cured for 60 mins
NCOMP-1wt%GN	nanocomposite with 1wt% of graphene
NCOMP-3wt%GN	nanocomposite with 3wt% of graphene
NCOS	nanocomposite-oxide-semiconductor
R_{cr}	constriction resistance between conductive fillers
R_t	tunneling resistance between conductive fillers
R_{total}	total resistance of ecas
ρ_i	intrinsic filler resistivity
ρ_t	tunneling resistivity
Ref-Cell	reference cell with al back contact
R_{ti}	total resistance between contact i and i+1
R_{sh}	sheet resistance of the n-layer
R_C	contact resistance between the contact and the n-layer
ρ_c	specific contact resistance
t_w	the maximum wet thickness of the screen printed material
t_m	mesh thickness in the screen
t_e	emulsion build-up thickness in the screen
T_f	firing temperature
T_m	ambient temperature
ψ_{bs}	barrier height at the interface between composite and semiconductor
ψ_b	barrier height at the interface between composite and oxide
u_f	distance between fermi level and band edge
WF	work function
X_{ox}	electron affinity of the oxide
X_{si}	electron affinity of silicon

Chapter 1

Introduction and Motivations

1.1 Crystalline Silicon Based Solar cell Technology

Since 1839 that Alexandre-Edmond Becquerel first observed the photovoltaic (PV) effect 0, crystalline silicon (c-Si) is proved to be the best energy source to replace fossil fuels due to its long term sustainability, being more environmentally friendly and its lower cost compared to the other solar cell technologies shown in Fig. 1.1[2-4].

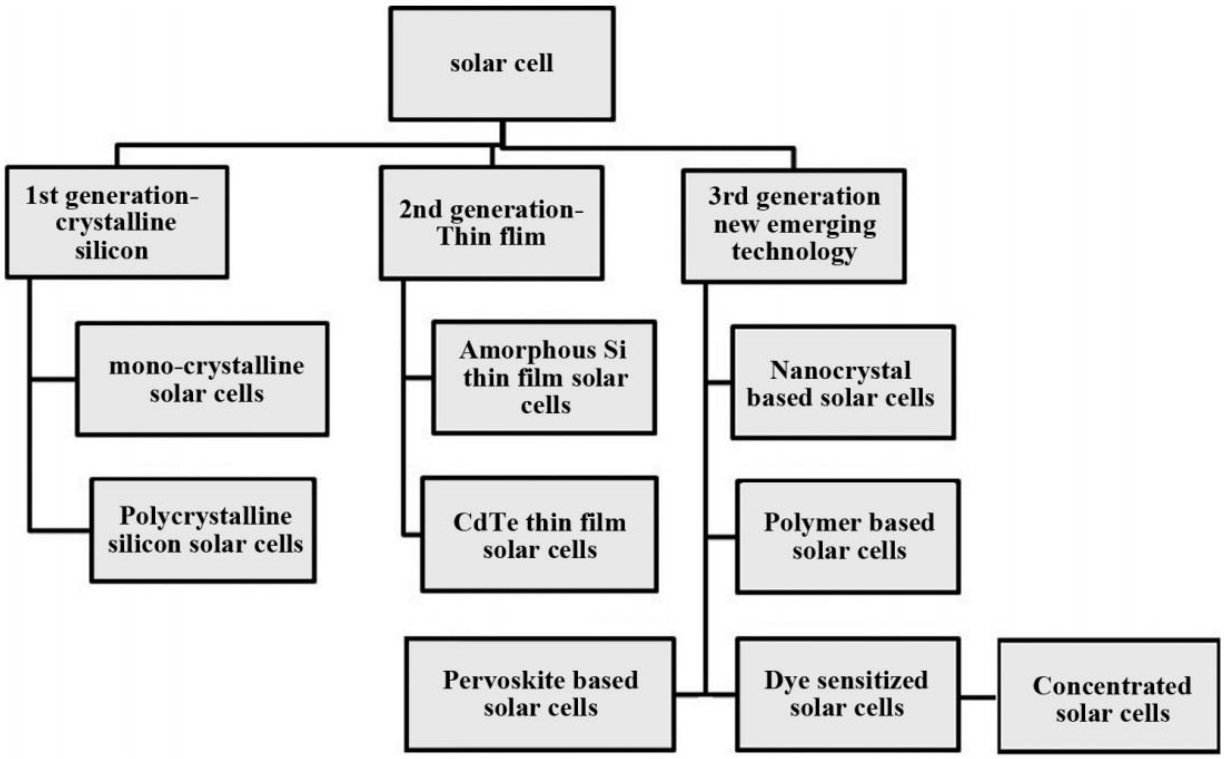

Fig 1.1: Different types of solar cell technologies[2]

Photovoltaic (PV) market has grown almost exponentially in the last 15 years and as shown in Fig.1.2 (a), the estimated global growth of cumulative PV capacity is going to reach 650 GW in 2019 [5]. The worldwide growth of the PV industry and the fact that crystalline silicon based photovoltaics dominate more than 90% of this market (Fig. 1.2(b)) reflect the importance of this

technology among the others. The main driving force in scientific and industrial developments of Silicon photovoltaics has been reducing the cost to be able to compete with fossil fuels. Fortunately, there has been a big cost reduction due to significant advances in conventional crystalline silicon solar industry. The average prices reported in August 2018 were around $0.13 per watt while in 1977 prices for c-Si cells were about $77 per watt [5].

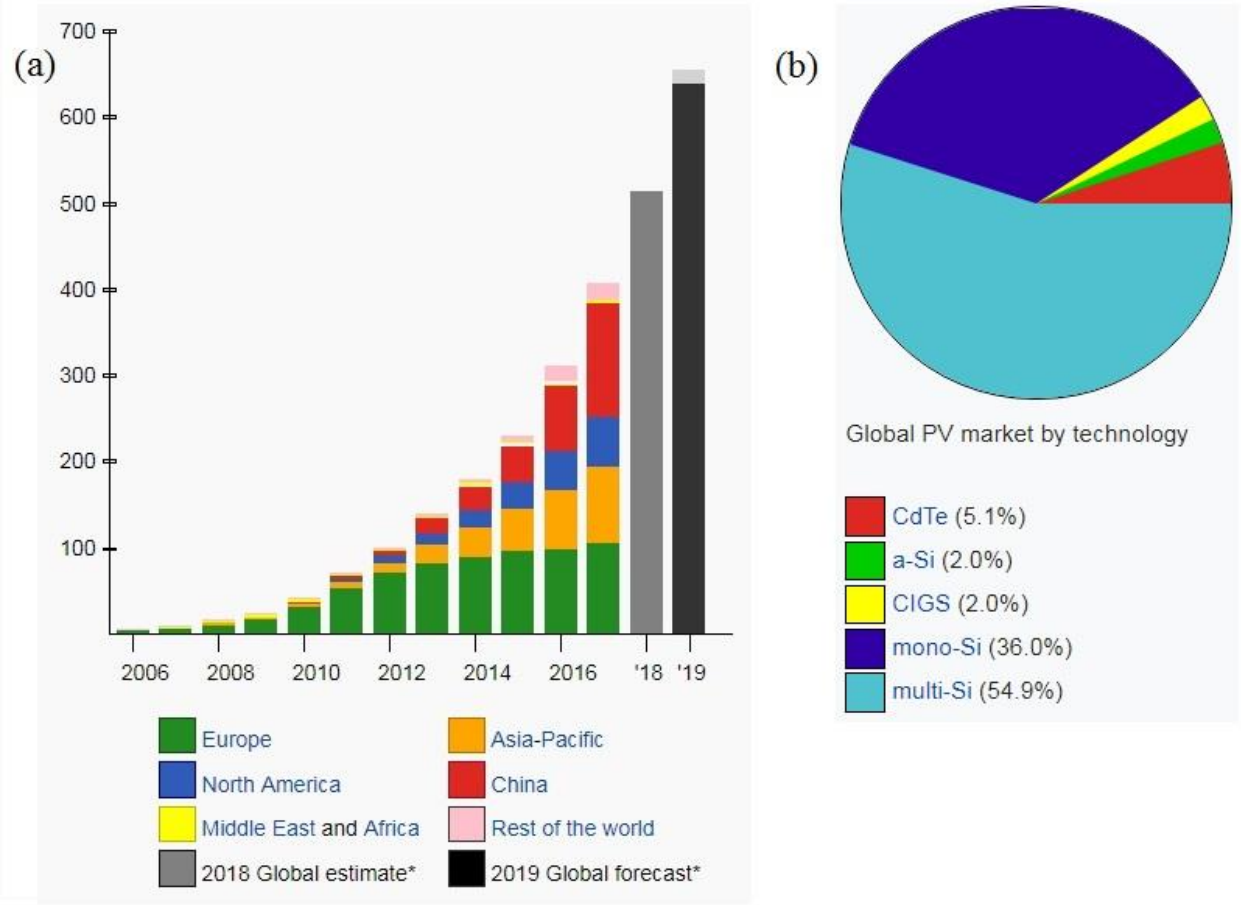

Fig 1.2: (a) Global cumulative PV capacity (b) C-Si share in the PV market[5]

A typical crystalline silicon solar cell is in fact a PN junction diode as shown in Fig. 1.3. When this diode is exposed to light, if the light photons have enough energy, Electron-Hole (EH) pairs can get generated and collected by the front and back contacts creating a current and voltage across an external load.

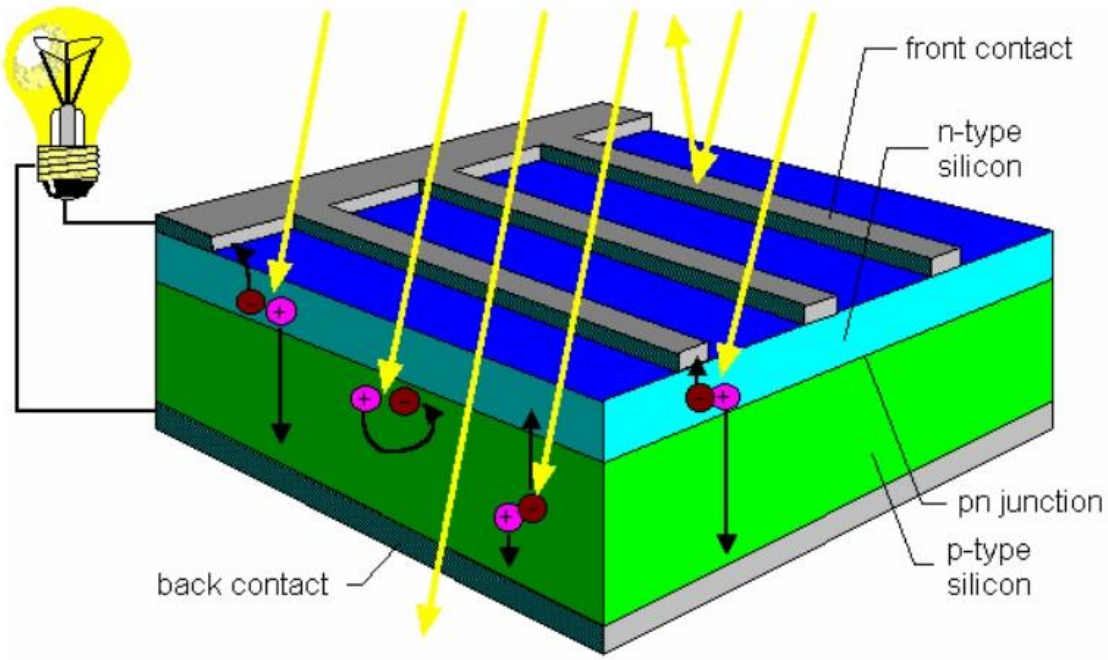

Fig 1.3: A typical c-Si solar cell[6]

Depending on how a solar cell is exposed to light and the way EH pairs are generated and collected, different configurations of crystalline Si solar cells could be defined such as monofacial solar cells with front surface metal contact which is shown above, bifacial solar cells as well as back contact solar cells, etc.,. Despite all the differences in the c-Si solar cell technologies, front and/or back contact deposition for the EH collection is a vital step which is mainly conducted by screen printing technology. As front and back contacts play a very important role in collecting the carriers and transferring the current, their influence in the efficiency and cost of the crystalline Si solar cells is highly important. Since developing a highly conductive material to be used as front or back contact is one of the main objects of this research, the available conventional conductive pastes are going to briefly reviewed in the next session.

1.2 Conventional Conductive Pastes

Aluminum or silver based pastes are usually considered for printing metal contacts in crystalline Si solar cells. As aluminum is normally alloyed with silicon at temperatures above 557°C (eutectic temperature), the surrounding silicon would be doped p-typed. Therefore, Al is usually used to form back surface field (BSF) as well as the rear contact [7]. On the other hand, Silver paste is

normally being used to form front contacts which typically contain following ingredients: ~80 wt% silver powder or flake, ~5 wt% Glass frit, ~5 wt% binder material, ~10 wt% vehicle material (a mixture of butyl carbitol acetate, terpinol, ethyl cellulose, butyl cellusolve) [8].

Silver and Al form electrodes at the surface of the solar cell and provide conducting pathways for transferring electrons. The conductivity mechanisms of the conductive paste are going to be reviewed in detail in the next chapter but in summary, aluminum alloy and silver particles formed at the interface during the firing step play the main role in the current transfer.

Decreasing the yield losses of commercial solar cells has been a major topic of interest for many research studies as different processing parameters, contact resistivity, metallic grids design optimization as well as emitter properties are extensively explored [9][10] . As mentioned, screen printing metallization is the most widely-used technique to form metallic contacts in commercial silicon solar cells. Among various process parameters in screen printing technology, firing step is considered to be a major yield-limiting and cost-determining stage as a high amount of thermal budget is consumed during high temperature sintering process. The bowing phenomenon caused by high temperature firing process is also considered one of the most important problems affecting the yield performance of the current solar industry.

Another important concern in conventional metallic pastes used in screen printing technique is the presence of lead which is not an environmentally friendly material. By increasing the environmental awareness, the universal attention on the toxicity of lead has increased and overall adverse effects of lead containing materials are being precisely monitored. Even small quantities of lead can affect the functionality of brain, kidneys and liver as well as nervous system when ingested. As a result, eliminating or minimizing the use of lead in electronic industry is rapidly growing. Therefore, developing a lead free alternative for currently available metallic pastes and conventional Sn/Pb solders has drawn attention in recent years.

Lead free metallic pastes containing metal oxides are the primary alternative for screen printing metallization but another interesting alternative would be electrically conductive adhesives (ECA) which have been of particular interest in electronic packaging applications since 1956 [11]. However, their possibility to replace conventional metallic pastes in screen printing technology has never been studied before and is going to be systematically investigated in this research. In addition to be environmentally friendly, ECAs provide low processing temperature comparing to the firing profile of conventional metal pastes which results in lower amount of deflection and bending

during the firing/curing and would enable PV technologies to use thinner substrates. Electrically conductive adhesives (ECAs) and their electronic properties are going to be thoroughly reviewed in chapter two.

1.3 Motivations for This Research

1.3.1 Developing a novel highly conductive nanocomposite

As reviewed above, electrically conductive adhesives (ECA) has been of particular interest in electronic packaging for a while but, their possibility to replace conventional metallic pastes in screen printing technology has never been studied before and is going to be thoroughly investigated in this research. In addition to being environmentally friendly, ECAs provide low processing temperature compared to the firing profile of conventional metal pastes. During high temperature firing in industrial silicon solar cells, residual stress will be produced in the cells which result in bending (deflection) of the substrate. This phenomenon is considered as a serious problem for assembly process and reliability of the fabricated modules especially in ultra-thin solar cells which normally cannot tolerate high stress levels and might cause failure. Therefore, Low temperature firing of ECAs could be very beneficial for developing ultra-thin solar cells to lower cost and increase yield performances.

Along with all the advantages of ECAs, they suffer from low conductivity comparing to other conventional metallic pastes/inks. Several methods have been proposed and studied in recent years to improve conductivity of ECAs; one latest way is using nanoparticles or nanowires in the polymeric matrix. Nano-sized materials could be included solely or with another micro-sized conductive particle to establish a more conductive network.

In this research, several approaches are taken to develop a highly conductive epoxy based nanocomposite using different nano-sized particles. The synthesizing recipe and curing profile of the nanocomposites are optimized to give the highest conductivity without degrading the mechanical properties of the material.

1.3.2 Residual stress analysis of the newly developed conductive nanocomposite

As mentioned above, high temperature firing in industrial silicon solar cells would produce residual stress in the cells which result in bending (deflection) of the substrate. Cell deflection is considered

as a serious problem for assembly process and reliability of the fabricated modules especially in ultra-thin solar cells which normally cannot tolerate high stress levels and might cause failure. Therefore, Low temperature firing of ECAs could be very beneficial for developing ultra-thin solar cells to lower cost and increase efficiency performances.

In this work, several developed highly conductive nanocomposites as well as a conventional silver pastes are screen printed, cured/fired and the amount of deflection as well as induced residual stress in the cured printed wafers are measured and compared to each other.

1.3.3 Device Fabrication using the newly conductive nanocomposite

The new developed conductive nanocomposite is intended to become an alternative material in many applications such as Printed circuit boards (PCBs), TFT electrodes and bus-bars in flat panel display backplanes, EMI Shielding in plasma display, LCD, RFID tags, electroluminescent lighting as well as touch screens. However, in this research the developed conductive nanocomposite is used in solar cell fabrication which has never been considered as an application for these materials. Increased probability of failures in ultra-thin solar cells due to residual stresses induced during firing stage has been major obstacles in their industrial production. However, substituting the back contacts by the developed conductive composite which has a very low firing/curing temperature will reduce the induced residual stress. Thus, ultra-thin substrates could be used in the new advanced solar cell designs.

In this research, solar cells are fabricated from scratch and evaporated Aluminum as well as the developed conductive nanocomposite are used as the back contact. Different electrical and optical properties of fabricated solar cells are characterized in CAPDS lab and cell performances are compared to each other.

1.4 Objectives of this PhD research

- Developing an environmentally friendly conductive alternative material for printed electronic applications
- Introducing a low processing temperature solution for screen printed metallization in PV technology to increase the yield performance values
- Establishing a process for screen printed structures to develop deflection measurements and residual stress analysis

- Introducing an effective work function definition for multiphase conductive nanocomposites
- Establishing a new method for measuring the effective work function of nanocomposites being used as an electrode in electronic devices
- Fabricating screen printed solar cells utilizing low temperature processes nanocomposites as the rear contact

1.5 Organizations of This Thesis

Chapter one:

A brief summary of different types of PV technologies is introduced in this chapter and crystalline silicon solar cells are reviewed in more detail. As the structure of a typical crystalline solar cell was reviewed, the importance of front and back contact in the performance of a cell is discussed. Then, the main conventional conductive materials being used as the front and back contacts are thoroughly reviewed. In the next session, the main motivations for this PhD research are categorized and explained and at the end, the principal objectives of this work are listed.

Chapter Two:

This chapter summarizes the main principles and methodologies of the conventional screen printing process. Fabrication sequences of the most conventional screen printed solar cells are explained briefly. Contact formation during firing step of screen printing is reviewed and contact microstructure and current transport mechanisms are investigated in detail. The bowing phenomenon in the deflected solar cells caused during firing the front and back contact is discussed and compared. Then the main conventional metallic pastes are introduced and compared with each other. The main ingredients of the metallic pastes and their roles in the paste are also mentioned in this chapter. Electrically conductive adhesives (ECAs) are introduced and suggested as an alternative for conventional metal pastes in screen printed solar cells. Chemical ingredients of ECAs as well as their different types are reviewed and compared to conventional metallic pastes. Two main conduction mechanisms in ECAs, percolation theory and tunneling effect, are explained theoretically and analytically. Furthermore, different pathways to improve electrical properties of

ECA are summarized. Effect of silver nanoparticles, nanowire and graphitic nanofillers in the ECA is reviewed and compared to each other briefly.

Chapter Three:

Development of Screen Printing Process and all the equipment required in this regard such as screen printing machine, screen specific properties, Drying oven and IR belt furnace are briefly explained in this chapter. The curing profile of the belt furnace is measured and plotted. Two different screen patterns considered for the front and back sides of the wafers are also illustrated. A conventional silver paste was screen printed, dried, fired and thoroughly characterized using scanning electron microscopy.

Chapter Four:

In this chapter, a primary simulation study was conducted to compare the amount of bending (deflection) in solar cells with metallic and ECA back contacts. Simulation results showed a significant decrease in the amount of bowing after replacing the metallic paste with ECA. Preparation procedure of two different conductive nanocomposite using silver nanowires is described in this chapter. The developed nanocomposite containing silver nanowires are printed on the silicon wafers and electrically and microscopically characterized. Electrical behaviour of the conductive nanocomposites is investigated using Dark IV and compared to each other. The nanocomposite with 0.1 wt% cured for 10 min gives the largest conductivity. Microstructure of the printed nanocomposite is characterized using Scanning Electron Microscopy. Due to low amount and small size of silver nanowires, their role in physical connecting of silver flakes is negligible. Therefore, the conductivity improvement after adding the silver nanowires is considered to be from tunneling effect mechanism. A through residual stress analysis was performed on the ECA, metallic pastes and the developed nanocomposite printed substrates and their amount of induced deflection was compared to each other. Results showed that nanocomposite printed wafers bend much less than metallic printed ones. Also, it was shown that adding silver nanowires improves the conductivity of the nanocomposite for around 70% which makes this nanocomposite a very good alternative for printed electronics applications. However, more conductivity improvement is required to compete with conventional conductive materials in PV technology.

Chapter Five:

In this chapter, a highly conductive nanocomposite was developed using graphene nanopowders as the second filler. Due to the large volume fraction of the graphene nanopowders and to achieve the best filler dispersion, the mixing procedure was optimized. Also, Graphene'shigh volume fraction would affect the polymer chains and post-printing curing reactions and therefore, the curing kinetics of the synthesized nanocomposite was studied using isothermal and dynamic Differential Scanning Calorimetry (DSC).A high degree of curing was obtained when samples are sintered at 150°C for 10 min.Thermogravimetric Analysis (TGA) was also used to study the thermal stability of the nanocomposite and results showed that the temperatures for onset of decomposition in graphene decorated nanocomposites are higher than their corresponding T_g showing their excellent thermal resistance. Compared to the printed ECA and nanocomposites with silver nanowires, the graphene decorated nanocomposites resulted in the highest boost in conductivity, over 2 orders of magnitude of ECA, bringing it comparable to metal pastes.A through residual stress analysis was performed on the developed graphene decorated nanocomposite printed substrates and the amount of induced deflection was compared to results from chapter 4. Considering the aspects of low curing temperature, good thermal resistance, high conductivity, and low residual stress, graphene decorated nanocomposite could be a promising alternative in screen printing metallization of thin substrates such as photovoltaics.

Chapter 6:

In this chapter, the electrical behavior of the developed graphene decorated nanocomposite with potential applications as electrodes in electronic devices is studied by measuring the work function of the nanocomposite. Since work function is inherently defined to be a property of a single material, in the case of nanocomposites where multiple materials are presented at the interface, inevitably, an Effective Work Function (EWF) definition was introduced. Three methods were utilized to measure the effective work function of the nanocomposite: IV method, UPS and TLM. IV method, which is based on the theoretical studies on tunneling phenomenon and the potential barrier height measurement analysis on MOS devices, was illustrated and used for the first time to measure the work function of a nanocomposite. The results were verified using two other techniques: UPS spectroscopy and TLM. The results from all measurements are in reasonable

agreement however a small difference between the UPS technique and the other two exists. The difference is attributed to the heterogeneous nature of the nanocomposite and the difference in the sensitivity of each measurement method to the surface structure. These observations indicate that a possibly device-dependent effective value for the work function is worthy to be expected.

Chapter Seven:

In this chapter, two Solar cells with different back contacts (Ref-Cell and NCOMP-GN-Cell) are fabricated using 4 inch wafers. All the fabrication processes are explained in detail and they were kept same and consistent except for the back contact material and deposition technique. Evaporated Al was used as the back contact for Ref-Cell while a newly developed graphene decorated nanocomposite (NCOMP-1wt%GN) was used as the back contact for NCOMP-GN-Cell. Cells were completely characterized using different techniques such as UV-VIS spectroscopy, Dark and Illuminated IV measurements systems as well as Internal and external Quantum Efficiency machine. Quantum efficiency results from NCOMP-GN-Cell were in an excellent agreement with the Ref-Cell while both cells showed slightly large ideality factors and low Fill Factors (FF). The large ideality factors and low Fill Factors (FF) are mainly related to the quality of the starting wafers specially their low carrier life time as well as front contact designs and process limitations. In general, the obtained performance results for both cells were very close to each other and both devices showed almost equal efficiencies which is a very satisfactory achievement for a standard technology baseline development.

Chapter Eight:

This chapter is the last chapter summarizing all the conclusions obtained in this PhD report. Some more reliability experiments and applications are suggested to be studied as the future work.

Chapter 2

Literature Review

2.1 Screen Printing Technology

Screen printing is originated from China similar to many other inventions and the first prints are reported to be from almost two thousand years ago. Then in 1850, the first modern form of the process was used in textile printing industry in both England and France. The first rubber bladed squeegee was designed and used by Albert Kosloff in 1920 but the major breakthrough occurred in the early 1940's by developing the first photographic stencil [14]. Screen printing has also been used in the electronic industry for more than 40 years to apply dielectrics as well as thick film conductors on different substrates to fabricate circuits [15]. The next session summarizes the main principles of the conventional screen printing process.

2.1.1 Screen Printing Principles and Methodology

The essential items required for making a screen print are as follow:

- Screen including a frame with a mesh containing a required design stretched upon it
- Squeegee fitted in to a holder
- Ink or paste

In this technique, a thick film of paste is transported through an aperture in the screen. There is an impenetrable emulsion layer on the screen which is stretched across a steel or aluminum frame. Contact patterns are defined by determined openings in the emulsion layer. The screen could be made of stainless steel, Nylon or polyester. To make the openings in the emulsion layer, the emulsion layer which is covered by a positive photo mask and contains the required patterns is exposed to light which hardens the lit area. Then screen is washed to remove the emulsion from the shaded area and form the openings [16]. During the printing process, as squeegee moves across the screen, the mesh of the screen is brought to line contact with the substrate and ink/paste is

pushed into the open areas and the extra material is removed by the edge of the squeegee [10, 13]. The basic steps of screen printing process are depicted in Fig. 2.1.

Amount of screen tension (high tension is preferred to help the screen to peel off the printed patterns just after the squeegee blade), rheology of the printed paste and printing parameters such as squeegee durometer, print stroke speed, attack angle, squeegee pressure and snap-off distance are important factors affecting the print volume and quality of the printed lines [9,14-15]. Mesh count of the screen (threads/cm), diameter of the wires and emulsion thickness define the maximum wet thickness of the pastes as follow [13]:

$$t_W = t_m A_o + t_e \qquad eq.2.1$$

Where t_W is the maximum wet thickness, t_m is mesh thickness, A_o is the fractional open area and t_e is the emulsion build-up thickness as indicated in Fig. 2.2.

A_o is calculated as:

$$A_o = \frac{(meshopening)^2}{(meshopening + wirediameter)^2} \times 100 \qquad eq.2.2$$

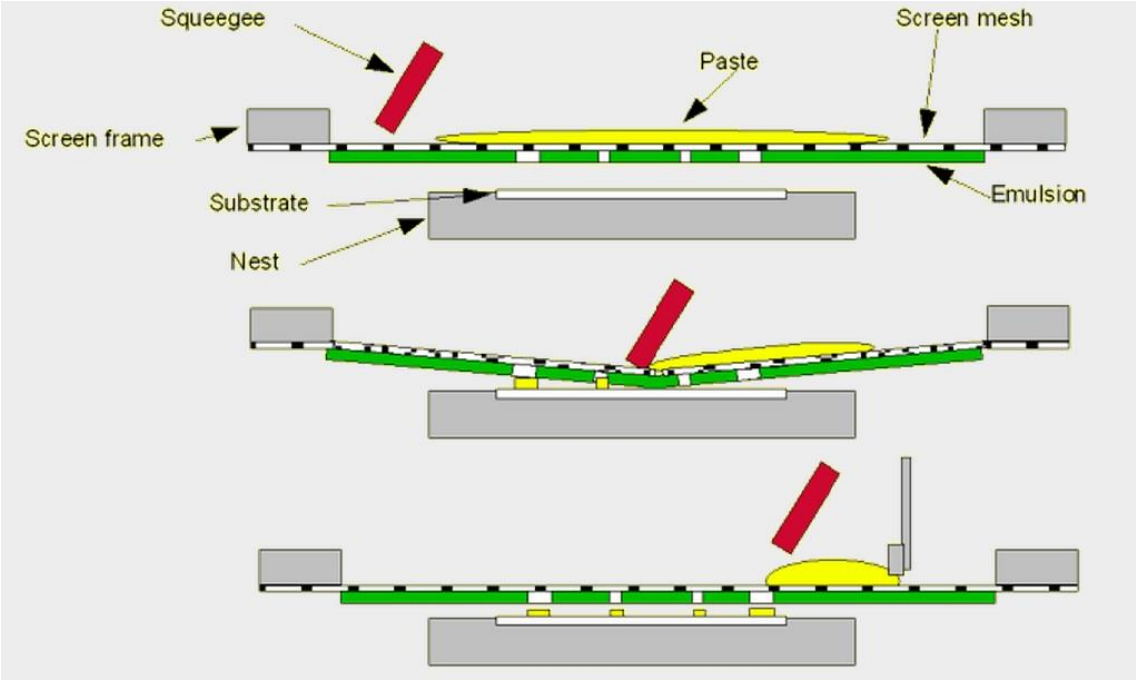

Fig 2.1: The screen printing methodology [14]

The greater fractional open area (A_o) of the mesh makes the passage of the paste easier through the screen. There are two useful rules to choose a proper mesh named as “rules of thumb”. According to the first rule, the minimum line width of the printed pattern would be three times the mesh thread diameter. Thus, Small thread diameter should be used to print narrow lines.

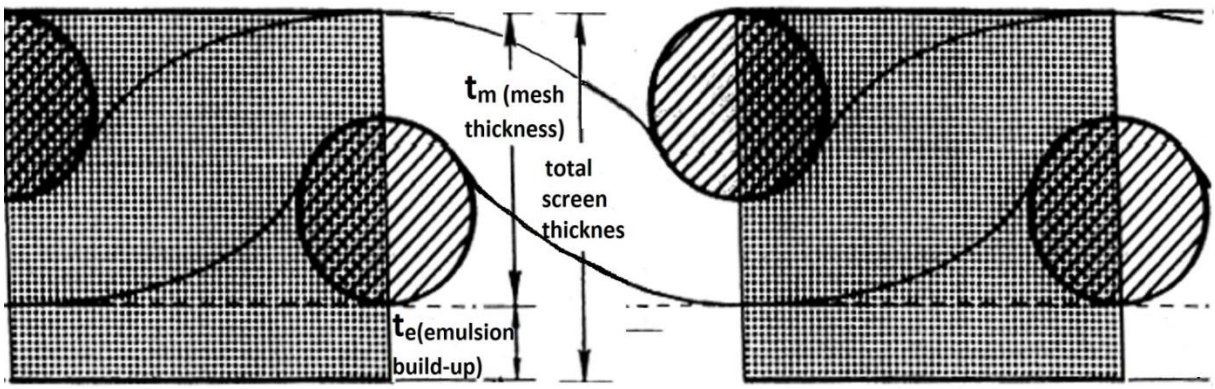

Fig 2.2: Cross section of screen mesh and emulsion layer [13]

The Second rule is that the mesh opening ought to be at least three times the size of the particles in the paste or ink [14].

Screen printing versatility in being able to print almost all materials has made this process very popular and attractive. Although many terms are considered to define the printing medium such as ink, paste, resist, die, conductive epoxy, adhesive, ceramic enamel or rubber latex, most of mediums could be defined as two general terms: ink which is used for materials with low viscosity and paste applied for more viscous mediums.

One of the most important features in electronic devices is the conductive structure forming by depositing metallic pastes that connects various components. Metallic contacts in commercial silicon solar cells is considered to be the most widely application of screen printing technique which is going to be covered thoroughly in the following session.

2.1.2 Screen Printing Application in Solar Cells

As mentioned above, screen printing metallization is the most widely used technique to form the metallic contacts in commercial silicon solar cells [16-17]. Photolithography (PL) and buried contact technology (BC) are also two other well established metallization techniques for solar cell

fabrication. Low metal contact resistance, very fine gridlines (around 8μm) and no shunting effect are major advantages of PL method leading to high energy conversion efficiency in cell performance [18-20]. However, patterning the photo resist mask and evaporating metals under vacuum in PL technique have made it a time consuming and expensive technology. Buried contact (BC) technology also enables the cells to have selective emitter or emitter region with lighter doping level among the grooves leading to lower surface recombination, good metal conductivity and low contact resistance [25]. Nevertheless, BC technique is also much more expensive than screen printing technology (screen printing module is almost $0.38/W cheaper than a BC module) [26]. Therefore, screen printing is still considered a more rapid and cost-effective process compared to PL and BC technologies. Producing less chemical waste and being practical and modular for actual industrial facilities are other major advantages of screen printed technologies [27]. Fabrication sequence of the most conventional screen printed solar cells is shown in Fig. 2.3. Each sequence is briefly explained in the following sessions.

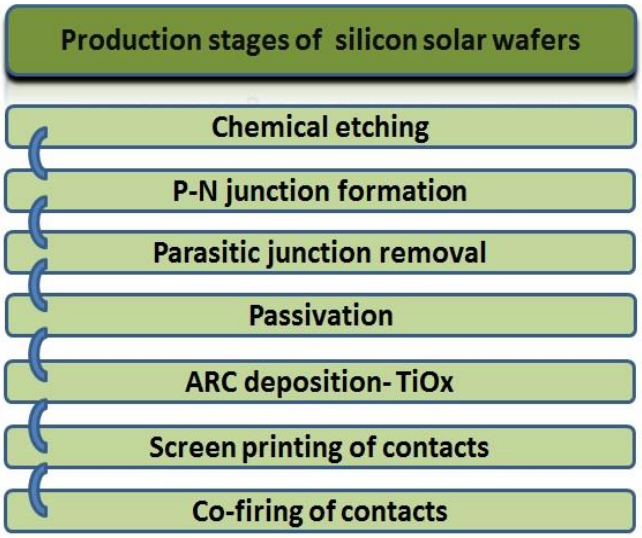

Fig 2.3: Production stages of the conventional solar cells

2.1.2.1 Chemical etching

The main purpose of the chemical treatment is eliminating the saw damage and removing contamination as well as native oxides from wafers. Several etching methods have been reported so far [13-14]; however, a typical example of chemical procedure applied before the donor doping

process would be RCA 1 and 2 to remove organic and metallic contaminations followed by 2% HF dip to remove the native oxide.

2.1.2.2 P-N junction formation

Developing the emitter is considered to be one of the most important steps in solar cell fabrication process which is obtained by simple diffusion process. High concentration of dopants near to screen printed contacts reduces the contact resistance; however, it forms a dead layer reducing the blue response of the cell [28]. The cell blue response would be improved though by forming shallower emitters in newer cell designs.

2.1.2.3 Surface Texturing

Surface texturing is performed by etching pyramids with a chemical solution at the surface of wafers to reduce light reflection. Several other methods of texturing are developed such as mechanical texturing with laser or cutting tool [29], isotopic chemical etching based on the defects [30], isotropic chemical etching combined by photolithographic mask [31] as well as plasma etching [32].

2.1.2.4 Passivation and ARC

Surface passivation of the solar cells reduces surface recombination and increases carrier lifetime and significantly improves the efficiency of solar cells. Passivizing the surface of Si- SiO_2 in solar cells could be performed by growing thermal oxide films at high temperatures or depositing silicon nitride at low temperatures [33]. Thermal oxidation has several advantages such as developing an oxide layer with excellent resistivity to most common impurities (B, As, p, Sb), high electrical resistivity as well as stable and reproducible surface passivation quality. However, in spite of its advantages, carrier life time would be degraded by high processing temperature in this method [34]. Investigations has revealed that deposition of SiN layer through plasma enhanced chemical vapour deposition (PECVD) which requires lower processing temperature could form a better passivation layer in solar cells [35]. Low temperature deposition, higher passivation quality and adjustable refractive index have made silicon nitride layer a proper choice for more applications in solar cell processing as ARC or passivation layer for front and rear side [30, 32].

To reduce light reflection, antireflection coatings (ARC) are deposited on the surface of solar cells (especially for multi-crystalline materials which are difficult to be textured). Titanium dioxide (TiO2) and silicon nitride (SiN) are two common antireflection coatings using in industrial solar cells[33]. Coatings are mainly deposited by simple techniques such as spraying or chemical vapor deposition [33].

After surface passivation and applying the antireflection layer, cells are stacked one on top of the other for edge isolation to remove the junction at the edge. This process is performed by various techniques like plasma etching, laser cutting or covering the edges to prevent diffusion of dopants at the border in the first place [28]. Next step would be depositing the front and back contacts which is reviewed in more detail in the next session.

2.1.3 Metallization in Silicon Solar Cells

Process of metallization has three steps:

- Paste deposition
- Drying
- Firing

The main stages in paste deposition are same as basic steps of screen printing process explained in session 2.1.1. Another configuration of the process is shown in Fig. 2.4.

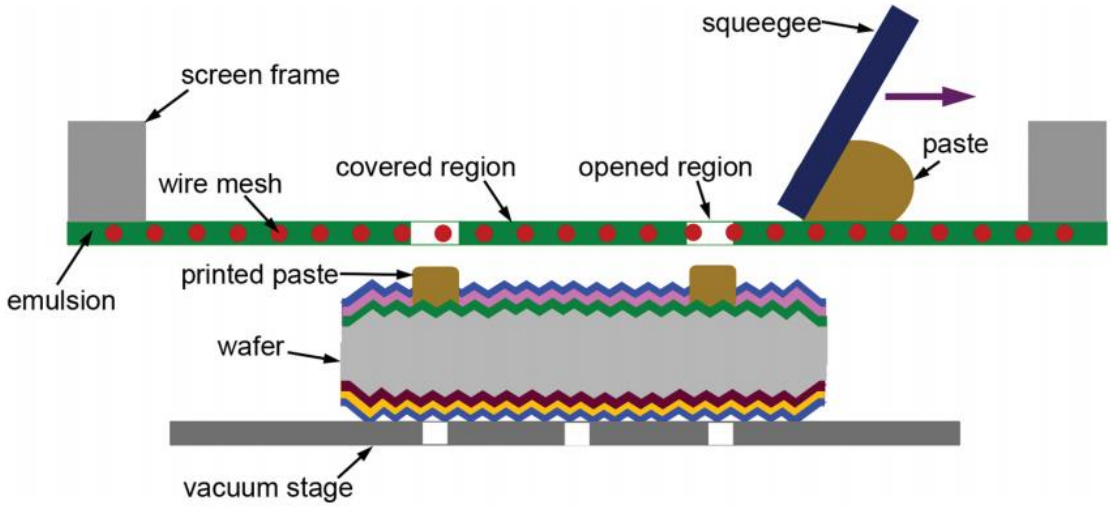

Fig 2.4: The screen printing methodology [37]

2.1.3.1 Drying

Drying is basically conducted at temperatures less than 200°C to evaporate some of solvents and remove the air bubbles from the paste. Solvents that have failed to be burnt off even in firing step could initiate cracking in the contacts while air bubbles trapped in the paste decrease the conductivity of the electrodes [38].

2.1.3.2 Firing

Firing is a particular thermal processing in which contacts are formed in a short time at around 800°C. Conveyor belt furnaces (infrared furnaces) with a typical firing profile depicted in Fig. 2.5 are normally used for this sintering process. As shown in Fig. 2.5, solvents and organic ingredients of the paste are burnt off at temperatures below 600°C and only metal and glass components are remained. Main part of firing and contact formation involving glass softening and metal sintering happens between 600°C and 800°C which is much below the eutectic temperature of Ag-Si (835°C) and silver melting point (961.9°C) [35-36]. It should be noted that a slightly lower firing temperature could cause a significant increase in series resistance of the cell while a slightly higher temperature decreases the lifetime of the minority carriers and degrades the output current [41]. The mechanisms of contact formation are fully explained in the following session.

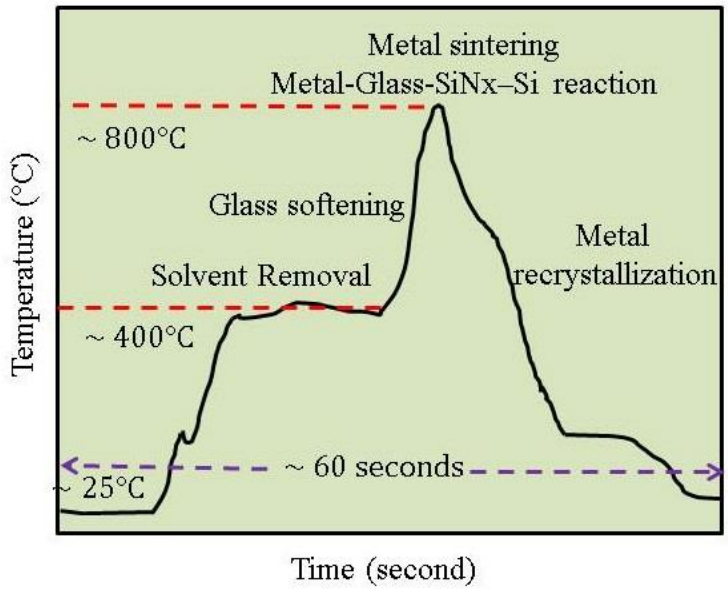

Fig 2.5: Firing profile of a commercial silicon solar cell

2.1.4 Screen Printing Yield Loss in PV devices

As it was mentioned in the previous chapter, reducing the cost and decreasing the yield losses has been in main concern in PV industry. Module manufacturing cost takes around 80% of the total price while silicon raw material occupies almost 55% of the PV module price and considering that crystalline silicon solar cells dominate the photovoltaic power generation, decreasing the raw material usage plays a vital role to reduce the PV production cost. Decreasing the thickness of the solar cell is considered to be the easiest way of reducing the silicon raw material usage; however, thinner crystalline solar cells usually lead to higher yield losses due to higher chances of breakage problems caused by bowing phenomenon [43].

Bowing is caused by the residual stress induced in the solar cell during the firing step. Residual stress is caused due to the difference between thermal expansion coefficients of front and backside electrodes and the c-Si wafer. The bowing phenomenon in a partially processed solar cell is shown in Fig. 2.6 [44].

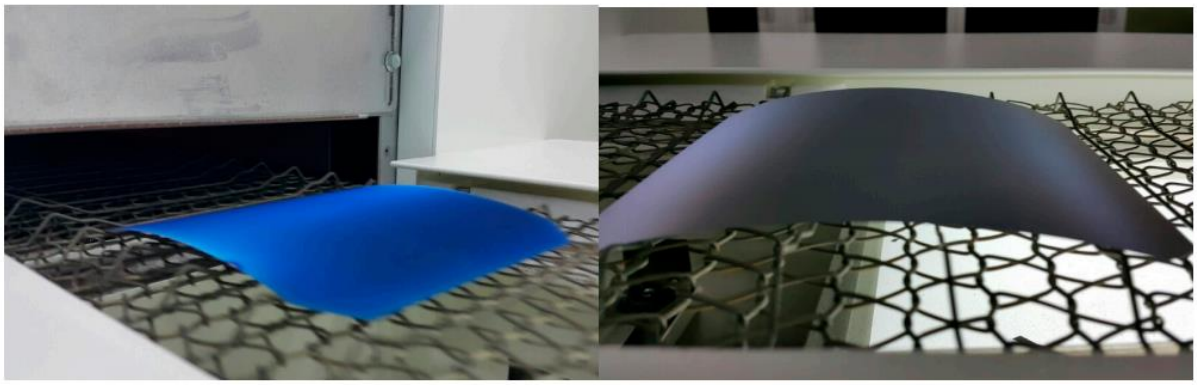

Fig 2.6: Bowing phenomenon in a partially processes solar cell[44]

Finite element simulation method (FEM) was used by researchers to help with understanding the problem of bowing [41-43]. Chen et al modeled a conventional Si solar cell with the geometry shown in Fig. 2.7 while the amount bowing was measured as maximum distance between the plane containing the bottom of the corner edges and the plane containing the top edge of the solar cell [45].

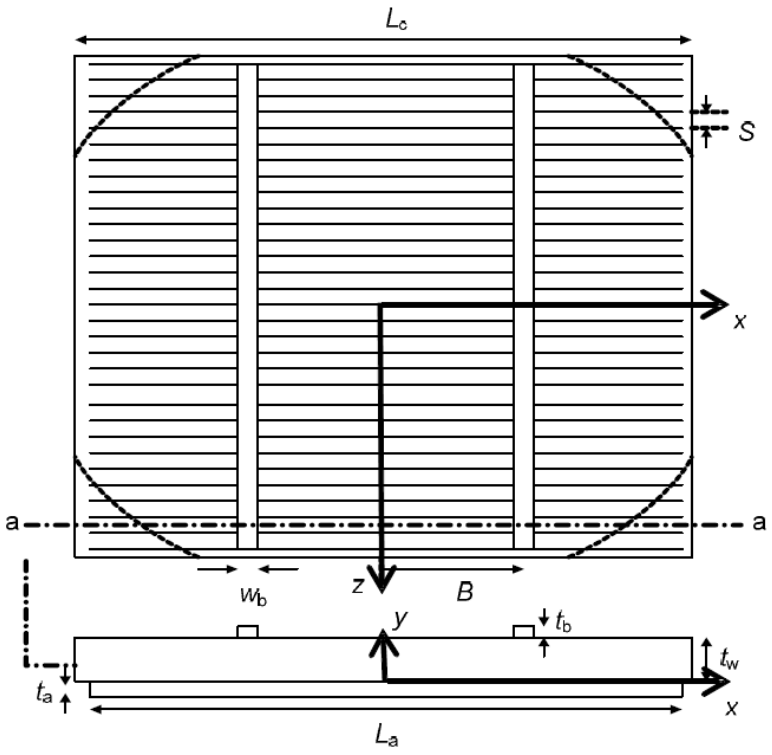

Wafer type	L_w	L_a	S	W_b	B
sc-Si wafer	125	122	2.1	2	29.5

Fig 2.7: Typical Model Geometry of a solar cell for FEM simulation of bowing[45]

As the simulation results show in Fig. 2.8, the deformed cell is very similar to the real bowed cell meaning that the cell is bent downward as the Al back contact is on the inner side. This shows that the AL inner contact is dominating the bowing phenomenon in the solar cell which is make sense due to its coverage area. JR Lim et al. [44] also compared the cell bowing in two cells: one with the front contact and one without it and as it is shown in Fig. 2.9, the contribution of the front contact in the total bowing amount is almost negligible compared to back contact induced. Controlling the Al-paste formulation, decreasing the thickness of the AL back contact as well cell heat treatments are suggested to be the ways to reduce the bowing which has reported to affect the cell performance and increasing the cost [44-46]. However, the other way to reduce the bowing is reducing the firing temperature for back contact firing by replacing Al with a low processing temperature conductive material which is going to be addressed in more details in this research.

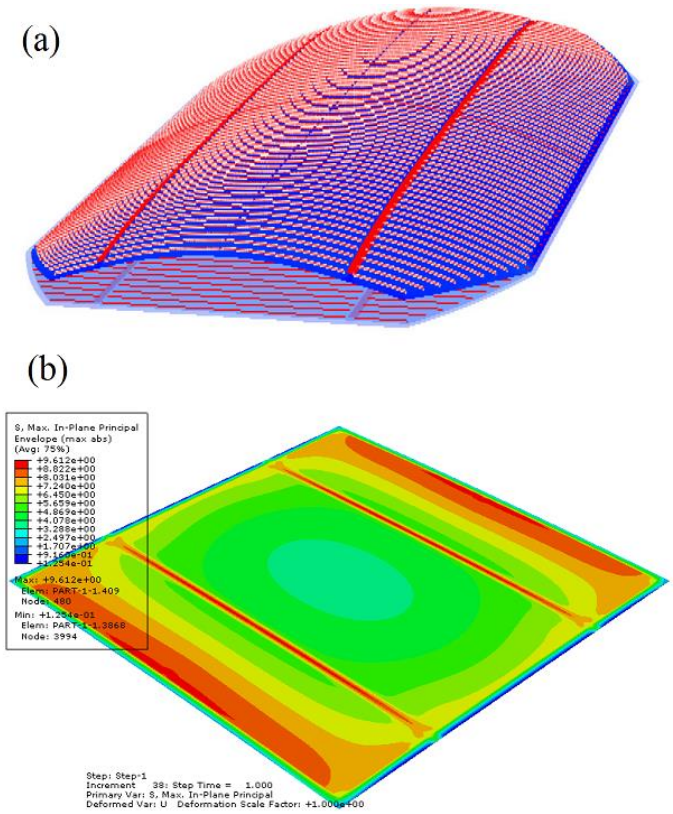

Fig 2.8: FEM simulation results of (a) cell bowing (b) stress distribution induced by firing process [45]

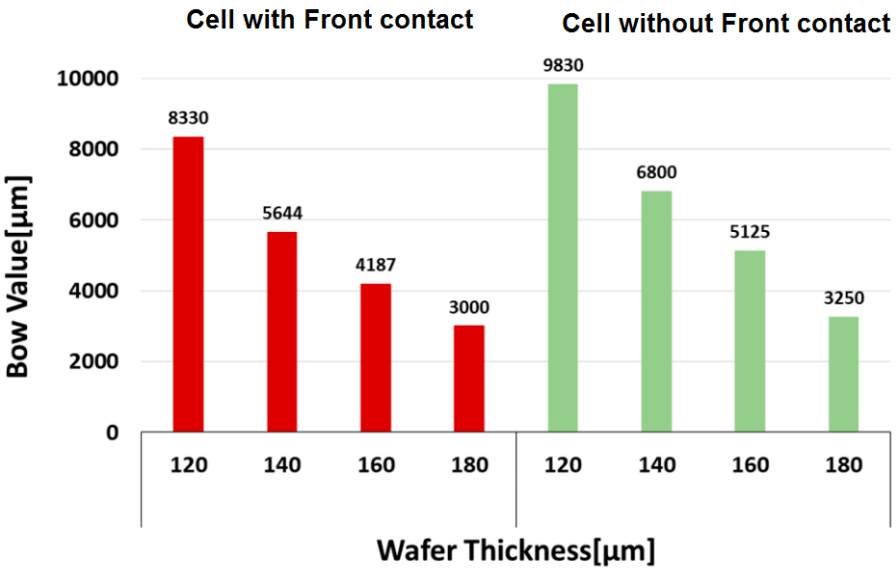

Fig 2.9: Front and back contact contribution in bowing phenomenon [44]

2.1.5 Contact Microstructure

Contact formation and current transport mechanism in screen printed contacts is not fully clear and a few mechanisms are proposed in this regard. All the proposed mechanisms agree on one important fact that glass frit plays a critical role during contact formation. The first theory was suggested by Cheek et al [52] proposing that the firing process was liquid phase sintering while Ballief et al [53] suggested that silicon and silver would be dissolved in the glass frit during firing and recrystallization of silicon occurs during cooling and then silver nucleate and grow on silicon. It was further suggested that only silver particles are dissolved in glass frit and would be recrystallized subsequently upon cooling [50, 51]. Then, Schubert et al [56] suggested that PbO in glass frit react with Si and would be reduced to Pb which makes an alloy with Ag. The <100> silicon planes are dissolved by the generated alloy and Ag crystallized on the <111> planes of the dissolved silicon surface [56]. Interface microstructure of optimally fired screen printed contacts is thoroughly studied by Lin et al (Fig. 2.10) [36, 53]. As it is shown in Fig. 2.10(a)-(c), three different microstructures could be found in the optimally-fired contacts: (a) Ag/thin glass layer/Si (b) Ag/thick glass layer/Si (c) Ag/glass layer/ARC/Si. Ag/thin glass layer/Si microstructure is suggested to be the main path for current conduction while in the case of having large glass frit clusters or big voids at the interface plane, a thicker glass layer could be formed (Fig. 2.10(b)). Also, at some part of the interface, residual antireflection coating could be remained between the glassy phase and Si (Fig. 2.10(c)). This residual ARC layer reduces the surface recombination; however, Ag embryos can't form because ARC inhibits Ag diffusion toward Si substrate. The amount of residual ARC layer is higher in under-fired samples compared to optimally-fired ones [36, 53].

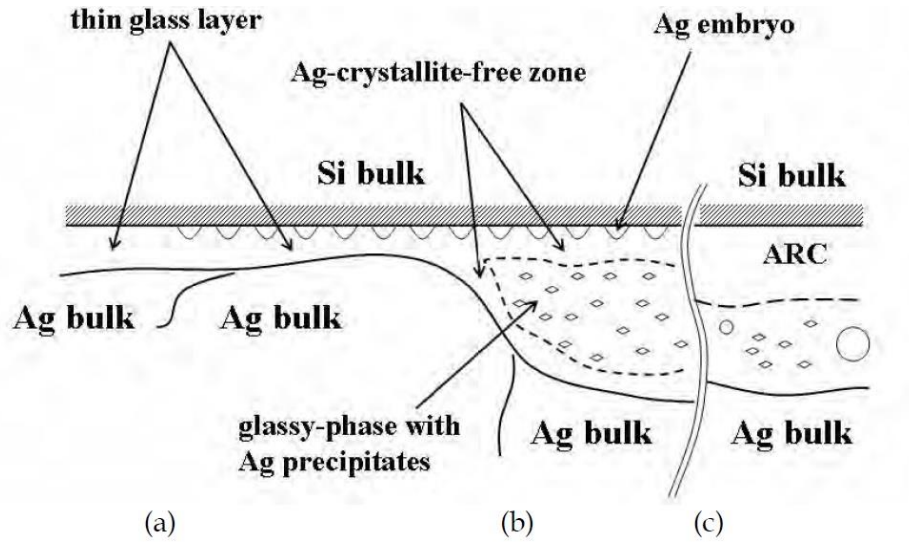

Fig 2.10: Three important interface microstructure (a) Ag/thin glass layer/Si (b) Ag/thick glass layer/Si (c) Ag/glass layer/ARC/ Si [40]

2.1.6 Current Transport Mechanism

Current could be transported from silver precipitates and silver bulk by three possible mechanisms [36, 50, 53]:

1. Direct connection between Ag precipitates and silver bulk
2. Tunneling through thin glass layer from Ag embryo serving as current pickup points to silver bulk (Fig. 2.11(a)).

Ag embryos which play an important role in transporting current at the interface originate from the silver dissolved in the glass phase during firing and are in direct with silicon bulk. Developing high densities of Ag embryos and keeping the glass layer as thin as possible improves the conductivity of electrical contact in this mechanism [40].

3. Current transport through thick glass layer via multi step tunneling between Ag precipitates in the glass layer (Fig. 2.11(b))

In thick glass layers, Ag precipitates form saturated glassy layer during firing and act as charge storage centers. Charge could be transported between these precipitates by quantum-mechanical tunneling of electrons. In addition, the dissolved silver in the glassy phase acts as trap point and increases the charge transportation rate [57]. The breakdown voltage is less at the interface of Ag precipitate/glass layer due to small radius of curvature at the interface[58]. The curved interface

effect as well as proper conductivity of Ag-supersaturated glassy phase provides charge transport through the thick glass layer by multistep tunneling and thermally excited electrons jumping from one precipitate to the other [57].

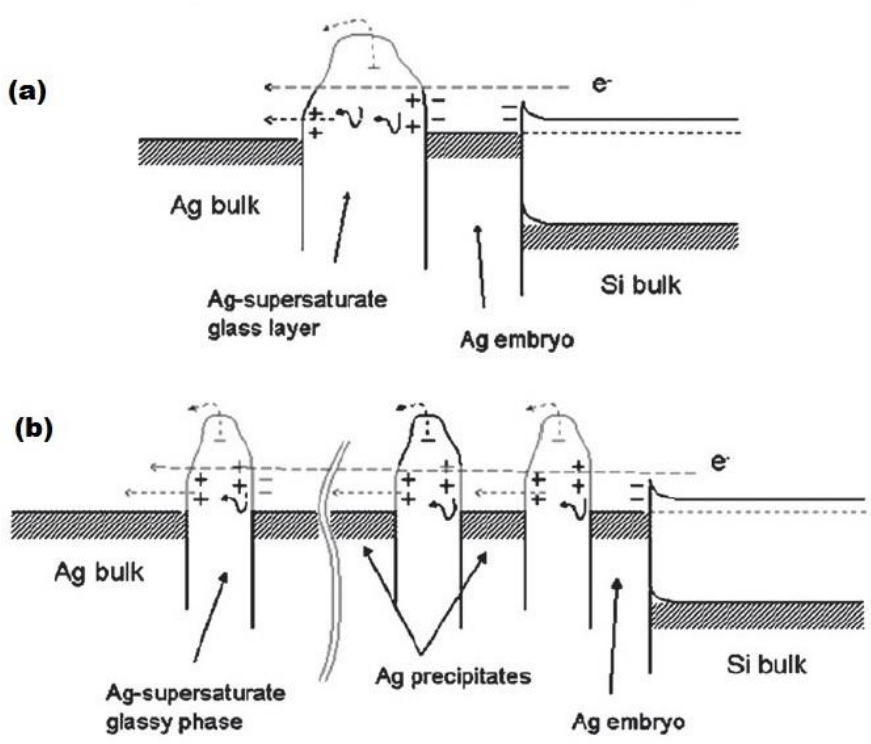

Fig 2.11: Possible current transport mechanism in (a) Ag/thin glass layer/Si (b) Ag/thick glass layer/Si[57]

As mentioned above, current cannot transport in those parts of the interface containing Ag/glass layer/ARC/ Si layers as silver diffusion into Si is prohibited by residual ARC and Ag embryos wouldn't be able to nucleate.

2.1.7 Conventional Metallic Pastes

Aluminum or silver based pastes are usually considered for printing metal contacts. As aluminum is normally alloyed with silicon at temperatures above 557°C (eutectic temperature), the surrounding silicon would be doped p-typed. Therefore, Al is usually used to form back surface field (BSF) as well as rear contact in p-type cells or a rear emitter in n-type cells [7]. Silver paste is also used to form contacts in n-type doped surfaces like phosphorus doped silicon. A typical

silver paste contains following ingredients: ~80 wt% silver powder or flake, ~5 wt% Glass frit, ~5 wt% binder material, ~10 wt% vehicle.

Silver forms electrodes at the surface of the solar cell and provides conducting pathways for transferring electrons. Hilali et al. showed that electrical performance of the cell depends on the size of the silver particles[12]. Glass frits (metal oxides like PbO or ZnO [60]) are responsible for adhesion to the silicon substrate. Binder materials such as ethyl cellulose, polyvinyl alcohol (PVA) and methyl methacrylate improves the strength of the printed patterns before firing step. Vehicle materials containing organic solvents are used to carry the solid components of the metallic paste [13]. Both binder and vehicle which would be burnt off at temperatures less than 600 °C, control paste rheology.

Increasing the efficiency of solar cell has been a main topic of interest for a long time and different factors are considered in this regard such as: processing parameters, contact resistivity, metallic grids design optimization as well as emitter properties. Among processing parameters, firing step is considered to be a major efficiency limiting and cost determining stage as a high amount of thermal budget is consumed during high temperature sintering process [57-58]. One other important concern in conventional metallic pastes is the presence of lead in glass frit which is not an environmentally friendly material. Developing a lead free alternative for currently available metallic pastes and conventional Sn/Pb solders has drawn attention in recent years [59-60]. Lead free metallic pastes containing metal oxides are the first alternative for screen printing metallization [65] but another interesting alternative for metallic pastes would be electrically conductive adhesives (ECA) which has been topic of interest for electronic packaging applications since 1956 [66]; however, their possibility to replace conventional metallic pastes in screen printing technology has never been studied and is going to be investigated in this research work. Next session would give a brief summary about different properties electrically conductive adhesives (ECAs).

2.2 Electrically Conductive Adhesives (ECAs)

ECAs have been used for electronic packaging applications such as hybrid, die attach and display assembly [11] and as also mentioned above, they are an environment friendly solution for interconnections in electronic applications. In addition to be environmentally friendly, They provide low processing temperature comparing to the firing profile of conventional metal pastes

which is the most energy consuming step in screen printing methodology. The main parts of ECAs are an Organic/polymeric binder matrix and conductive metal fillers. ECAs are mainly divided into two different groups based on conduction direction: anisotropic conductive adhesives (ACAs) and isotropic conductive adhesives (ICAs). The electrical behaviour of ACAs and ICAs is deferent from each other based on percolation theory as depicted in Fig. 2.15 [15]. For ICAs, the volume fraction of fillers exceeds the percolation threshold (V_c) leading conductivity in all x, y and z directions while the conductivity of ACAs is provided only in one direction. Percolation threshold is typically in the order of 15-25% volume fraction [11, 60]. It should be noted that the resistivity shown in Fig. 2.12, is representing the bulk resistivity of the ECAs.

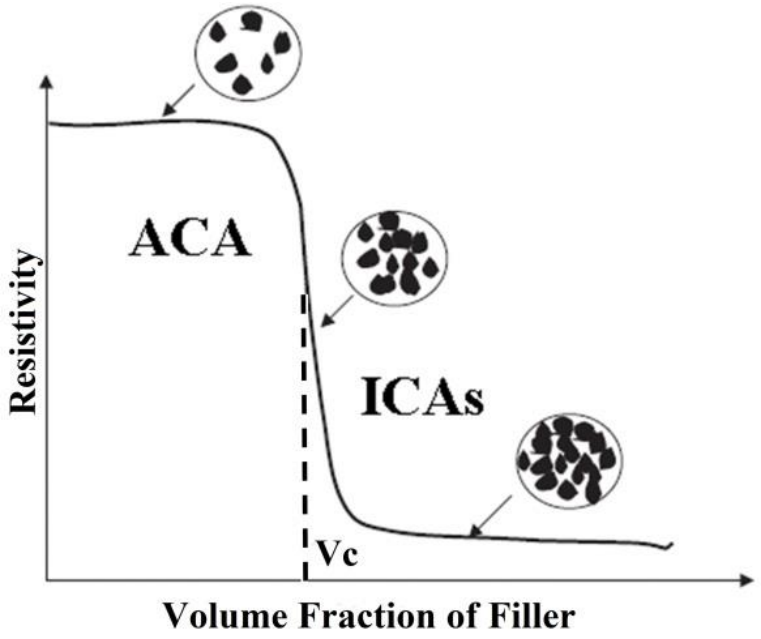

Fig 2.12: Typical percolation curve of conductive adhesives[15]

Higher resistivity of ACAs compared to ICAs, voids or open circuits resulting from the random distribution of conductive particles in ACAs as well as the necessity of applying heat and pressure simultaneously during hardening the matrix, has restricted application of ACAs in high-end electronic applications. Many studies are conducted on ECA development, discussing their benefits and drawbacks and investigating their main technological applications [11, 60, 64-65]. The most important advantages and disadvantages of ECAs over Conventional metallic pastes are shown in Table 2.1.

Table 2.1: Advantages and disadvantages of ICAs

Advantages	Disadvantages
Offering an environmental friendly alternative	Lower conductivity
Low processing temperature	Unstable contact resistance
Low thermo-mechanical fatigue	Poor impact performance
Can be used on a wide range of surfaces	
Can be utilized for finer pitch applications	
Shorter and quicker assembly time (fewer processing time)	
Low cost	

2.2.1 Composition of ECAs

ECAs are composed of an adhesive matrix (polymeric binder) which provides mechanical strength and conductive fillers used for charge transport. The main characteristics for an ideal polymeric matrix for ECAs are long shelf life, relatively high glass transition temperature (T_g) - conductive adhesives with low T_g lose electrical conductivity during aging- fast cure, low moisture absorbance, and good adhesion **[**69**]**. Thermoplastic resins like polyimide can be used for the ECA matrix However, despite their good reworkability, the adhesion of thermoplastic ECAs degrades at high temperature which makes this material not a good choice in many applications. Therefore, the most commercial ECAs are based on thermosetting resins like epoxy resin because of their superior mechanical and thermal properties as well as processability [67-68]. Regarding the conductive filler, silver (Ag), Gold (Au), Copper (Cu) and carbon are used in ECA formulations. However, Silver is the most common filler because of its high room temperature electrical and thermal conductivity as well as the unique characteristic of its conductive oxide (Ag_2O). The most popular morphology of conductive fillers is flake because of their higher aspect ratio, more contact spots and consequently more electrical paths in comparison to spherical particles. The filler size generally ranges from 1 to 20 μm [15].

2.2.2 Conduction mechanisms in ECAs

Although percolation theory predicts the conductivity of ECAs, this theory neglects the role of polymer matrix and type of the filler and is only based on the geometric characterization of the

filler. Thus, tunneling effect or field emission theory is developed to avoid these flaws and is defined as penetrating electrons from one filler in to the potential barrier and reaching to the next filler at some distance. According to this theory a conductive network is formed among the adhesive without filler particles contacting each other. Both percolation theory and tunneling effect mechanisms are depicted in Fig. 2.13 (a) and (b) schematically.

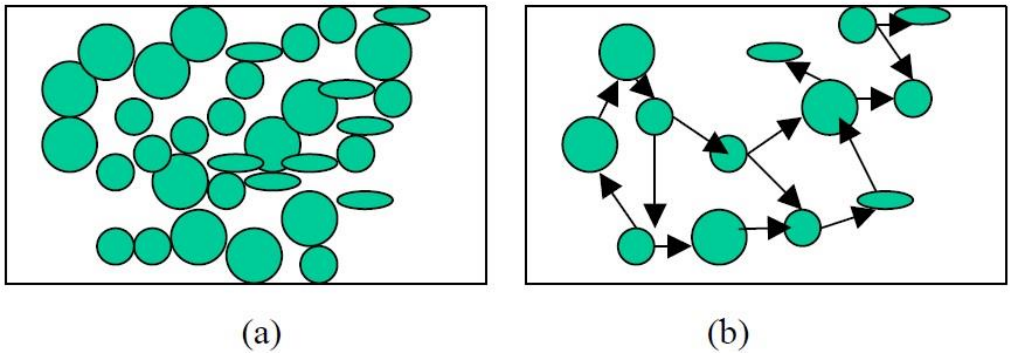

Fig 2.13: Conductivity mechanisms (a) percolation theory (b) Tunneling effect [72]

Bulk resistance of the ECAs decreases dramatically after the adhesive is cured [70-71]. It is not completely clear what happens during curing the ECAs but a few researches are conducted on investigating the conduction mechanism [72, 74]. Conductivity improvement during thermal cure is suggested to be the result of lubricant removal [75] as well as the compressive force induced by cure shrinkage [72, 74]. However, D. Lu et al. showed that resin cure shrinkage plays a more important role during conductivity establishment in a conductive adhesive [77].

The total resistance of particle-particle contacts in percolated linkages in conductive composites has two important contributions: constriction resistance and tunneling resistance. Constriction resistance (R_{cr}) is the consequence of the current flow being constricted through small conducting contact spots and can be calculated as:

$$R_{cr} = \rho_i / D \qquad eq. 2.3$$

Where ρ_i is the intrinsic filler resistivity and D is the diameter of the contact spot.

Moreover, when thickness of the thin film layer coated on the surfaces of the particles is in the order of 100Å or less, quantum mechanical tunneling with a lower resistivity occurs [72, 75]. In electrically conductive adhesives containing Ag filler, three different films could exist on the filler

surface: Tarnish films which are basically Ag_2O and Ag_2S, some organic material that has been applied as lubricant to help dispersion of flakes in the epoxy as well as a thin film of epoxy which could cover the silver flakes. Tunneling resistance depends on tunneling resistivity (ρ_t) and the area of the contact which is covered by the thin film (A_c) and can be derived as:

$$R_t = \rho_t / A_c \qquad eq.2.4$$

Thus, the total particle-particle resistance (R_c) is equal to:

$$R_c = \rho_i / D + \rho_t / A_c \qquad eq.2.5$$

During thermal curing, the resin shrinks and compresses the particles bringing them closer to each other and both, particle- particle contact area (A_c) and contact diameter (d) increases as well causing both R_{cr}, R_t and R_c to decrease (Fig. 2.14) [11, 75].

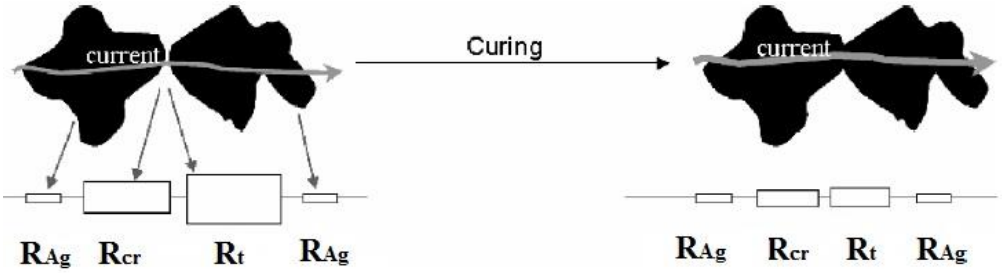

Fig 2.14: Particle-particle contact resistance in ICAs

There is also discontinuity of crystal lattice order in the contact spot which could reflect electrons and produce a resistance; however, such resistance is very similar to the resistance of the grain boundaries in the poly crystalline materials and could be neglected **[**79**]**.

As it is depicted in Fig. 2.15, the overall resistance (R_{total}) of ECAs will have three main parts: 1) resistance of particle-particle contacts (R_c) 2) bulk resistance of fillers (R_f) and 3) resistance between filler and substrate (R_s) [66, 77] :

$$R_{total} = R_c + R_f + R_s \qquad eq.2.6$$

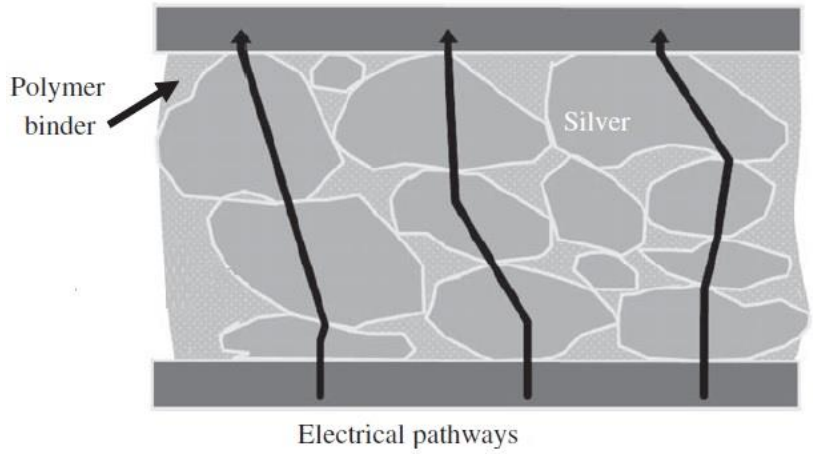

Fig 2.15: Electrical paths in ICAs[81]

2.2.3 Pathways to improve electrical and structural Properties

One way to improve the conductivity of ECAs is by removing the lubricant layer on the silver flakes which is an electrically insulating material. It is revealed that using lubricant removals like short-chain acids such as adipic acid, high boiling point ethers like diethylene glycol monobutyl ether or diethylene glycol monoethyl ether acetate could improve the conductivity of conductive adhesives [75].

The second way, as mentioned in the last part, would be increasing the curing shrinkage by adding a small amount of multifunctional epoxy resin to the formulation of the adhesive. The multifunctional resin increases cross linking density, shrinkage and therefore conductivity [82].

Although the silver oxide is a good conductive material compared to the other metal oxides, its conductivity is still inferior to metal itself. So, incorporation of reducing agents such as aldehydes is considered as the third approach to improve the conductivity of ICAs **[**83]. The oxidation reaction can be shown as:

$$R–CHO+Ag_2O \rightarrow R–COOH+2Ag$$

The other way is using nanoparticles or nanowires in the polymeric matrix. Nano-sized materials could be included solely or with another micro-sized conductive particle. ECAs with nanomaterial have been a point of interest for researchers and are briefly explained in the next session.

2.3 Nanoparticles and Nanowires in Polymer Media

As mentioned above, due to the special electrical mechanical, chemical, optical and magnetic properties of nanoparticles and nanowires, ECAs containing nanomaterial have been studied in the last few years to achieve finer pitch and high performance interconnection in advanced electrical packaging. Nanoconductive particles, nanowires, or graphitic nanofillers are considered in the developing nano conductive adhesives and will be reviewed in the following sessions.

2.3.1 ECAs with silver nano particles

Silver nanoparticles have been considered as an alternative for micro-sized silver flakes in ECAs in recent researches. The main advantage of using nano-sized particles or wires is that they would disperse in the areas where bigger fillers cannot scatter and contact each other and then a more conductive network would be developed via tunneling effect. Effect of substituting micro-sized silver particles by nano-sized filler in PVAc matrix either in part or as a whole is studied by Lee et al [84]. This work showed that adding silver nano particles would increase the resistivity of the material in all the conditions except when the amount of micro-sized Ag was a bit lower than the percolation threshold. The reason was the fact that the micro-sized Ag particles are not continuously connected to each other before percolation threshold concentration and by adding the small amount of silver nano particles, a continues conductive network would be formed. In other cases, adding silver nanoparticles degrades the electrical properties due to the fact that a large number of small particles included in the nano-sized silver colloid inevitably increase the contact resistance. Similar results were also obtained by Ye et al [85] as well as Fan et al [86] while Ye et al proposed that the conductivity of the ECA's containing micro–sized fillers is controlled by constriction resistance (R_{cr}), while the conductivity of nanoparticle containing adhesive is dominated by tunneling resistance (R_t).

It was also shown by Lee et al that the material's resistivity improved significantly by sintering the ECA (at 190°C for 30 minutes). As it is shown in Fig. 2.16, during sintering, due to high surface activity and diffusion of silver nanoparticles toward each other coarsening happens which reduces the contact resistance significantly (resistivity of 5×10^{-5} Ωcm was achieved) [84].

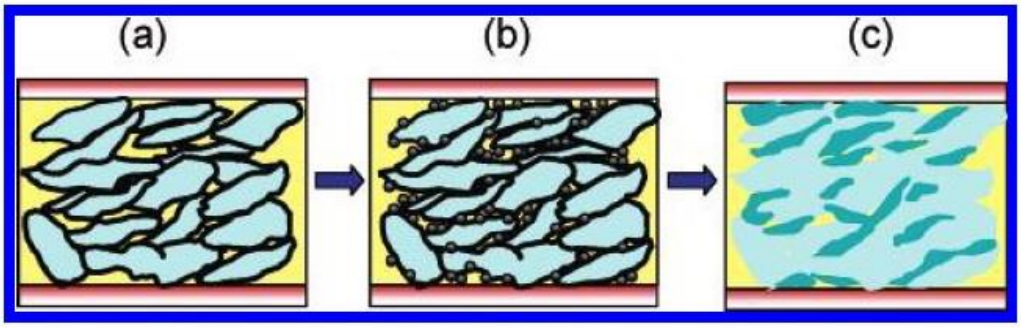

Fig 2.16: (a) ECA with silver flake (b) ECA with both flakes and nanoparticles (c) ECA with sintered nanoparticles among fillers[87]

Jiang et al also studied the sintering behaviour of ECAs containing both silver flakes and nanoparticles and showed that the electrical resistivity reduced after sintering due to fewer contacts between fillers after sintering coupled with the effect of having surfactants on the surface of silver nanowires. The absorbed surfactant helps nanoparticles to disperse in the epoxy resin enabling higher filler loads in the ECA. The surfactant is also deboned from the Ag nanoparticles at a certain temperature and reacts with the silver oxide layer covered on the silver nanoparticles. This reduction process helps the sintering of silver nanowires which decreases the resistance of the ECA [87].

2.3.2 ECAs with silver nanowires

Due to the outstanding physical and chemical properties of one dimensional nanostructures like nanowires, many of recent studies have been focused on these materials [85-87]. In addition to improving the impact strength and adhesion strength [91], silver nanowires provide more perfect conductive networks compared to silver particles as slender nanowires could form a continuous conductive network at a lower amount of filler loads [92]. Wu et al developed and ECA containing silver nanowires and compared it with two other ECAs containing 1µm and 100 nm sized silver particles and found that the ECA exhibited higher shear strength and lower bulk resistivity at lower amount of fillers (56 wt%) compared to two other samples [78]. Fig. 2.17 compares conductive schematic models for different samples where Fig. 2.17(a) illustrates the conductive path for samples containing micrometer sized silver particles and Fig. 2.17(b) stand for the sample with silver nanowires.

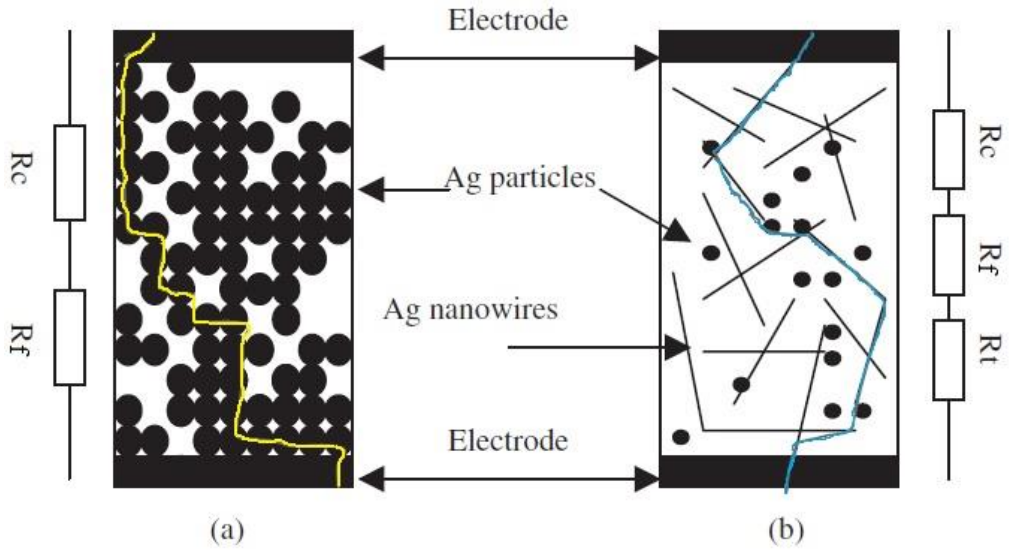

Fig 2.17: Conductive path of ECA containing with (a) micrometer Ag particles (b) Ag nanowires[78]

Comparing the two possible conductive paths in Fig. 2.17 (yellow and blue lines), it is revealed that the yellow line needs more silver particles to form conductive network rather than blue line in the sample containing Ag nanowires. For ECAs containing micrometer sized silver particles, particle-particle resistance (R_c) provides the main part of material resistance due to too many contact points small contact areas between spherical particles. On the other hand, R_c is still the main part in ECAs with silver nanowires however, it is much lower due to larger contact area and fewer contact points. It can also be seen in Fig. 2.17that the tunneling resistance (R_t) is contributed to the total resistance in the ECAs filled with silver nanowires [78].

Functionalizing the surface of nanoparticles/wires with organic surfactants has been studied in the last few years and it has been revealed that it can improve the conductivity of the ICAs significantly [84, 91-92]. The polarities of polymer matrix and inorganic filler is often different which result in particle aggregation during blending of particles/wires with polymer while surface functionalizing of the particles makes the surface of the particles more compatible with the matrix and lets the nanoparticles/wires disperse more homogenously through polymer [87]. Moreover, the surfactant stays on the surface of metallic fillers and prevents the fillers from oxidization during mixing and sintering [95]. Zhang et al used a diacarboxylic acid (pentanedioic acid) to functionalize the nanowires and 3.5% of the pentanedioic acid was remained on the surface of Ag nanowires. TGA

result revealed that the desorption of the acid on the silver surface occurred from 150°C to 250°C [95].

2.3.3 ECAs with graphitic nanofillers

The application of graphitic nanofillers, i.e., carbon nanotubes (CNTs) and Graphene nanopowders, in electrical conductive adhesive field has recently drawn a lot of attention. CNTs, discovered first by Iijima [96], are sheets of graphite which is rolled in to a seamless tube and are classified in to single wall (SWCNT) and multi wall (MWCNT) carbon nanotubes as shown in Fig. 2.18(a) and (b) [97]. Also, graphene is a two dimensional honeycomb flat layer of densely packed carbon atoms while the thickness of the monolayer is around 0.335 nm [98]. Due to the very large surface area and high aspect ratio of CNTs and Graphene nanostructures, a percolated electrical network can be formed with low amount of fillers which lead to low density conductive ECAs [100].

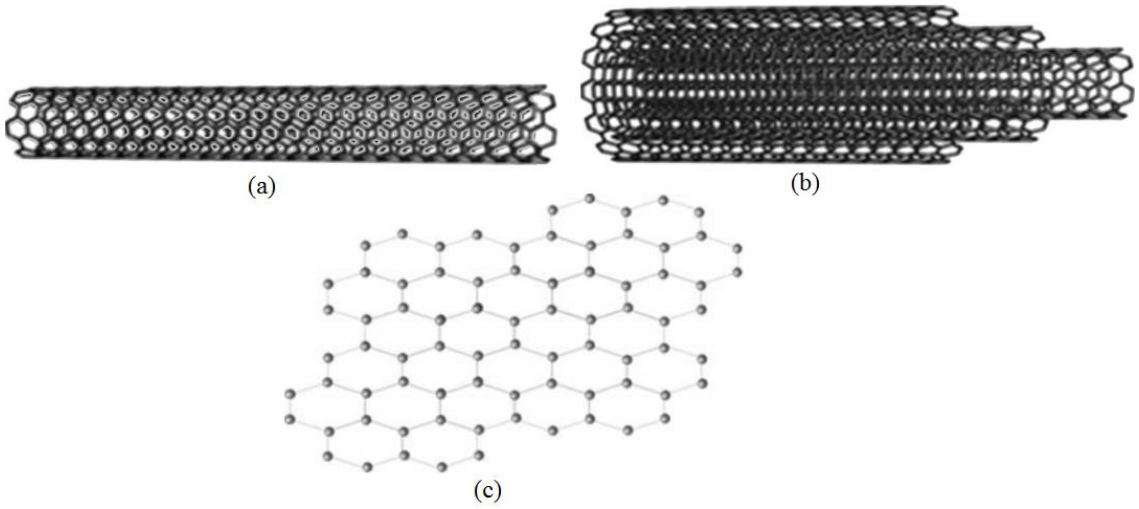

Fig 2.18: (a) Single wall (SWCNT) (b) multi wall (MWCNT) carbon nanotubes [97] (c) Graphene monolayer [99]

Research conducted on ECAs filled with graphitic fillers has shown that when graphitic fillers are used as the main filler, the fabricated nanocomposite suffers from low conductivity compared with advanced ECAs filled with metal fillers [101]. However, due to their large surface area and high

aspect ratio, that would be a very good idea to use them as auxiliary filler in a matrix containing epoxy and silver as the main filler. Xuechun and Feng [102] and Marcq et al. [103], studied the effect of adding MWCNTs to an ECA containing Ag flakes and their results showed a decrease in resistivity down to 1.3 x 10^{-3} Ω.cm and 2 x 10^{-4} Ω.cm; respectively. Luan et al., investigated a nanocomposite containing Epoxy, silver nanowires and 2-D graphene sheets and they obtained an acceptable resistivity of 10^{-3} Ω.cm at very low percolation threshold (20%) [104]. Decreasing the tunneling resistance between the Ag nanowires as a result of graphene nanosheets was reported to be the main reason for the conductivity improvement of the nanocomposite.

As mentioned in session 2.2, the bulk resistance of the fillers (R_f) and the particle-particle resistance (R_c) have the main role in electrical conductivity of the system. Thus, some research has been conducted on using metallic nanoparticles to decorate the graphitic fillers which reduces both R_f and R_c [102-104]. Oh et al. also investigated the effect of functionalizing the decorated CNTs with a di-carboxylic acid which resulted in a very significant improvement in conductivity of the nanocomposite [107]. It is reported that the metallic nanoparticles used as the decorating agent help sintering and coalescing the CNTs to the neighbouring Ag flake while the decorated CNTs act as electrical bridges between separated flakes (Fig 2.19).

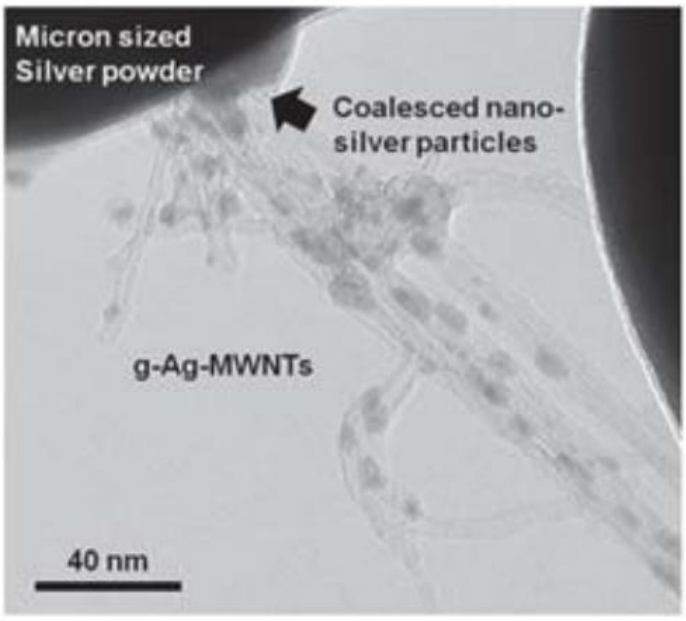

Fig 2.19: The decorated CNTs acting as electrical bridges between separated flakes [107]

As graphene nanosheets have higher aspect ratio along with larger surface area in the matrix compared to CNTs, they are reported to be more effective in improving the conductive network [108]. However, obtaining a homogeneous dispersion of graphene sheets in the epoxy matrix and preventing the agglomeration of the fillers is a challenge which has been tried to be solved by either modifying the surface of graphene sheets using organic materials or decorating the surface of the fillers by inorganic nanoparticles. Both methods are effective in improving the filler dispersion in matrix but the former technique weakens the conductivity of the nanocomposite due to its effect on π electrons delocalization on the surface of the filler [106-109]. The later method was investigated by Peng et al. which revealed an improvement in the conductivity of the nanocomposite, although the final results were not promising [113]. The improvement in the conductivity of the nanocomposite after the addition of Ag NPs-decorated graphene was contributed to the reduction of the tunneling resistance after the addition of the filler; however, this improvement would be cancelled out by the increase in contact resistance due to the extra contacts formed between silver nanoparticles. The contact resistance could be decreased by optimizing the sintering process and coalescing the Ag nanoparticles. Amoli et al. investigated the effect of sintering on conductivity improvement of a hybrid ECA containing silver flakes as well as Ag NPs-decorated graphene [114]. A very low resistivity ($4.6 \times 10^{-5} \Omega.cm$) was reported for the hybrid nanocomposite cured at 220 °C for 2 hrs which was due to a proper sintering of Ag nanoparticles and a significant reduction in the contact resistance (Fig. 2.20).

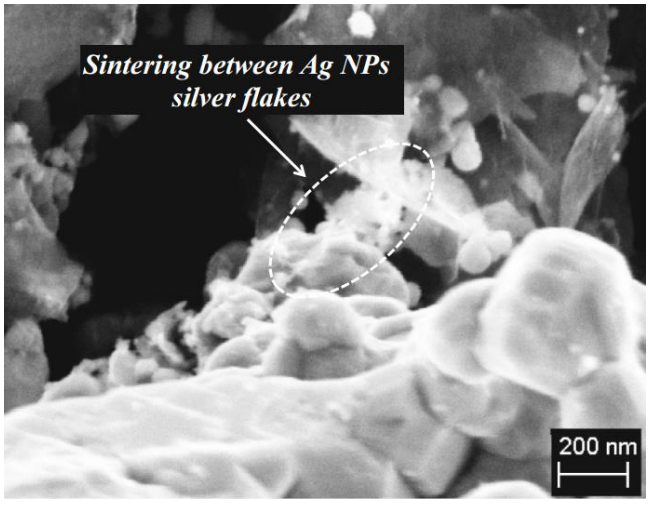

Fig 2.20: The effect of sintering on conductivity improvement of a hybrid ECA [114]

2.4 Findings and Prospects for Applications in Advanced Devices

The above studies on nano inks/composites reveals that they are a very promising option in conductive materials from the aspects of resistivity and fabrication processing. Highly conductive and high resolution patterns could be developed using conductive polymers containing nano-sized fillers. Different conductive materials with their processing techniques are compared to each other in Fig. 2.21. As it is shown in Fig. 2.21, conductive polymers containing nano-sized particles belong to the printable category which is considered a very important advantage of these materials as printing is a low-cost and roll-to-roll process.

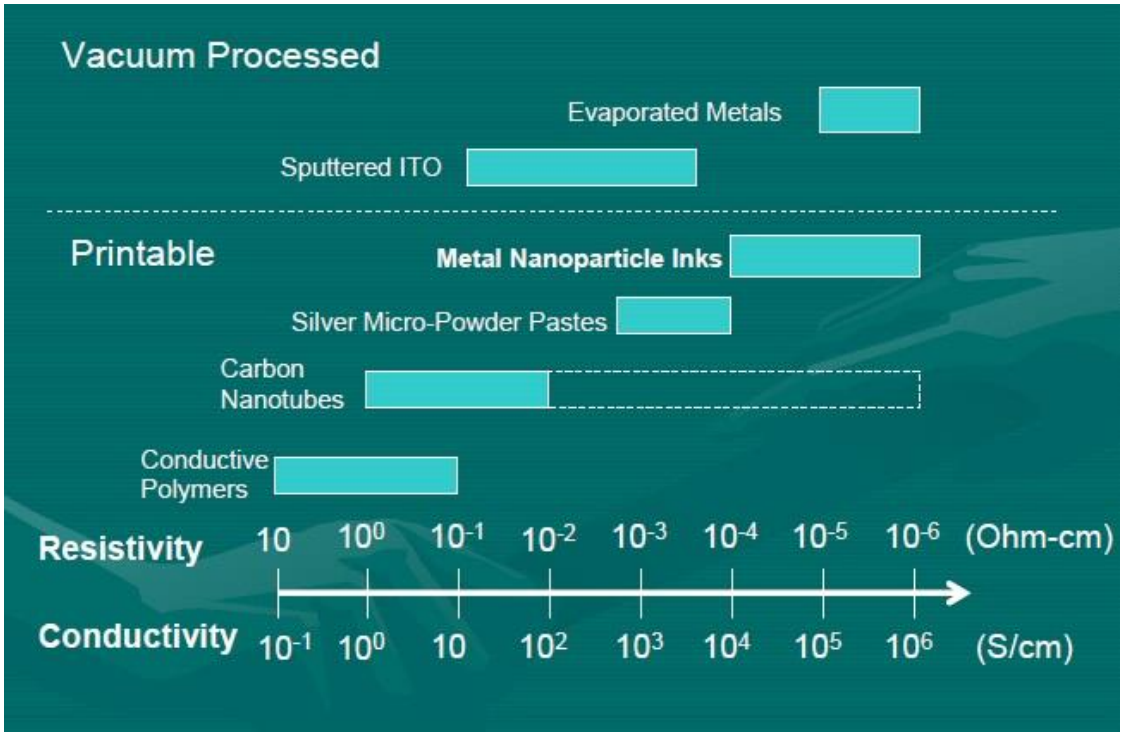

Fig 2.21: A comparison between electrical properties of printable and vacuum processed conductive materials

.

Conductive inks containing nano-sized particles having low processing temperature and high conductivity are finding a wide range of application in the market such as:

- Printed circuit boards (PCBs)

  TFT electrodes and bus-bars in flat panel display backplanes

- EMI Shielding: plasma display, LCD, etc.
- RFID tags
- Electroluminescent lighting
- Touch screens
- High efficiency screen printed solar cells

One other important application for nano conductive materials which has never been considered so far is photovoltaic and particularly in screen printed solar cells. Due to the low processing temperature of the developed conductive nanocomposite, it will cause low amount of bending in firing step allowing generating ultra-thin solar cells. In this research, highly conductive nanocomposites containing silver nanowire and graphene nanopowders are being investigated and developed. The sintering process of the new developed nanocomposite will be thoroughly studied to optimize the electrical property of the material. Work function of the developed conductive nanocomposite will be measured experimentally and will be evaluated theoretically. The new synthesized conductive nanocomposite is used to fabricate screen printed solar cells and will be compared with the conventional cells with Al back contacts.

Chapter 3

Establishing the Basic Screen Printing Process

MSP-485 screen printer in the CAPDS lab was set up by me after going through its manual and designing and ordering the screens as well as calibrating the machine by conducting several runs and printing a conventional metallic paste in trial runs. The metallic paste is a highly conductive silver composition purchased from DuPont Company.

3.1 Screen Printer System

Metallic patterns are printed by the AMI model MSP-485 screen printer accommodating screen frames with the maximum size of 12" ×12" and maximum print area of 8" ×8". Machine was aligned according to manual each time before printing. Other specifics of the machine are given in the Table 3.1.

Table 3.1: Specifics of MSP-485 screen printer

Feature	Description
Screen Frame	Maximum 12" x 12"
Print Area	Maximum 8" x 8"
Part Size	Maximum 8" x 8"
Power	110/115V; 50/60 Hz; 1 phase
Air	min. 80 psi clean, dry air
Width	32"
Length	32"
Height	51"
Weight	550 lbs.
Print Mode	Contact/Off Contact

Squeegee Drive	Aqueous Hydraulic
Squeegee Speed	Up To 10 ips
Squeegee Holder	Up To 8.5", 3/8" Square
Print Head	Mark III Torsion Bar with flood blade
Controls	PLC, flat membrane user interface
Stage	x, y, ø micrometer with vacuum lock
Print Cycles	Print/flood, flood/print, alternate, print/print
Counter	Print cycle

After each set of printing, printer machine as well as screens should be cleaned with Isopropanol (IPA), acetone and clean room wipes. Pastes shouldn't remain on the screen for more than 10 min otherwise it will be dried in the screen and won't come off. MSP-485 screen printer located in CAPDS lab is shown in Fig. 3.1.

Fig 3.1: MSP-485 Screen Printer Machine in the CAPDS lab

A Yamato DX 600 Oven is used for drying the metallic printed paste. Metallic pastes were dried at 180°C for 10 min and an L-9010 RTC belt furnace equipped with Newport controllers also used

to fire the metallic patterns (Fig. 3.2). The belt furnace was used with its maximum speed (41 inch/min) and the temperature profile of the furnace was measured by a thermocouple attached to a USB data logger. The temperature profile result is shown in Fig. 3.3.

Fig 3.2: IR belt furnace in the CAPDS lab

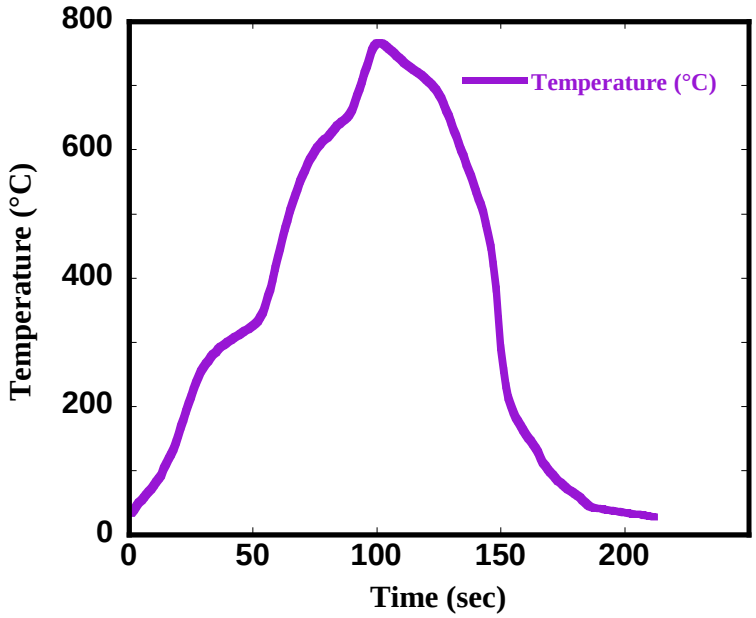

Fig 3.3: Temperature profile of the IR belt furnace

3.2 Design of Screen and Pattern

Two different screen patterns are designed by Corel Draw software for front-side and back-side printing of the wafers (Fig. 3.4 (a) and (b)). Screens are fabricated by SEFAR Company based on the designed patterns using 12" × 12" aluminum frames and stainless steel mesh type. Stainless steel mesh types could give the largest percent open area as well as the best stability of the print size compared to nylon and polyester mesh types. They also peel from large areas easier than other mesh types. The amounts of mesh count and wire diameter are 360 wire/inch and 16 μm (0.0006 inch), respectively. A large number of mesh counts is considered in the ordered screen to make it suitable for extra fine pattern.

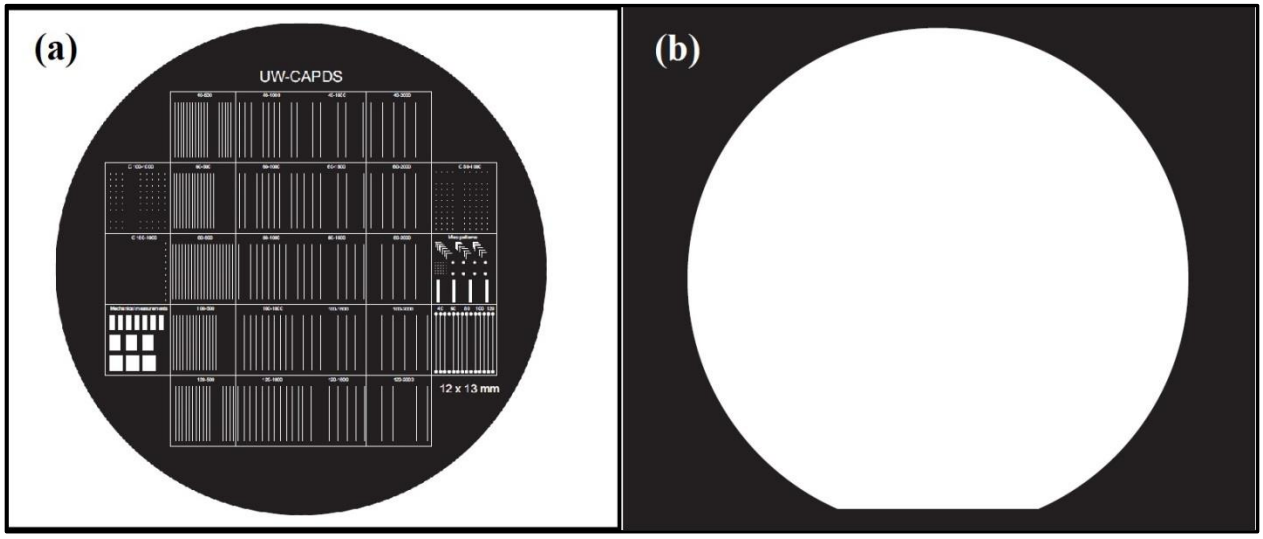

Fig 3.4: Screen patterns (a) front-side (b) back-side designed for 4 inch wafers

3.3 Description of Metallic Paste

To finalize the setting up of the screen printer, a conventional highly conductive metallic paste was utilized to print on silicon wafers. The purchased metallic paste have several benefits such as fast drying and firing, excellent fine line capabilities, high finger line aspect ratio, high electrical conductivity after firing, being suitable for shallow emitter designs (up to 85 Ω) as well as very good shunting control especially for shallower junctions. Typical physical properties of the metallic paste are given in Table 3.2.

Table 3.2: Physical properties of metallic paste

Feature	Description
Viscosity (Pa·s)	240-300
Solids (%) at 750°C	90-92
Fineness of Grind (4th/50%)	<17μm/<5μm
Resistivity (m Ω/sq/10μm)	<5

Metallic paste was screen printed using the screen for the front side. The printed patterns were dried at 180 °C in the oven and then fired in the IR belt furnace. The printed metallic paste after firing is shown in Fig. 3.5.

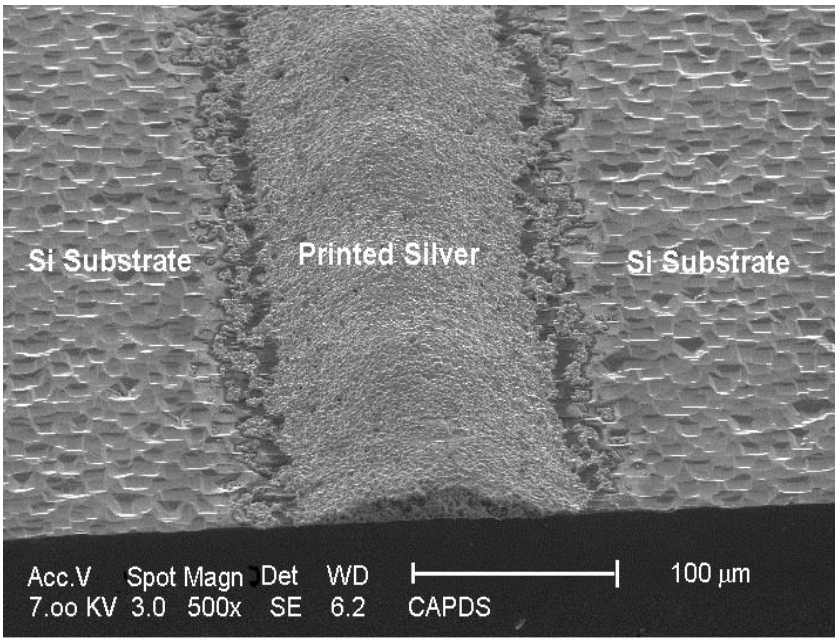

Fig 3.5: Printed metallic paste after drying and firing

Printed patterns were then characterized by Scanning Electron Microscopy (SEM) and Energy-dispersive X-ray spectroscopy (EDAX) analysis. To prepare the SEM samples, printed wafers were cut to small pieces and mounted. Steel clips were used to hold the wafer in the mounting cup. Mounted samples were polished by sand papers and diamond pastes up to 1 micron and then gold

coated with a Cressington 308R coating systems. Silver precipitates formed during firing as well as glass phase are pretty clear in the SEM result depicted in Fig. 3.6.

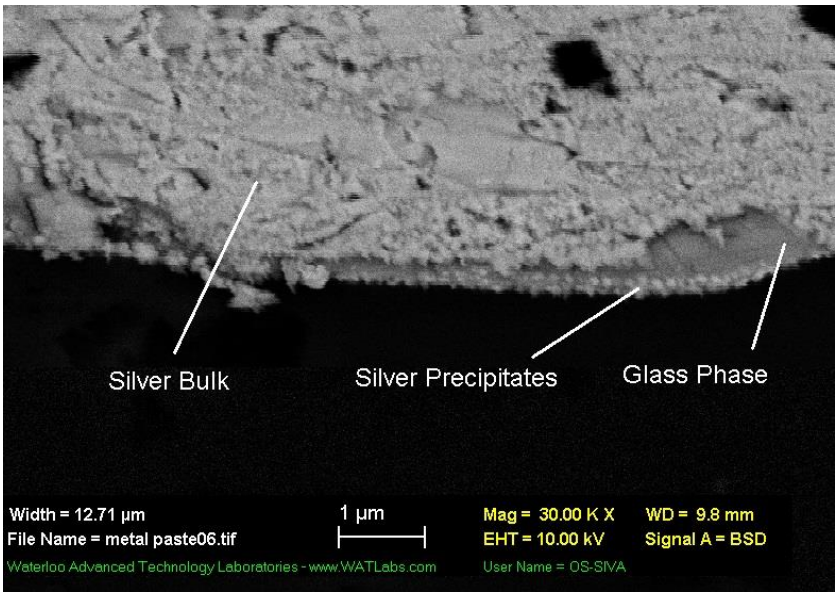

Fig 3.6: Silver precipitates and glass phase in fired metallic paste obtained by Scanning electron microscopy (scale bar is 1 µm)

It can be seen in Fig. 3.6 that three different interfaces are present in the fire sample:

- Ag/thin glass layer/Si
- Ag/thick glass layer/Si
- Ag/Si

To get a better understanding about the chemical composition of metallic phase and perform a quick comparison with glass phase, Energy Dispersive X-ray Spectroscopy (EDAX) analysis is conducted on the sample at two different points: one on the metallic paste and one on the glass phase; results are shown in Fig. 3.7 and 3.8, respectively. As it is shown in the Fig. 3.7, the main phase is silver in the metallic areas far from the interface and small amount of Pb contributed to the glass frits also present. However, comparing to Fig. 3.8, it can be seen that not only the amount of silver in the dark gray phases are reduced significantly, but also there is a notable increase in the amount of Pb confirming the existence of glass phase close to interface.

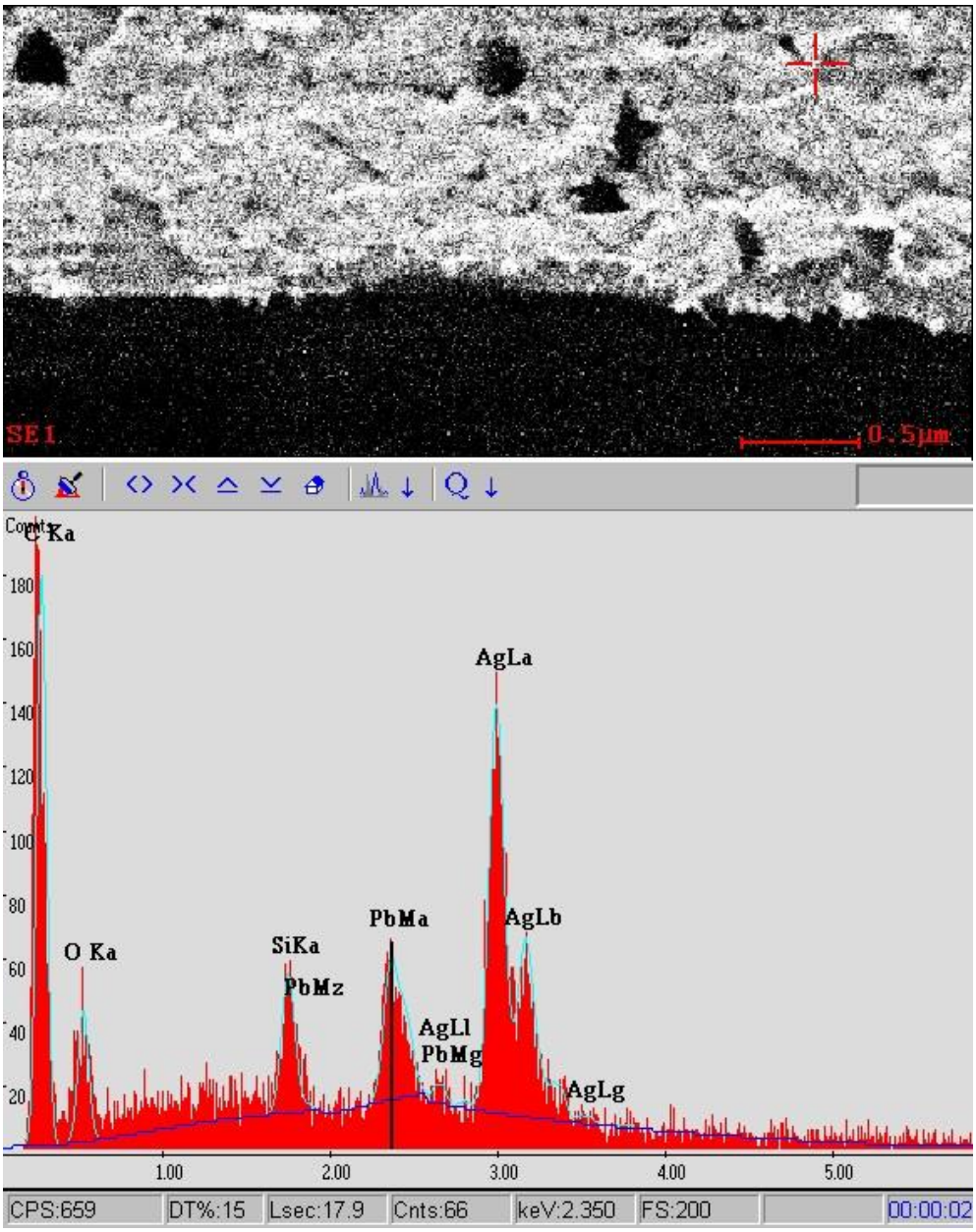

Fig 3.7: EDAX analysis performed on bulk silver of screen printed and fired metallic paste (EDAX is conducted in UW Chemistry Department)

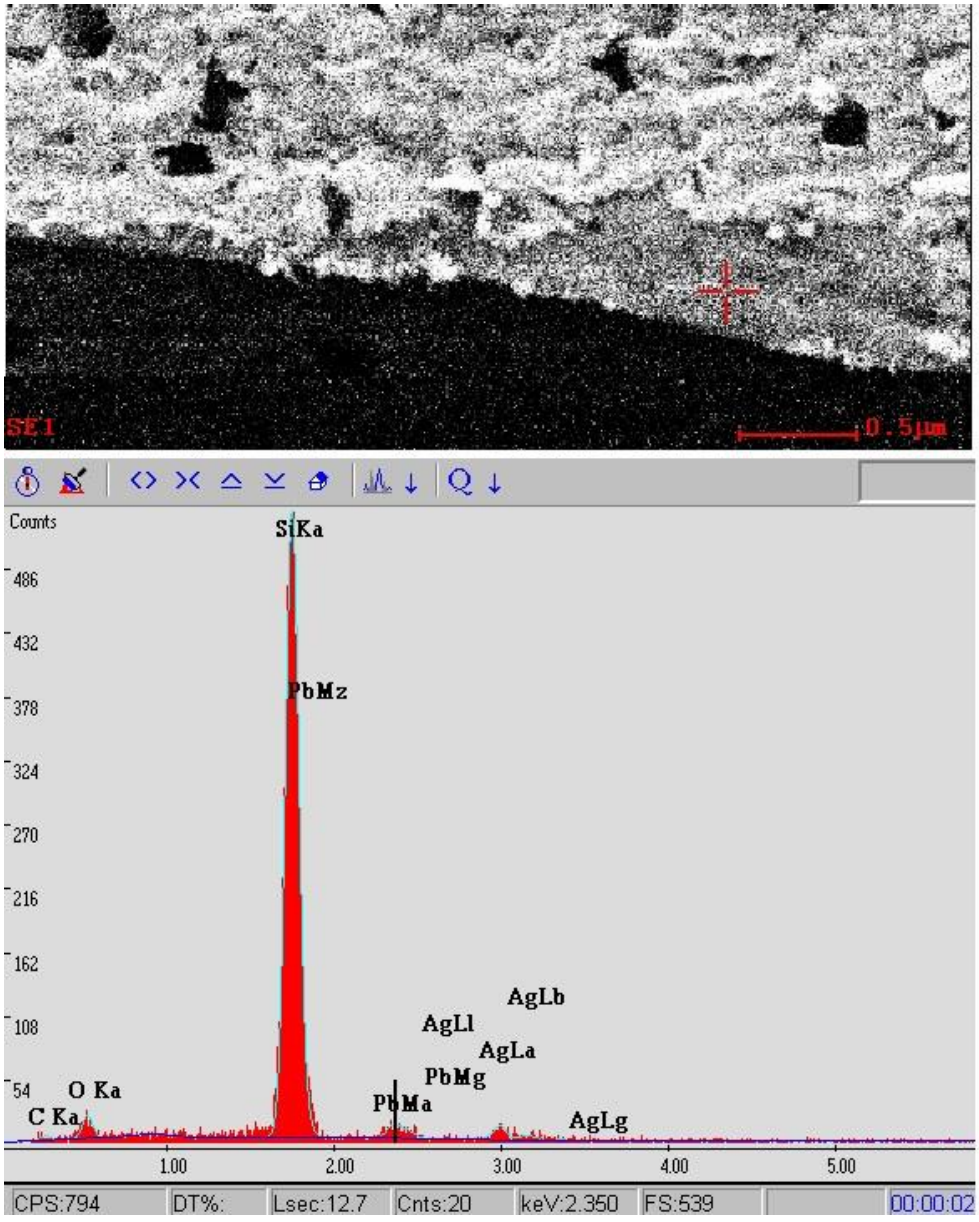

Fig 3.8:EDAX analysis performed on the glass phase of screen printed and fired metallic paste (EDAX is conducted in UW Chemistry Department)

3.4 Conclusion

A screen printing process was established by designing masks compatible to both conventional metallic pastes as well as ECAs. To set up of the screen printer, a conventional highly conductive metallic paste was utilized to print on silicon wafers. The Printed patterns were characterized and results confirmed the proper printing quality. A microstructural analysis using Scanning Electron Microscopy (SEM) as well as Energy Dispersive X-ray Spectroscopy (EDAX) was done on the interface to investigate the curing profile. The presence of the three different interfaces Ag/thin glass layer/Si, Ag/thick glass layer/Si and Ag/Si confirmed that all the required chemical reactions and phase transformation have happened during the curing.

Chapter 4

Developing a Conductive Hybrid Nanocomposite Containing Silver NPs and Silver flakes

4.1 Introduction

As it was reviewed before, the major efficiency limiting and cost determining step in screen printing technology is considered to be metallization part as during the high temperature sintering step, a high amount of thermal budget would be consumed. Presence of the lead is the other concern in the conventional metallic pastes. Therefore, developing an environmentally friendly alternative containing no lead for currently available metallic pastes and conventional Sn/Pb solders has been the topic of interest recently. As it has mentioned in chapter 1 and 2, one alternative for screen printing metallization would be electrically conductive adhesives (ECA) which has drawn attention for electronic packaging applications. Important advantages of ECAs compared to conventional metallic pastes could be summarized as they are more resistant to thermo-mechanical fatigue, applicable for fine pitch patterns and as mentioned above, they are environmentally friendly and have low processing temperature. They are also low price and their processing time is short leading to high efficiency technologies. However, low conductivity and unstable contact resistance are the main disadvantages of these materials.

In this chapter, a brief simulation study is presented to show the bending phenomenon in silicon solar cell during the firing step. The simulation also compared the amount of bending in metallic and ECA printed substrates. Moreover, different conductive adhesives are developed using a polymer medium containing silver flakes as the matrix and silver nanowires as auxiliary conductive filler. Developed nanocomposites are then thoroughly characterized microscopically and electrically. A detailed residual stress analysis was also conducted on the printed substrates.

4.2 Primary Simulation Study

For industrial silicon solar cells, bending of the cell (deflection) due to residual stress produced in firing step is considered as a serious problem. The main reason for the residual stress is the thermal expansion coefficient mismatch of the conductive contacts and the silicon substrate which causes residual stress during cooling in firing step. A schematic illustration of deflection caused by residual stress induced in solar cell during firing is shown in Fig. 4.1 The different expansions force the substrate to bend and the conductive films with the normally higher coefficient of thermal expansion is on the inner side when cooled after firing. Deflection resulted from this residual stress is measured at the center of the silicon wafer from the middle of the substrate to the plane connecting the edges of the wafer as it is shown in Fig. 4.1.

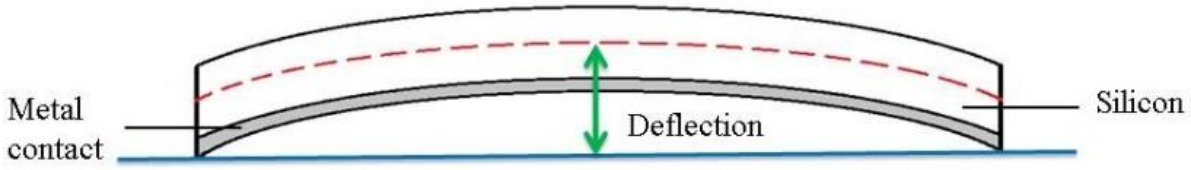

Fig 4.1: A schematic illustration of deflection caused by residual stress induced in solar cell during firing

The amount of bending due to the materials in contact (Si and Ag gridlines in this case) can be represented by a bimetallic strip model and deflection formula can be obtained as [112-113]:

$$\delta = \frac{3(\alpha_b - \alpha_t)(T_f - T_m)(h + H)L^2}{4h^2\,(4 + 6\frac{H}{h} + 4\left(\frac{H}{h}\right)^2 + \left(\frac{E_t}{E_b}\right)\left(\frac{H}{h}\right)^3 + \left(\frac{E_t}{E_b}\right)\left(\frac{H}{h}\right))} \qquad eq.4.1$$

where H is the thickness of Si wafer, h is the thickness of conductive film, α_t and α_b are the thermal coefficient of expansions (TCE) of Si wafer and conductive film respectively, T_f is the firing temperature, T_m is the ambient temperature, E_t and E_b are the elastic modules of Si wafer and conductive film respectively and L is the length of the cell.

The effect of contact thickness and firing temperature on the bending of Si solar cells is modeled based on the Eq. 4.1. Two different conductive materials, silver (Ag) and resin based conductive pastes are considered in the modeling calculations. The simulation results are shown in Fig. 4.2 (a) and (b). The simulation results in Fig. 4.2 (a) show that the amount of bending in Si solar cells

decreases significantly by substituting conventional metallic pastes with ECAs. It also shows that Si solar cells bend more by increasing the metal/resin thickness; however, the amount of deflection is much lower in ECA-printed cells. The effect of wafer thickness on the amount of cell deflection after firing is shown in Fig. 4.2 (b).

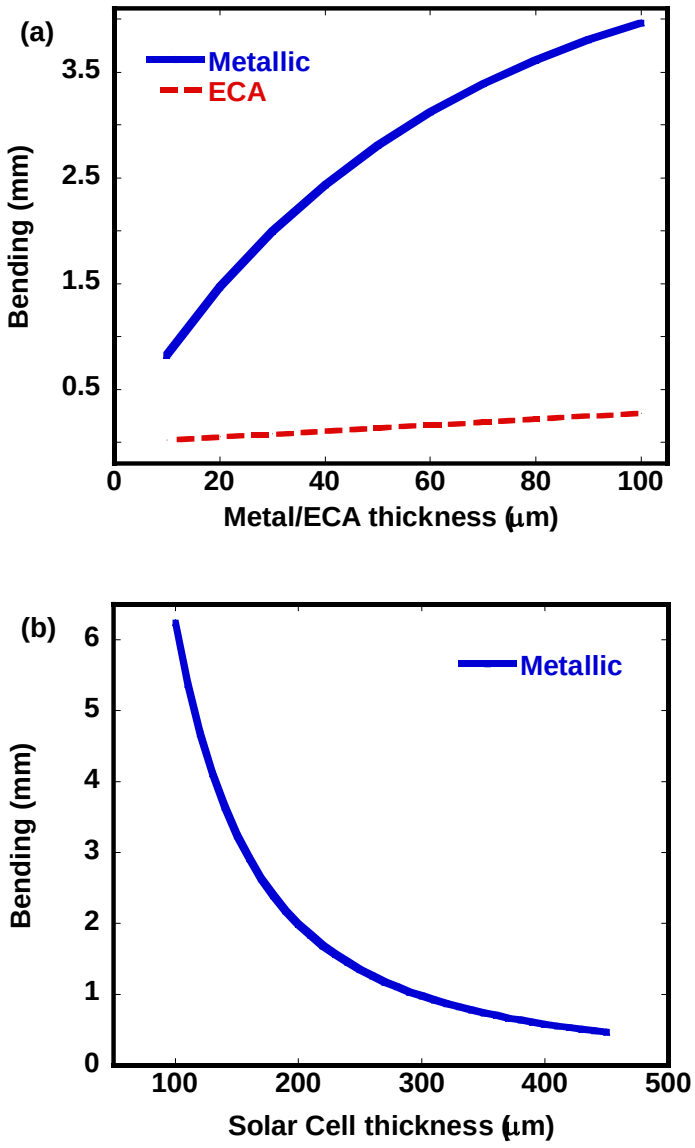

Fig 4.2: Simulation results for bending in metal- and ECA- printed Si wafers

As shown above, the amount of residual stress as well as deflection is directly related to the difference between room temperature and firing temperature, the thickness of the film and substrate. However, it should be noted that the above design of deflected solar cell (Fig.4.1) is a simplistic illustration of the real condition based on the bimetal strip model and the amount of residual stress and deflection also depends on the film area coverage as well.

4.3 Experimental Procedure

Three different conductive pastes, "silver metallic paste", "ECA paste" as well as a "nanocomposite material" are printed by an AMI model MSP-485 screen printer. Silver metallic paste which is a highly conductive silver composition is purchased from DuPont and was previously introduced in chapter 3.ECA paste including resin and hardener is ordered from Transene Company. The resin part contains a thermoplastic copolymer matrix with 65-70 wt% silver flakes. More details on the ingredients of the resin and hardener are given in Table 4.1.

Table 4.1: Resin and hardener ingredients

Resin	Thermoplastic copolymer	$(C_{15}H_{16}O_2.C_3H_5ClO)_x$
		$(C_{36}H_{72}O_6)$
	n-Methylpyrolidone	(C_5H_9NO)
	Silver	Ag
Hardener	Triethanolamine	$(C_6H_{15}NO_3)$
	Piperazine	$(C_4H_{10}N_2)$
	n-Aminoethylpiperazine	$(C_6H_{15}N_3)$
	2,4,6-Trix (Dimethylaminomethyl) Phenol	[(CH3)2NCH2]3C6H2OH

Before Mixing the Polymer media and Ag nanowires, the ECA is printed on silicon wafers and is microscopically characterized with SEM. To prepare the SEM samples, printed wafers were cut to small pieces and mounted. Steel clips were used to hold the wafer in the mounting cup. Mounted samples were polished by sand papers and diamond pastes up to 1 micron and then gold coated with a Cressington 308R coating systems. Microstructure of the ECA is depicted in Fig.4.3.

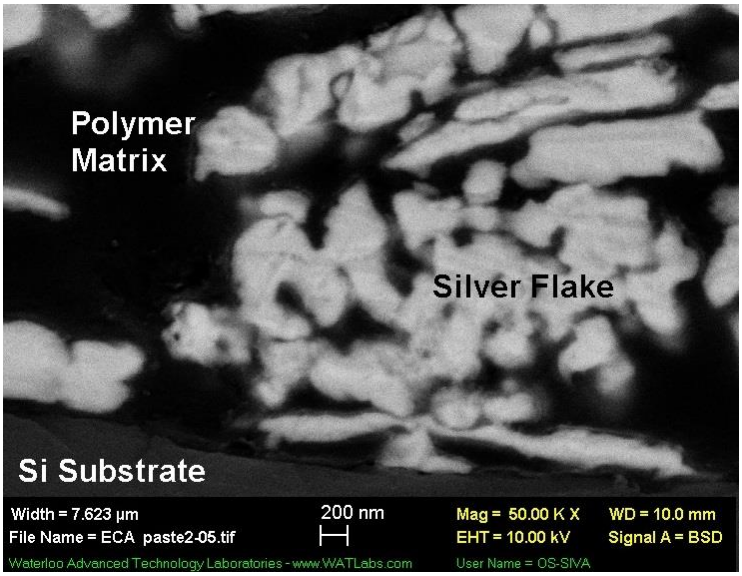

Fig 4.3: ECA microstructure by Scanning electron microscopy (scale bar is 200 nm)

Energy-dispersive X-ray spectroscopy (EDAX) analysis is also conducted on ECA samples shown in Fig. 4.4. EDAX results reveal the chemical composition of the ECA and also confirm that the ECA is lead free.

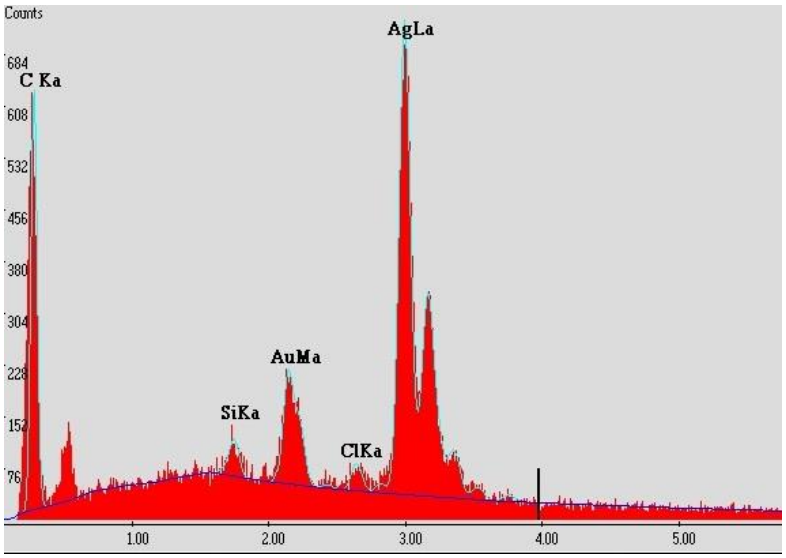

Fig 4.4: EDAX analysis performed on the screen printed ECA

Silver nanowires are purchased from Blue Nano Company. The average size of the Ag nanowires is $35\ nm \times 10 \mu m$ and they are solved in the Isopropanol solvent with the standard density of 10 mg/ml. Specifications of the purchased nanowires are given in Table 4.2 in more detail.

Table 4.2: Specifications of the silver nanowires

Property	Specification
Average Dimensions	35nm x 10 μm
Solvents	Ethanol Isopropanol
Standard Concentration	1.25wt% (ethanol) for sample quantities
Standard Density:	10mg/ml (ethanol) for sample quantities
Molecular Weight	108
Elementary Analysis (not including solvent)	Silver (99.5%+), Carbon (0.03%), Hydrogen (0.23%), Oxygen (0.14%)
Appearance	Gray suspension dispersed in solvent
Polymer Content	Less than 0.5%

The purchased Ag nanowire is characterized by scanning electron microscopy (SEM) as well as Energy-dispersive X-ray spectroscopy (EDAX). A drop of Ag nanowire solution is inserted on a SEM sample holder and dried at room temperature under vacuum for 24 hours. SEM and EDAX analysis results are shown in Fig.4.5 and 4.6, respectively.

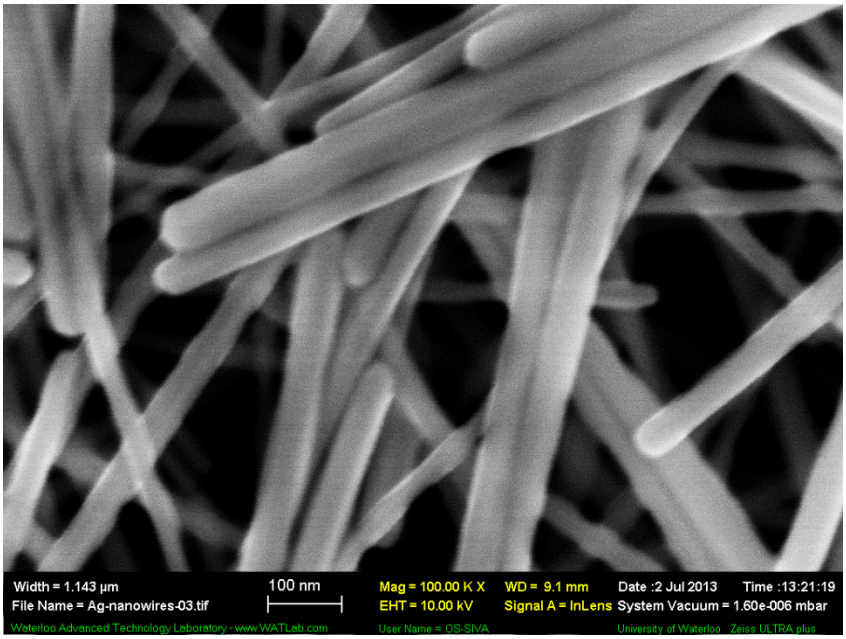

Fig 4.5: Scanning electron microscopy of Ag nanowires morphology (scale bar is 100 nm)

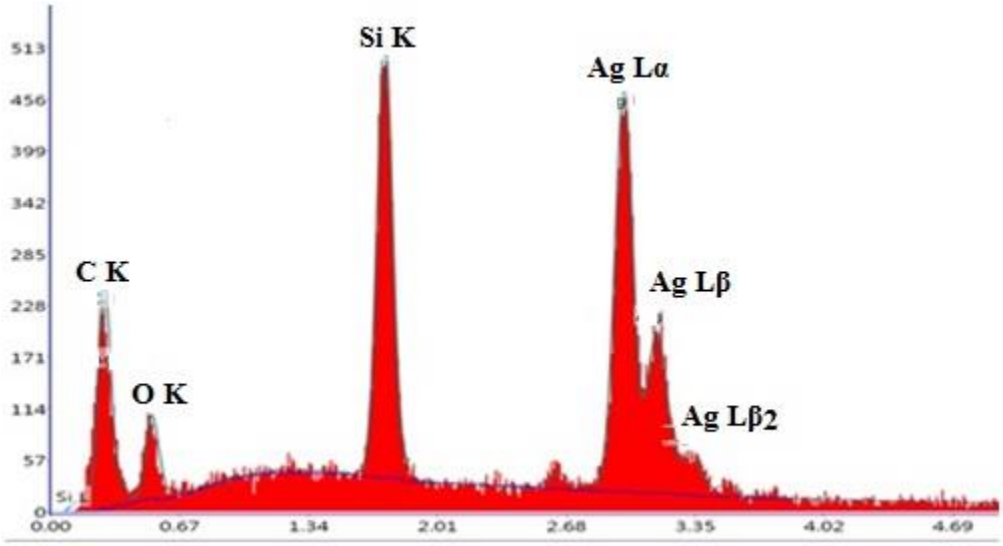

Fig 4.6: EDAX analysis performed on Ag nanowires

Silver nanowires with a weight fraction of 0.05% and 0.1% were added to the resin part of the ECA. It was experimentally observed that the viscosity of the final nanocomposite containing 0.05 wt% Ag nanowires was proper for printing fine and clean patterns but the nanocomposite containing 0.1 wt% nanowire wasn't viscous enough so in the case of the nanocomposite with 0.1

wt% nanowires, Ag nanowire solution was centrifuged with an Eppendorf Centrifuge model 5810 before the mixing step and half of the solvent was removed from the top.

After adding the Ag nanowires to the ECA, the new nanocomposite was stirred manually for two minutes and then mixed for 10 minutes using a Cole-Parmer ultrasonic bath. For mixing the new resin and hardener before printing the nanocomposite, the ratio of the mass of developed nanocomposite to the ratio of the hardener is 100 to 2.5 and the mixture is stirred manually for one minute.

To sinter the printed metallic patterns, an L-9010 RTC belt furnace was used while ECA and nanocomposite films were cured at 100°C in an oven for two different curing times: 10 minutes and 1 hr.

Conductive patterns were analyzed and compared to each other electrically, mechanically and microscopically. Conductivity of the printed patterns was calculated from the bulk conductivity of the screen printed material which was measured using dark IV and following equation:

$$\sigma = LI/Vwt \qquad eq.3.2$$

Where L, w and t are length, width and thickness of the printed film. $V$and I are also the values of voltage and current defined by the source measure unit (SMU). Dimensions of the printed patterns were measured by a Dektak 150 surface profiler. The surface profiler was also utilized to measure the amount of deflection as well as induced residual stress in the cured printed wafers. Finally, Scanning electron microscopy (SEM) is performed to study and compare the microstructure of different conductive films.

4.4 Results and Discussion

4.4.1 Morphology and electrical characterization

Based on the concentration of silver nanowires and curing time, several printed films are developed as depicted in Table 4.3. After synthesizing the samples and screen printing the patterns, SEM samples were prepared from cross section of the printed films. SEM results of ECA paste as well as nanocomposite samples containing 0.05 wt% and 0.1 wt% of silver nanowires (NCOMP-0.05wt%Ag and NCOMP-0.1wt%Ag) are shown in Fig. 4.7(a) and (b).

Table 4.3: Specifications of the printed films

Samples	Ag nanowire (wt%)	Curing time (min)
Metallic Paste	-	-
ECA	0	10
ECA-2	0	60
NCOMP-0.05wt%Ag	0.05	10
NCOMP-0.05wt%Ag-2	0.05	60
NCOMP-0.1wt%Ag	0.1	10
NCOMP-0.1wt%Ag-2	0.1	60

According to Fig. 4.7, silver flakes have the main role in developing the conductive network in both samples. In nanocomposite samples, silver nanowires are not very clear in the epoxy matrix due to their significantly lower concentration in nanocomposites in comparison with the concentration of silver flakes in the ECA paste (0.05 wt% and 0.1 wt% compared to 65-70 wt%, respectively); however, a few of them are shown in Fig. 4.7 (a) and (b) by the red circles. Also, during the nanocomposite synthesis, sonicator is used to mix the nanowires and epoxy which causes the breakage of the nanowires in to very small pieces. This could be another reason for not being able to see nanowires clearly in the nanocomposites. Although, in the nanocomposite containing 0.1 wt% nanowires, these small broken conductive particles are more clear.

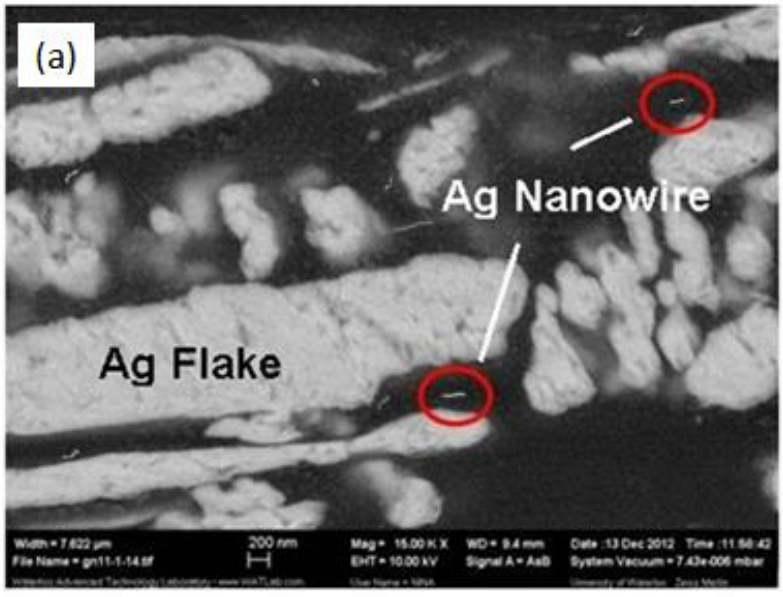

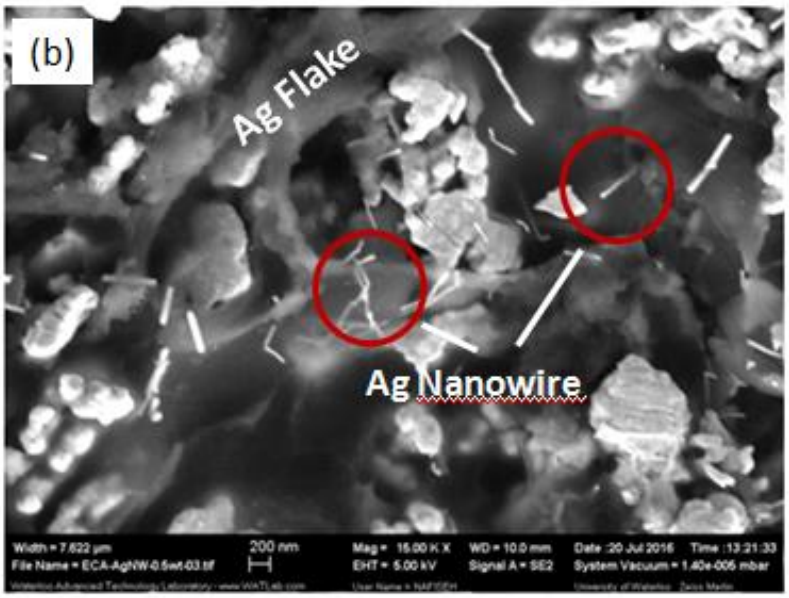

Fig 4.7: SEM analysis of (a) NCOMP-0.05WT%AG and (b) NCOMP-0.1WT%AG

In order to characterize samples electrically, conductivity measurements were performed on the printed patterns using dark IV and surface profiler (Table 4.4).Comparing the conductivity of printed patterns cured for 10 min ((ECA, NCOMP-0.05wt%Ag and NCOMP-0.1wt%Ag), it can be seen that after adding 0.05 wt% and 0.1 wt% of Ag nanowires to the ECA, conductivity of the nanocomposite improves significantly (61% and 69% respectively). Table 4.4 also reveals that increasing the curing time in the nanocomposite filled by silver nanowires decreases the conductivity of the material.

Table 4.4: Measured conductivity of different nanocomposites

nanocomposite	Bulk conductivity (Sm-1)
ECA	5.95×10^4
ECA-2	1.19×10^4
NCOMP-0.05wt%Ag	1.55×10^5
NCOMP-0.05wt%Ag-2	1.15×10^5
NCOMP-0.1wt%Ag	1.93×10^5
NCOMP-0.1wt%Ag-2	2.99×10^4

Both main theories for conduction mechanism, "percolation threshold theory" and "tunneling effect or field emission", are considered to analyze the effect of silver nanowires on conductivity behaviour of the nanocomposite. Percolation threshold theory is based on forming a conductive network in the matrix due to the contacts between flakes at a critical amount of the filler content. As it was shown in Fig. 4.7(a) and (b), because of the low concentration of silver nanowires as well as their small sizes, their impact in physical connecting of silver flakes is negligible. Therefore, the second theory (tunneling effect) is utilized to explain the conductivity improvement of the nanocomposite after adding the silver nanowires. In tunneling effect theory, electrons in one filler can diffuse in to the potential barrier and get to the next particle forming a conductive channel in the matrix. So, in our nanocomposite samples, the tunneling effect of the scattered silver nanowires located between the silver flakes could be responsible for the improvement in the conductive.

4.4.2 Residual Stress Analysis

The amount of residual stresses and bending induced in the wafers after firing of Metallic paste, ECA as well as NCOMP-0.1wt%Ag printed samples are measured and compared to each other. The study was also extended to wafers with different thicknesses in the range of 100 - 600 μm.
Values of residual stress induced in metallic, ECA and as NCOMP-0.1wt%Ag printed wafers after firing processes are measured using the surface profiler and plotted in Fig.4.8. As it is shown in Fig.4.8, the amount of residual stress in ECA and nanocomposite is close to each other; although, their residual stress is much lower than the metallic paste one.

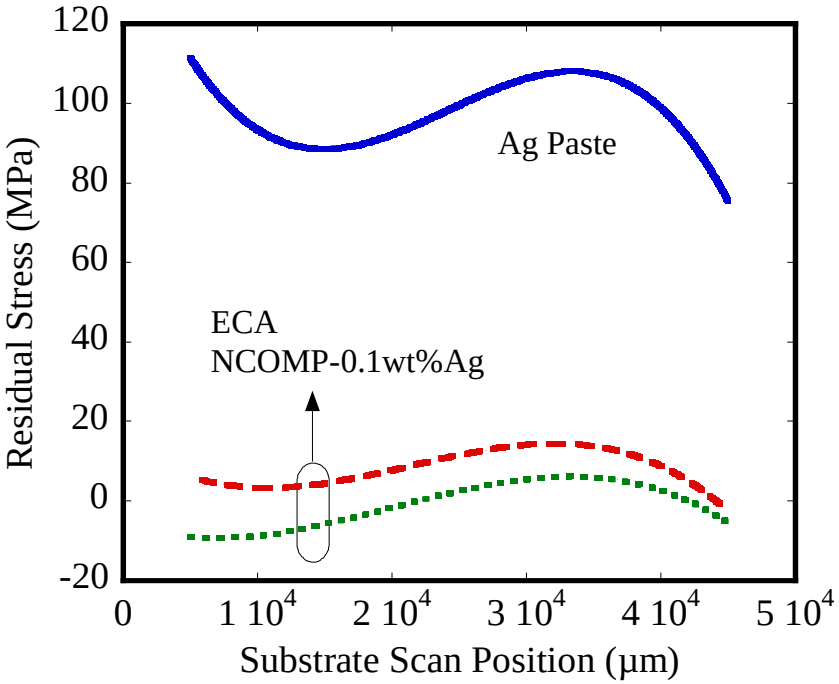

Fig 4.8: Residual stress in metallic, ECA and NCOMP-0.1wt%Ag printed wafer

The maximum and average values for measured residual stresses are shown in table 4.5. It can be seen that both maximum and average values of the residual stress induced in the metallic printed wafers are significantly higher than the ECA and NCOMP-0.1wt%Ag ones.

Table 4.5: Average and maximum of residual stress values

Printing material	Max. residual stress (MPa)	Ave. residual stress (MPa)
ECA	14	8
NCOMP-0.1WT%AG	6	9
Metal	109	97

In order to analyze the effect of substrate thickness on the induced residual stress in printed wafers, the evolution of residual stress is measured in all the samples using the surface profiler and results are shown in Fig. 4.9(a) and (b). Results reveal that the smaller the thickness, the induced residual stress would be significantly higher in metallic-printed wafers while the difference between residual stresses in ECA as well as NCOMP-0.1wt%Ag printed wafers is very small and effect of

thickness is almost negligible. This result confirms one important advantage of ECAs as well as the novel nanocomposite which would enable solar cell manufacturing to use ultra-thin wafers. Using thin wafers in manufacturing has drawn attention to use the expensive Si material more efficiently. More proper cell designs with higher efficiencies would be achieved with decreasing cell thickness. However, one important limiting issue regarding the use of thin cells is that thinner solar cells tend to present higher amount of bending after firing process. So, considering above results on the amount of residual stress in NCOMP-0.1wt%Ag printed wafers, the novel nanocomposite could be a promising alternative for high efficiency ultra-thin substrates.

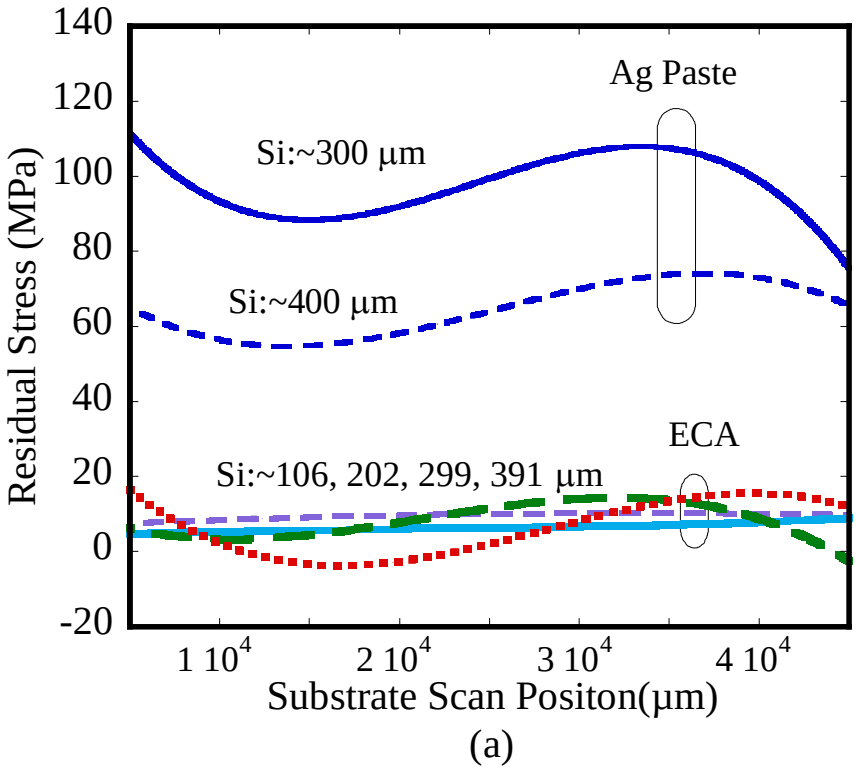

(a)

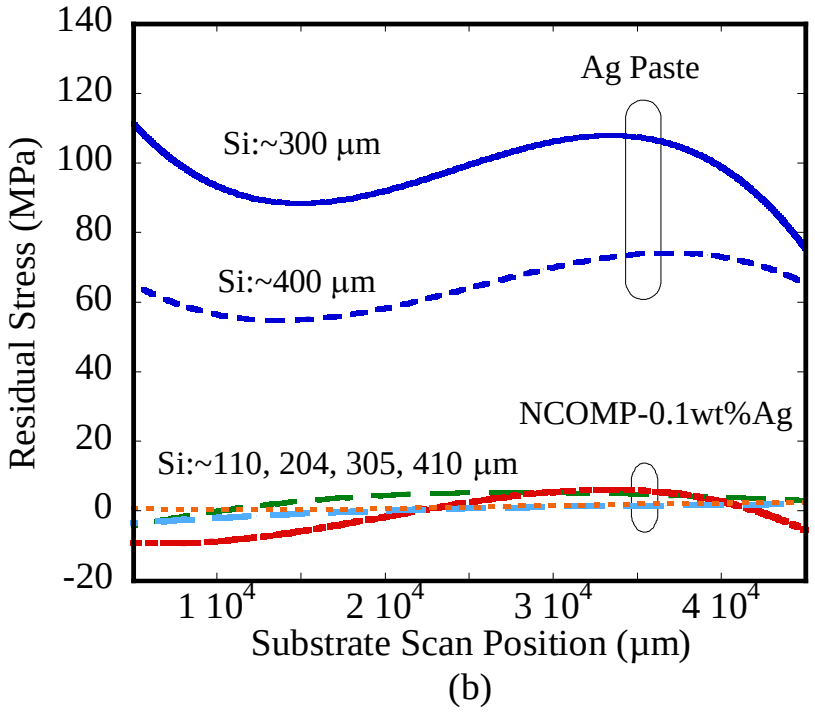

Fig 4.9: Effect of thickness on the amount of residual stress

The amount of bending in printed substrates is also measured using the surface profiler. Profiler gives the radius of curvature for printed wafers. The amount of bending (d) is calculated as

$$d = R \times (1 - \cos(L/2R)) \qquad eq.4.1$$

Where R is radius of curvature and L is arc length (Fig.4.10).

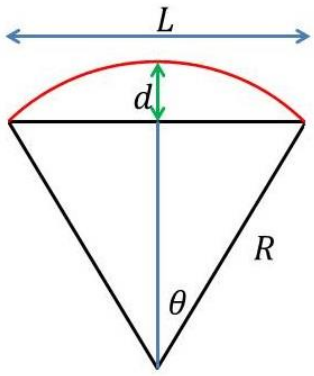

Fig 4.10: Arc geometry

The amount of bending in ECA, NCOMP-0.1wt%Ag and metallic printed wafers is depicted in Fig.4.11. It can be seen that by increasing the thickness, the amount of bending decreases in all three samples; however, the deflection is significantly lower in ECA and NCOMP-0.1wt%Ag samples compared to the metallic printed one. The breakage was high in metallic printed wafers with thicknesses below 200 μm and they broke during the sintering due to excessive amount of bending while ECA and NCOMP-0.1wt%Ag printed wafers with thicknesses up to 100 μm made it successfully through the curing process. Therefore, the novel nanocomposite induces less amount of stress and bending on the cell and could enable industry to use thinner wafers in solar cell modules. In the case of NCOMP-0.1wt%Ag nanocomposite, not only its conductivity is higher than ECA, but also the amount of bending and also residual stress are even lower than ECA and metallic paste which confirms that the new developed nanocomposite could be a promising alternative in electronic packaging as well as screen printing metallization.

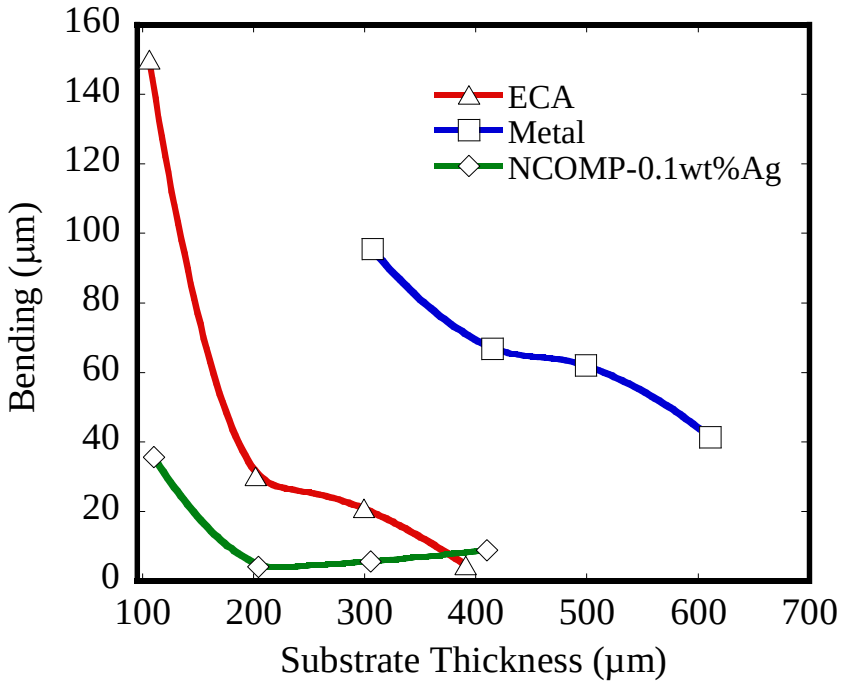

Fig 4.11: Bending in ECA, nanocomposite and metallic printed wafers

4.5 Conclusion

Different conductive adhesives were synthesized and screen printed on silicon wafers. Two different curing times (10 and 60 minutes) were considered to dry and sinter the adhesives. Conductivity measurements revealed that addition of even a very low amount of silver nanowires (0.05 wt%) could decrease the resistivity and improve the conductivity of the nanocomposite for around 62%. Morphology characterization analysis confirmed the influence of silver nanowires in improving the electrical properties of the paste due to their breakage and scattering among silver flakes. SEM images as well as conductivity measurements also suggested that the conductive mechanism could be tunneling effect between small silver particles. Comparing the values of the resistivity of the samples cured at different times did not show an improvement in the conductivity of the nanocomposites which could be due to the presence of coarsening and lower number of small particles would remain in the matrix to be involved in tunneling effect theory. Thus, decreasing the conductivity by increasing the curing time could also show that tunneling effect is the dominant mechanism for transferring the electrons in the paste.

Residual stress analysis also revealed that the amount of residual stress induced in substrates is much lower in nanocomposite and ECA printed wafers in comparison with metallic printed ones. Also, the amount of increase in residual stress by decreasing the wafer thickness was small in the case of using nanocomposite and ECA paste compare to the metallic paste. Moreover, it was shown that the amount of bending increased with decreasing the thickness of substrate in all three cases; however, it was much lower in nanocomposite printed wafers confirming that the new developed nanocomposite could be a promising alternative in screen printing metallization.

Chapter 5

Developing a Highly Conductive Graphene Decorated Nanocomposites

5.1 Introduction

As it was reviewed in chapter 2, developing alternative conductive printable materials to currently available metallic pastes and conventional Sn/Pb solders have been the topic of interest in electronic packaging and solar industry. In silicon solar cell industry a shift towards ultra-thin wafers is a seriously considered option for cost reduction. As illustrated in chapter 4, stress induced by conventional printed metal electrodes can cause wafer "bowing" and breakage during module lamination process, limiting the scope of using ultra-thin wafers in solar cell manufacturing. Also flexible and large area electronic applications will require new, low thermal budget schemes for electrode formation. Moreover, alternate electrode materials can also contribute to the ongoing effort to achieve lead-free metallization schemes. As it was shown in chapter 4, electrically conductive adhesives (ECA) which have drawn attention for electronic packaging applications can provide a possibility to replace conventional metallic pastes in screen printing technology. In fact, their low firing temperature will reduce the induced residual stress as well as diffusion rate of conductive material into semiconductor material. These characteristics of ECAs have the potential to enable them for use in thin substrate devices. However, their low conductivity is considered to be the main disadvantage of these materials. As depicted, two different nanocomposites were developed in the previous chapter using an ECA as well as Ag nanowires and experimental results showed a significant improvement in the conductivity of the nanocomposite; however, it was seen that increasing the amount of the silver nanowires couldn't improve the conductivity anymore. Also, the lower amount of induced residual stress and deflection in the substrate after curing and firing of the printed materials compared with the results from conventional metallic paste confirmed that the developed nanocomposites could be a promising option for ultra-thin electronic devices. However, despite the fact that conductivity of the nanocomposite got improved for around

60%, its value still lower than the conductivity of the conventional silver paste and Aluminum used in the solar cell fabrication or printed electronics. Two essential ways to improve the conductivity of ECAs is by optimizing the curing profile and increasing the curing shrinkage as well as introducing nanomaterials in the polymer matrix. Many studies have been focused on one dimensional nanostructure fillers like silver nanowires as it was experimented in the previous chapter. On the other hand, as reviewed in the background, two dimensional graphene sheets with outstanding electrical and structural properties have attracted researchers during the last few years and could be used to improve the electrical properties of the ECAs.

In this chapter, screen printable nanocomposites are developed by introducing graphene nanopowders into the ECA to achieve higher conductivity. Material synthesis and curing profile are optimized to improve the electrical property of the developed nanocomposites. Different characterization techniques are utilized to study the thermal stability and conductivity of the developed materials. Also, the amount of bending and induced residual stress on wafers printed with the nanocomposite are studied and compared with the previously obtained results in chapter 3.

5.2 Materials Used

For the preparation of nanocomposites, the commercial ECA paste from Transene was used as the base material. Graphene nanopowders with an average flake thickness of 12nm were used as additives for the preparation of the Graphene decorated nanocomposites (NCOMP-GN). The scanning electron microscope image in Fig. 5.1 show the graphene used. P-type Si wafers with the thicknesses in the range of 100 - 600 μm as well as glass slides were used as substrates for printing the nanocomposites.

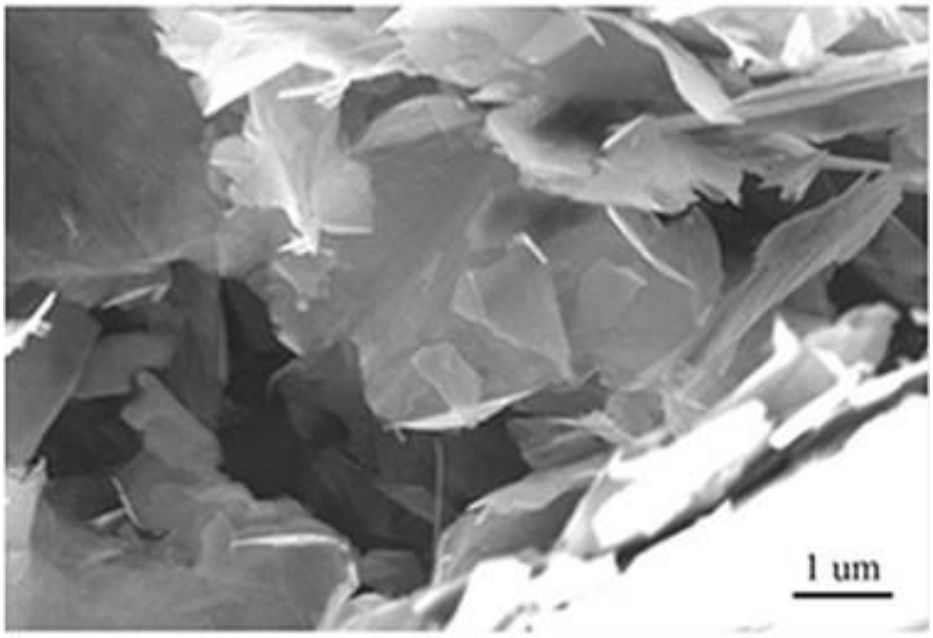

Fig 5.1: Scanning electron micrographs of graphene nanopowders

To synthesize the NCOMP-GN nanocomposite, graphene nanopowders with weight fractions of 1 wt% and 3 wt% were added to the base resin. To mix the graphene and resin, mechanical mixing using a Vortex mixer as well as sonication in a Cole-Parmer ultrasonic bath were considered but due to the large weight fraction and volume fraction of the graphene nanopowders, the mixing procedure needs to be optimized. The nanocomposite with larger amount of graphene (NCOMP-3wt%GN) was picked to analyze and optimize the mixing procedure. This way, the optimized mixing procedure would be proper for the nanocomposite with lower amount of filler (NCOMP-1wt%GN) graphene. To optimize the mixing procedure, mechanical stirring and sonication was performed for different duration times and the material was doctor bladed on a clean glass and cured. To keep the optimization condition consistent, all samples were cured at 150°C for 10 minutes and then 20 minutes of Vortex plus 1hr of sonication was selected as the starting point. 4point probe technique was used to measure the electrical resistivity of the samples. Table 5.1 shows effect of different sonication times on the resistivity of the samples.

Table 5.1: Sonication time optimization

Sonication time (hr)	Electrical Resistivity
1	2.65E-05
5	3.14E-05
10	2.61E-05
15	3.44E-05
20	3.15E-05

As shown in the Table 5.1, increasing the sonication times doesn't have a positive effect on improving the conductivity of the material and consequently, 1 hour of sonication is selected as the optimized sonication time. Also, the effect of increasing the Vortex (mechanical stirring) time on the resistivity of the sample was investigated and as Table 5.2 shows, 20 mins of vortex is giving the best results. It should be noted that the reported results are the average of three repeated tests performed at the same condition.

Table 5.2: Mechanical mixing time optimization

Vortex time (min)	Electrical Resistivity
0	4.63E-04
20	2.65E-05
40	3.61E-05
60	3.751E-05

As per the above results, nanocomposite samples were mechanically stirred for 20 minutes in the Vortex mixer and then sonicated for 1 hour in a Cole-Parmer ultrasonic bath. To help with the dispersion of graphene in the matrix, high purity isopropanol was added at 0.2 ml / 1wt% of graphene. Hardener was then added to the nanocomposites right prior to printing. Despite the low weight percentage of graphene, it is expected that its high volume fraction would affect the polymer chains and post-printing curing reactions, as would be shown by the curing kinetics studies.

5.3 Preparation of Test Structures

A screen-printing system (AMI model MSP-485) accommodating screen frames with the maximum size of 12" ×12" and maximum print area of 8" ×8" was used to print the films on 4-

inch silicon wafers. To print smaller patterns onto glass substrates, an in-house built mold with dimensions 7mm×7mm×100μm was used. Samples with printed ECA and NCOMP-GN patterns were dried and cured in a Yamato DX 600 oven.

5.4 Characterization Methods

Differential Scanning Calorimetry (DSC): DSC is a useful method to analyze the chemical or physical transformation processes by measuring the exothermic or endothermic heat flow which could determine the reaction kinetics, i.e., corresponding temperatures and reaction times. The differential heat flow between the sample and a reference material is monitored in this method. The DSC measurements on 10-15 mg samples of NCOMP-GN nanocomposites were performed using a Modulated DSC-Q-2000 (TA Instrument) system. Isothermal DSC was performed at three different temperatures of 100°C, 125°C, and 150°C to investigate the curing kinetics. Thermal stability of the ECA and NCOMP-GN samples was also studied in dynamic-mode DSC with a heating rate of 10°C/min.

Thermogravimetric Analysis (TGA): For the TGA measurements, a TGA-Q500 thermogravimetric analyzer with a heating rate of 10°C/min was used. TGA, by determining the weight change in response to temperature variation, allows studying the thermal decomposition of materials. A derivative thermogravimetric (DTG) loss is normally used to determine the temperature range with the most apparent weight loss. The measurement and analysis were performed on the nanocomposite samples with the temperature varied from 25°C to 650°C.

Electrical Conductivity: To measure the electrical conductivity of the nanocomposites, 100 μm thick films with different compositions were printed on glass substrates and cured. Measurements were done in a Jandel RM2 four point probe. A shape correction factor of 4.0095 was applied to calculate the sheet resistivity as described in [118].

Wafer deflection and Stress: The Dektak 150 surface profiler was utilized to measure the amount of deflection induced on 4-inch diameter Si wafers printed by ECA and NCOMP-GN. Wafers with different thicknesses chemically etched to different target thicknesses (100 – 600 μm) were used. In the measurement, carried out in a fixed-stylus, moving-sample mode, the curvature of the substrate was recorded along the same locations before and after film deposition and thermal treatment. The profiler gives the radius of curvature and the amount of bending (d) is calculated as $d = R \times (1 - \cos(L/2R))$ where R is radius of curvature and L is arc length.

5.5 Results and Discussion

5.5.1 Curing kinetics in Material Synthesis

The isothermal DSC results performed on the synthesized NCOMP-GN samples (NCOMP-1wt%GN and NCOMP-3WT%GN) are shown in Fig. 5.2(a) and 2(b) revealing that for both weight percentages, nanocomposites cured at 150 °C have the highest degree of curing. Since curing causes shrinkage in the network and decreases the tunneling and constriction resistances, the nanocomposites cured at 150 °C are expected to have relatively lower resistivity. One can also observe that no heat is generated after a period of 10 minutes which means that the curing process is complete. Also, the maximum heat flow of the curing peak is higher in the 1wt% graphene samples than 3% ones. This is because of the higher amount of fillers in NCOMP-3wt%GN interfering with the polymer branches and leading to a lower degree of curing.

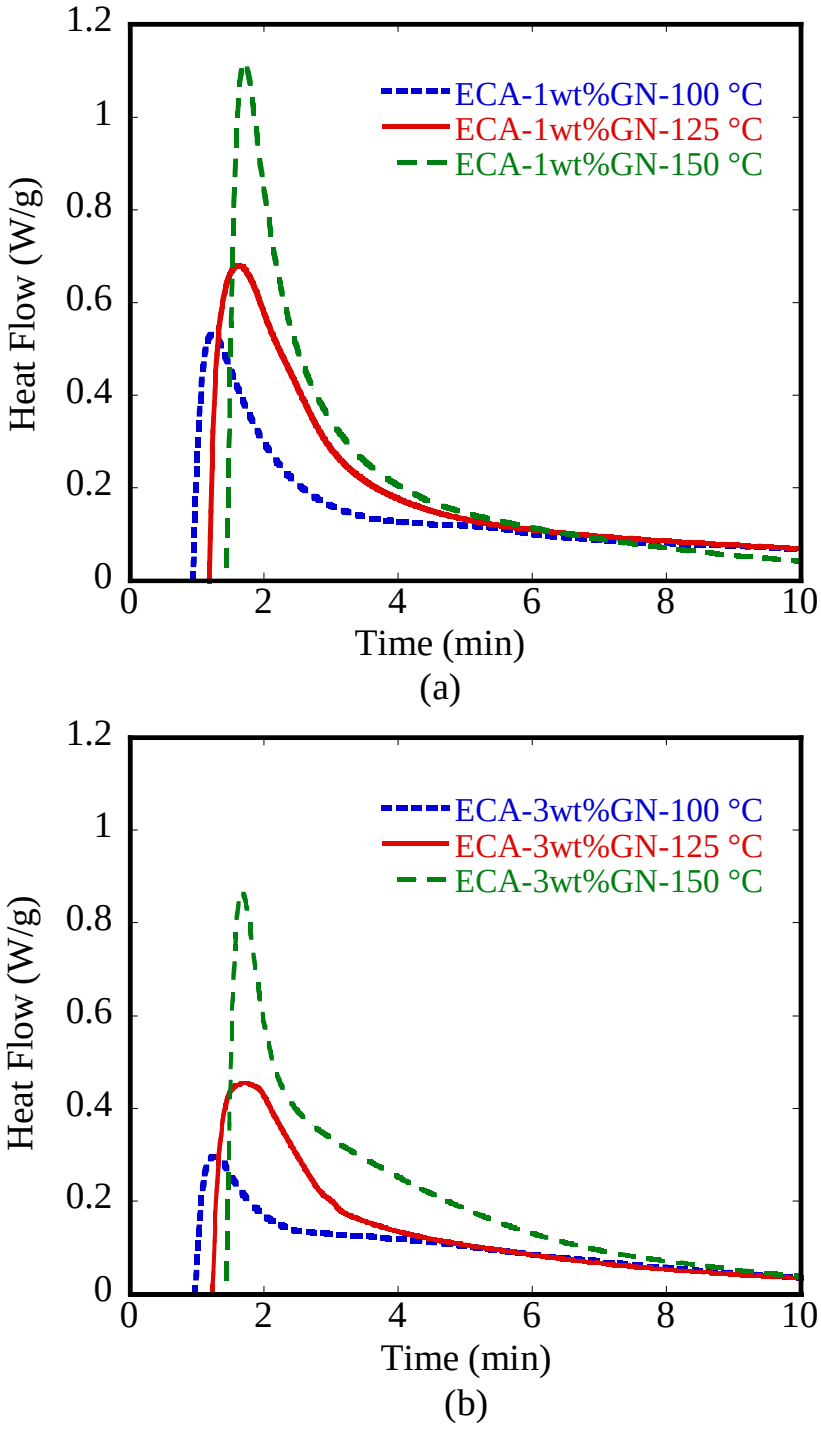

Fig 5.2: Isothermal DSC results of, (a) NCOMP-GN (1wt %) and, (b) NCOMP-GN (3wt %) materials

The dynamic-DSC curves of ECA, NCOMP-1wt%GN and NCOMP-3wt%GN samples are shown in Fig. 5.3. It is clear that the majority of curing happens between 100 °C and 150°C which is in a good agreement with isothermal-DSC results. The specific cure reaction enthalpy (ΔH_t) was calculated from integrating the area under the exothermal peaks in Fig. 5.3 according to ASTM E2160-04. Also, the glass transition temperature (T_g) of the ECA and nanocomposite samples was determined from dynamic-DSC curves, using the methodology described by ASTM E1356 – 08. The results are presented in Table 5.3 which shows cure reaction enthalpy (ΔH_t) is decreased after graphene addition and this is due to the intervention of the nanopowders in the cross-linking process between the polymer chains. As per table 5.3, the glass transition temperature (T_g) which also depends on the degree of cross-linking shifts to lower temperatures with increasing the filler amount.

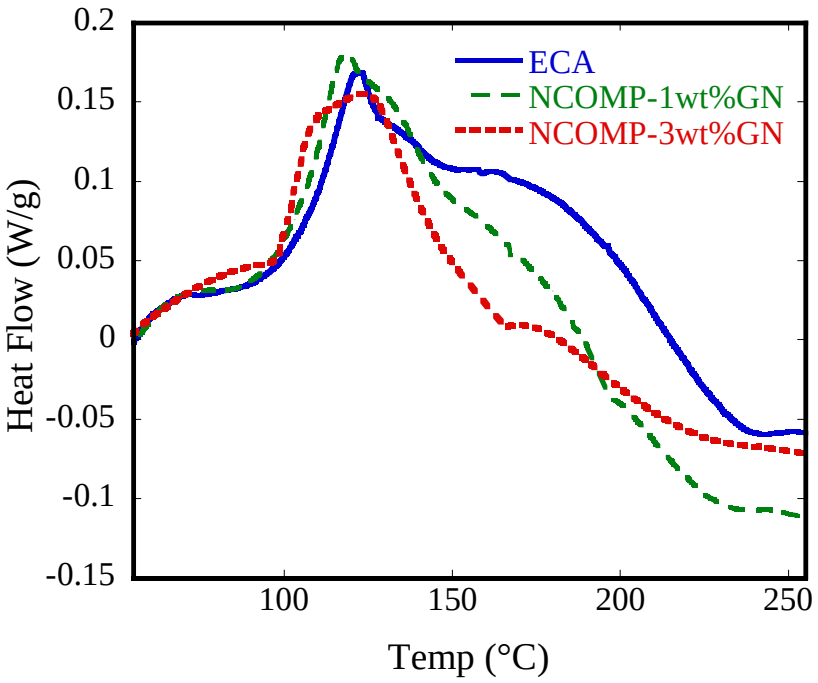

Fig 5.3: Dynamic DSC curves of the ECA, NCOMP-GN (1wt %) and NCOMP-GN (3wt %) materials.

Table 5.3: Thermal analysis data for the prepared NCOMP-GN nanocomposites.

Parameter	ECA	NCOMP-1wt%GN	NCOMP-3WT% GN
ΔHt (J/g)	45.87	38.48	37.39
Tg *°C)	220	206	193
1st step weight loss %	11.4	12.92	13.45
2ed step weight loss %	5.16	6.609	7.16
Total weight Loss %	23.42	26.64	29.37

The results of thermogravimetric analysis for the ECA and NCOMP-1wt%GN and NCOMP-3wt%GN samples are shown in Fig. 5.4(a) and (b). For temperatures up to 300°C all the samples are thermally stable without notable mass loss. The temperatures for onset of decomposition of all three samples in Fig. 5.4(a) and (b) are higher than the corresponding T_g values in Table 5.3, implying the samples have excellent thermal resistance. The TGA thermographs also show that the samples show a characteristic two-step decomposition behaviour; the first step starts at around 300°C, and it is due to the oxidative thermal decomposition of the network organic segments and the second one, initiating at around 450°C, can be attributed to the oxidative decomposition of the formed char[119]. Referring back to table 5.3, nanocomposites exhibit slightly more weight loss in both first and second steps which could be due to the excess graphene oxidation in both samples; however, it can be stated that the effect of graphene on the thermal decomposition of the nanocomposite is almost negligible and the developed materials have suitable thermal properties for use as a printable electrode. The total weight loss in all three samples suggests that all the organic components burn out at 650 °C and only metallic phase remains after that.

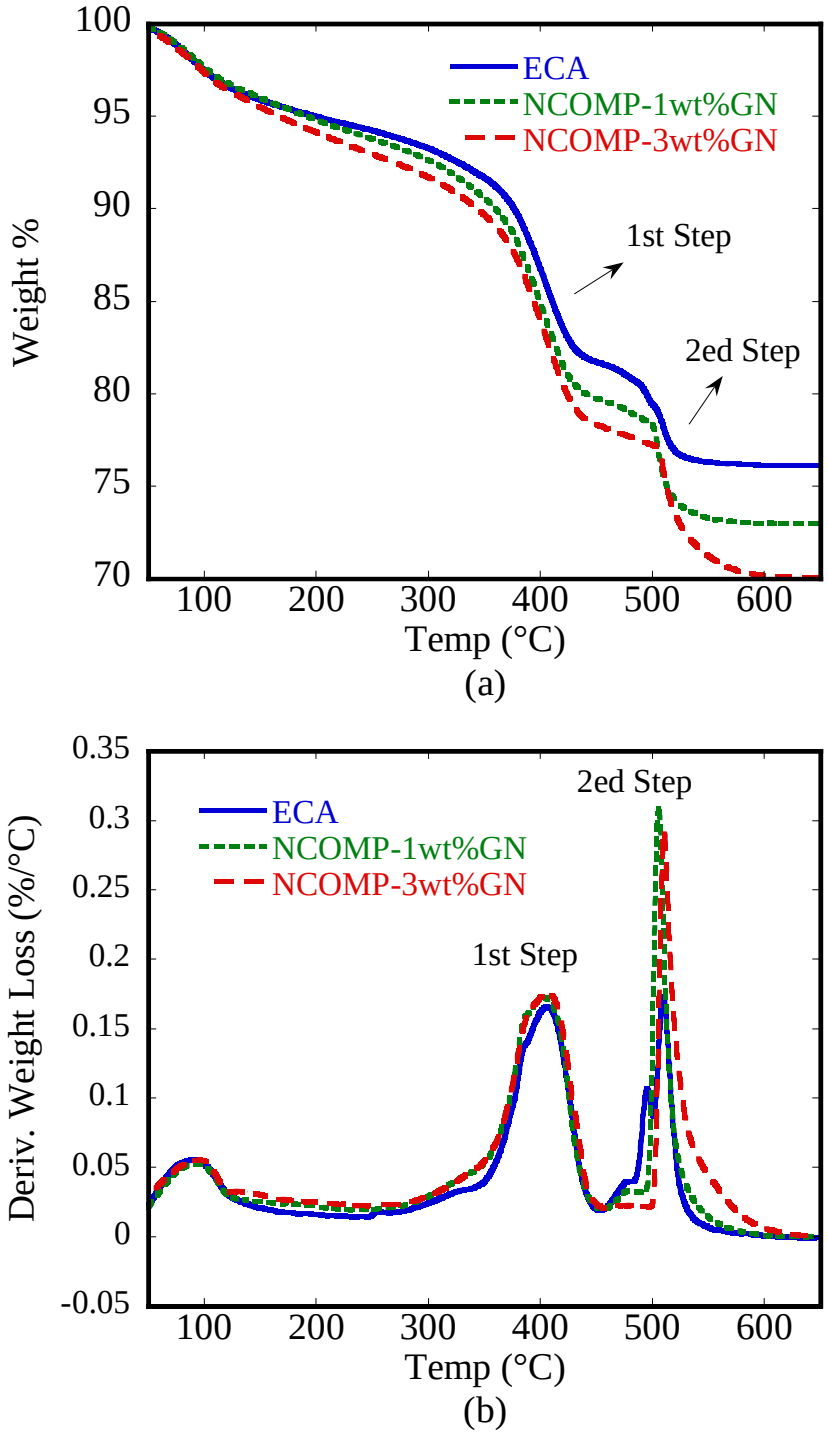

Fig 5.4: (a) TGA and, (b) DTG thermographs of ECA, NCOMP-GN (1wt %) and NCOMP-GN (3wt %) materials

5.5.2 Electrical Properties of the Printed Films

The resistivity (ρ) measurement results of the printed NCOMP-1wt%GN and NCOMP-3wt%GN are presented in Fig. 5.5. In Fig. 5.5, the ρ values of both NCOMP-1wt%GN and NCOMP-3wt%GN samples decrease with increasing curing temperatures confirming that the enhanced shrinkage by curing increases the contact area and consequently decreases the tunneling and constriction resistances. Also, comparing the incorporated amounts of graphene in the nanocomposites, increased amount of graphene tends to increase the resistivity, which can be due to the higher number of contact points between the fillers leading to a larger constriction resistance.

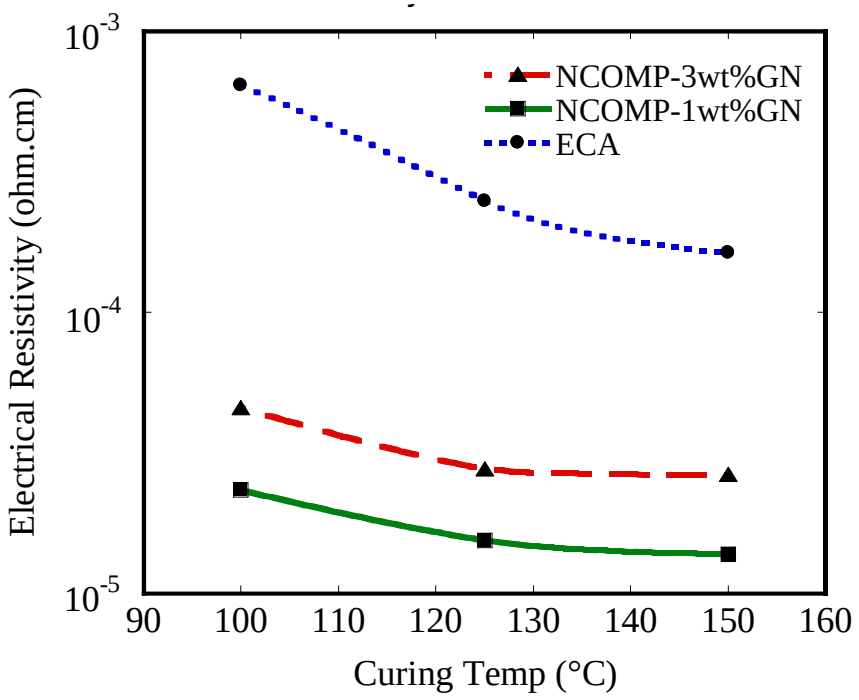

Fig 5.5: Effect of curing temperature on the resistivity of the ECA, NCOMP-1wt%GN and NCOMP-3wt%GN printed film

Electrical resistivity of all the materials studied in chapter 3 and 4 are compared to each other in Fig. 5.6 which shows the resistivity of NCOMP-GN samples are much lower than that of ECA samples.

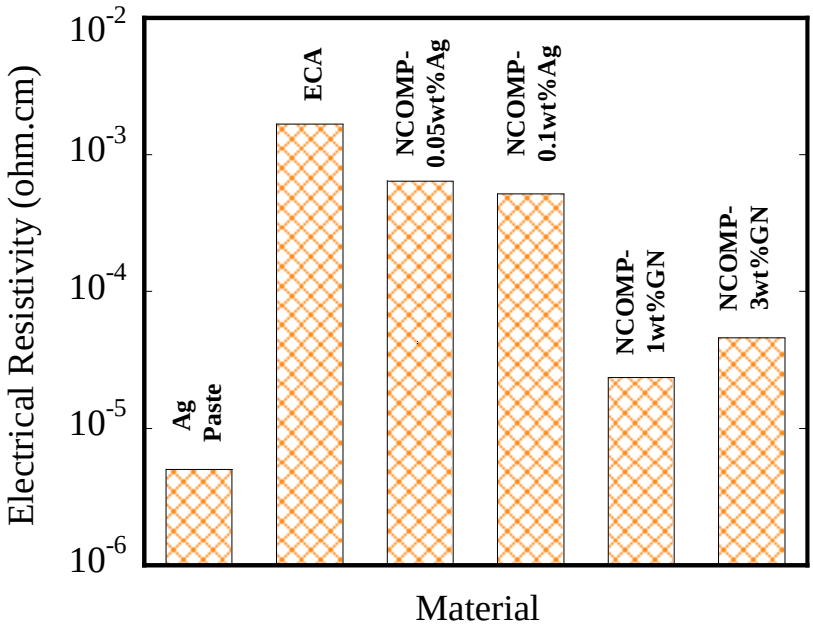

Fig 5.6: A comparison of the resistivity measured on different materials

Also, as it can be seen in Fig. 5.6, adding 0.05 wt% and 0.1 wt% of Ag NWs to the ECA improves the conductivity of the nanocomposite by 60% and 70% respectively; however, addition of graphene nanopowders increases the conductivity of the ECA by two orders of magnitude which can be due to the very low density and high specific area of graphene sheets. It should also be mentioned that increasing the Ag NW concentrations to more than 0.1 wt% may not be time and cost efficient due to the additional centrifuge step required to remove the solvent from the Ag NW solution which could also increase the chance of agglomeration as well as the cost of the material. Thus, nanocomposites containing 1wt% of the graphene nanopowders (NCOMP-1wt%GN) cured for 10 min at 150 °C represents the most suitable choice as printable nanocomposite on the Si substrate.

5.5.3 Residual Stress Analysis

Fig. 5.7 shows the values of residual stress induced in 4-inch Si substrates printed with ECA, NCOMP-1wt%GN and NCOMP-0.1wt%Ag; for a better comparison analysis, the residual stress results of Ag-paste, ECA, NCOMP-0.1wt%Ag are also added to the graphs. The substrate

thickness was in a comparable range (300-345μm) for all cases in Fig. 5.7. It is clear that the residual stress values of ECA and nanocomposite samples are close to each other while the Ag-paste sample has much higher residual stress. The maximum and average values of the measured residual stresses are given in Table 5.4.

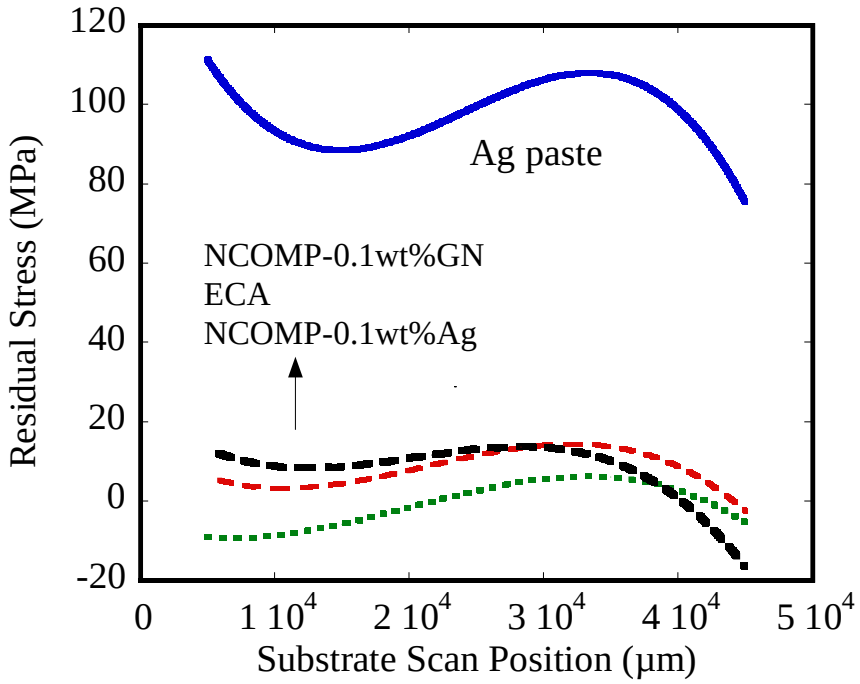

Fig 5.7: Residual stress induced by printed Ag paste, ECA, NCOMP-0.1wt%Ag and NCOMP-1wt%GN films on Si wafers. (The wafer thicknesses were within comparable range, 300-350 μm).

Table 5.4: Average and maximum residual stress values.

Printing material	Max. residual stress (MPa)	Ave. residual stress (MPa)
Metal	109	97
ECA	14	8
NCOMP-0.1wt%Ag	6	9
NCOMP-1wt%GN	14	9

In order to analyze the effect of substrate thickness on the induced residual stress, measurements were carried out after printing the nanocomposites on Si substrates having different thicknesses. The results are shown in Fig. 5.8(a) and (b). The stress values for both NCOMP-1wt%GN and NCOMP-0.1wt%Ag printed substrates are within the same range and only very small dependence on wafer thickness was observed. However, for metallic-printed wafers the smaller the thickness, the induced residual stress would be significantly higher. As mentioned before, stress data on metal printed wafers of thickness below 200μm was not possible due to wafer breakage after sintering process. The result confirms that ECA and nanocomposite materials have the advantages of requiring lower curing temperatures (compared to metal pastes) but also inducing much less stress even for thin wafers.

The degree of bending of Si wafers printed with ECA, NCOMP-1wt%GN, NCOMP-0.1wt%Ag, and metallic film printed substrates are depicted in Fig. 5.9 as a function of wafer thickness. As would be expected, the bending increases with decreasing wafer thickness. But the deflection is significantly smaller in ECA and nanocomposite samples compared to the metallic printed ones. The higher amount of bending in NCOMP-1wt%GN compared to the ECA is due to optimizing the curing process and increasing the temperature to 150°C. The ECA and nanocomposite printed samples with wafer thicknesses down to 100 μm made it successfully through the curing process without any breakage. Considering the resistivity results shown in Fig. 5.6 and the wafer bending values in Fig. 5.9, both NCOMP-1wt%GN, NCOMP-0.1wt%Ag nanocomposites could be a promising alternative for printable electrodes for ultrathin substrates. Since the resistivity of the NCOMP-1wt%GN is very close to that of conventional metallic pastes and its induced residual stress is much lower, this nanocomposite can be an attractive alternative for screen printed electrodes thin-wafer devices. A near-future application could be Si solar cells where the industry is moving towards thin wafer technologies.

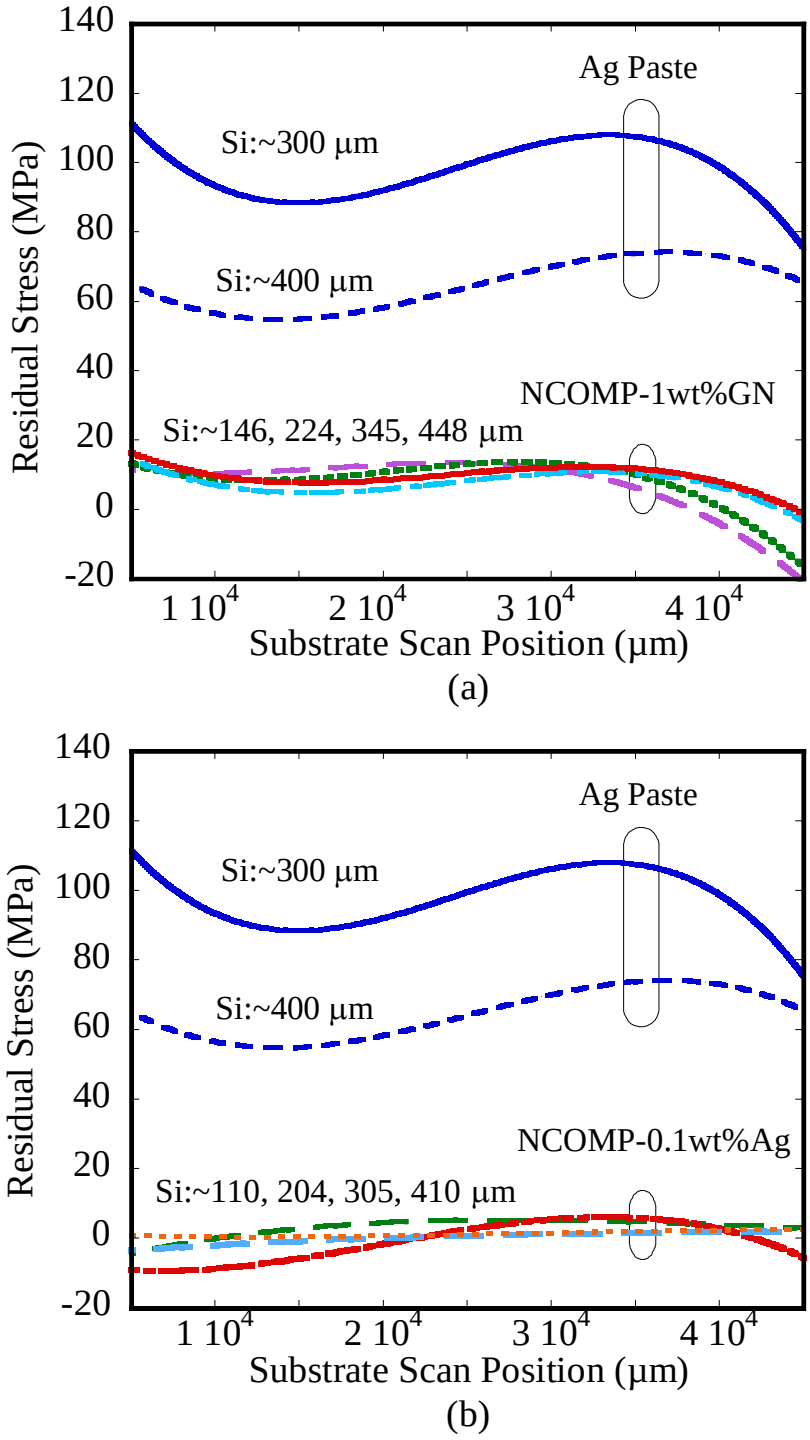

Fig 5.8: Residual stress induced by printed, (a) NCOMP-1wt%GN and, (b) NCOMP-0.1wt%Ag nanocomposite films on Si wafers with different thicknesses

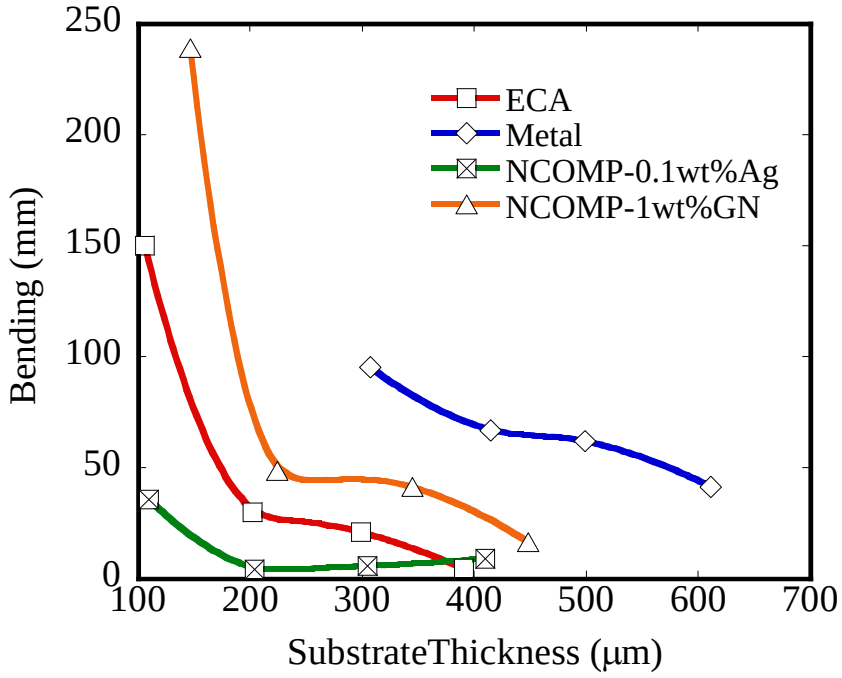

Fig 5.9: Bending in ECA, nanocomposites and metallic paste printed wafers with different thicknesses (points are connected to guide the eye).

SEM results of ECA paste andNCOMP-GN-1wt% samples are shown in Fig. 5.10(a) to (d). According to Fig. 5.10, silver flakes have the main role in developing the conductive network in all three samples. It can also be seen that the graphene sheets mostly fill the gap between the silver flakes (Fig.5.10(b) and (c)), but the conductive network is much weaker in ECA-Ag-0.1wt% sample as it was seen in Fig. 4.7 due to their specific shape and lower volume concentration of the silver nanowires.

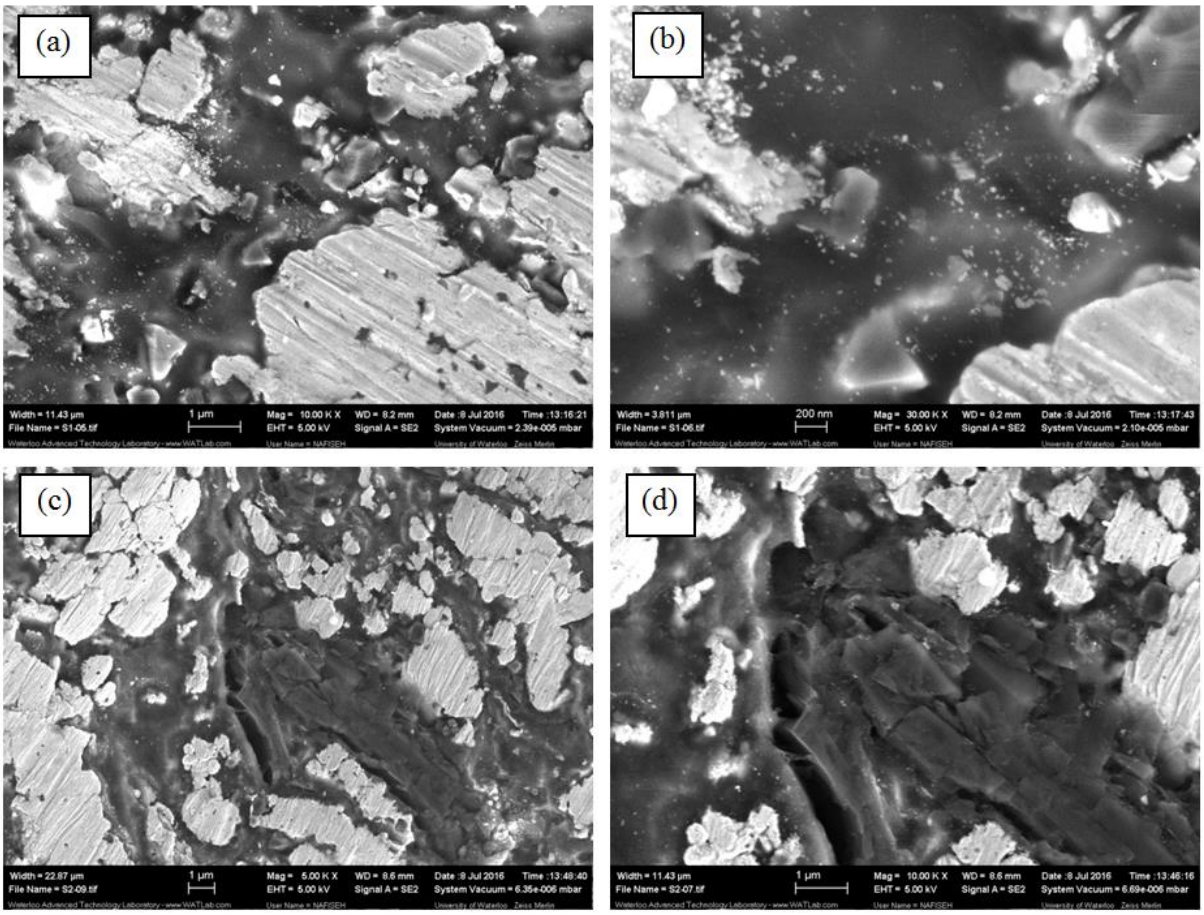

Fig 5.10: SEM analysis of (a) ECA , (b) ECA at higher resolution, (c) NCOMP-GN-1wt%, (d) NCOMP-GN-1wt% at higher resolution

Main theories for conduction mechanism, "percolation threshold theory" and "tunneling effect or field emission", are considered to analyze the effect of graphene nanopowders on conductivity behaviour of the NCOMP-GN nanocomposite. As it is mentioned before, percolation threshold theory is based on forming a conductive network in the matrix due to the contacts between flakes at a critical amount of the filler content. As it is shown in Fig. 5.10(c) and (d), because of the large surface area of graphene sheet, there is either a high chance of direct physical contact between graphene sheets and silver flakes or they are most likely at the tunneling distance from the silver flakes (less than a few nm). Therefore, both conduction mechanisms are utilized to explain the conductivity improvement of the nanocomposite after adding the graphene nanopowders. However, as shown in Fig.4.7, the role of silver nanowires in physical connecting of silver flakes

in NCOMP-0.1wt%Ag is negligible and only the tunneling effect of the scattered silver nanowires located between the silver flakes could be responsible for conductivity improvement of the material.

5.6 Conclusions

New nanocomposites were synthesized by adding different amounts of graphene nanopowders to epoxy-based ECA paste to improve the electrical conductivity. For the NCOMP-GN samples a proper mixing procedure was optimized and then curing profile was developed by conducting a comprehensive set of dynamic and isothermal DSC measurements and studying the curing kinetics of the nanocomposites. A high degree of curing was obtained when samples are sintered at 150°C for 10 min. The thermal stability of the ECA and NCOMP-GN nanocomposites were investigated using thermogravimetric analysis and results showed that the temperatures for onset of decomposition in nanocomposites are higher than their corresponding T_g showing their excellent thermal resistance. Compared to the printed ECA and NCOMP-Ag nanocomposites, the NCOMP-GN nanocomposites resulted in the highest boost in conductivity, over 2 orders of magnitude of ECA, bringing it comparable to metal pastes. Residual stress analysis also revealed that the amount of residual stress induced in the substrate is much lower in ECA and nanocomposite printed wafers in comparison with metallic printed ones. The dependence of residual stress and wafer bending on wafer thickness is much lower in ECA and nanocomposite printed wafers compared to metallic printing. Considering the aspects of low curing temperature, good thermal resistance, high conductivity, and low residual stress, the NCOMP-1wt%GN nanocomposite could be a promising alternative in screen printing metallization of thin substrates such as in photovoltaics.

Chapter 6

Effective Work Function Extraction of Conductive Nanocomposite Being Used as an Electrode in Electronic Devices

6.1 Introduction

As it was mentioned in the previous chapters, printable conductive adhesives play an important role in manufacturability of industrial scale electronic devices due to their lower processing cost and large area compatibility compared to vacuum deposited metallic films. Low temperature processability, short processing times, resistance to thermo-mechanical fatigue, compatibility with fine pitch printing, and environmental friendliness are among the other advantages that epoxy based conductive adhesives. Most investigations on such materials have so far focused on the mechanical and electrical properties in the bulk; however, there is yet a lot to be learnt about how these materials behave electronically at interfaces.

Work function is among the most important parameters that helps to characterize the interface. Since work function is inherently defined to be a property of a single material, in the case of epoxy based nanocomposites as shown in Fig. 6.1, multiple materials such as graphene nanopowders, polymer and silver are presented at the interface with the substrate in the device which will affect the electrical behaviour of the interface. Inevitably, a new definition for the work function need to be derived.

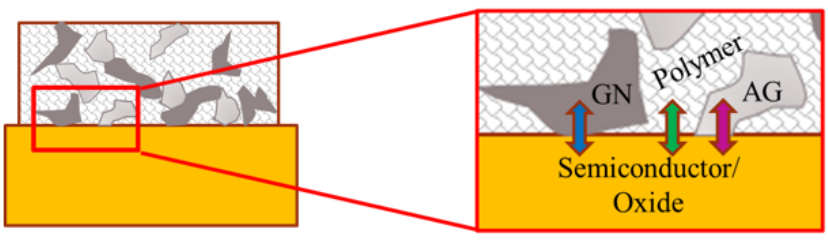

Fig 6.1: Heterogynous interface in the electronic devices using nanocomposites as electrodes

A definition of Effective Work Function (EWF) was first introduced by J. L. Freeoufet al. [121] for the work function of metallic contacts at the interface of multi-phase semiconductors. According to Freeoufet's model, the effective work function would be dominated by the micro-clusters presented at the interface which are the result of either oxygen contamination or metal semiconductor reactions. In the case of conductive nanocomposite being used as the electrode in electronic devices, the multi-phase nanocomposite will be in contact with semiconductors or oxide layers and therefore, it is predicted that work function of the nanocomposite gets affected by the electrode's heterogeneous nature as well as the potential chemical reactions at the interface. Thus, effective work function (EWF) values need to be derived depending on the interface characteristics and device structure. Multiphase nature of the conductive nanocomposite limits the methods with which EWF can be reliably measured; therefore, care needs to be given in choosing the right measurement method. For instance, the Capacitance-Voltage (CV) method that uses CV measurements with multiple oxide thicknesses [118-120] can't be used in this case because the theoretical model for a MOS capacitor with parallel electrodes does not accurately represent a device with such a heterogeneous electrode. In this investigation, we chose three techniques to measure the EWF for the graphene decorated nanocomposite which are going to be reviewed in the following sessions.

6.2 Effective Work Function (EWF) Extraction Methods

6.2.1 IV Technique

First method, to which we will refer as the IV technique in this research, relies on the onset of Fowler-Nordheim tunneling in a conductor-insulator-conductor (CIC) arrangement. The original theoretical work supporting the IV technique was introduced by Stratton [126] and Simmons[127], but more recently, Zafar et al. proposed it as a practical method for the measurement of work function [125-127]. In short, this technique involves measuring the IV characteristics in a CIC device at two different temperatures while the electrode of interest is biased as anode. From the two measurements, two important parameters are then calculated as below:

$$\Delta J_T = \frac{J(T_1) - J(T_2)}{J(T_2)} \qquad eq.6.1$$

$$\Delta \mathrm{J_V} = \frac{\mathrm{d(lnJ)}}{\mathrm{d(V)}} \qquad eq.6.2$$

Where $J(T_1)$ and $J(T_2)$ are current densities measured at temperatures T_1 and T_2while $T_1 > T_2$.
As per the theoretical studies on tunneling, if the dominant current conduction mechanism is tunneling, the maximum of ΔJ_T and ΔJ_V occurs at the same applied voltage and this voltage is equal to the barrier height at the anode. This technique can also be applied to a conductor-insulator-semiconductor arrangement if the polarity of the applied voltage is so chosen to drive the semiconductor into accumulation. Since silicon dioxide can be grown with exceptionally high breakdown voltage at ultra-low thicknesses[131], n-type silicon is an ideal substrate to be used with this technique. The IV technique for extraction of work function has only been applied on metallic films in the literature; however, in this study, this technique was used for the first time on a Nanocomposite-oxide-Semiconductor (NCOS) structure.

6.2.2 Ultraviolet Photoemission Spectroscopy (UPS) Technique

The second method is the Ultraviolet Photoemission Spectroscopy (UPS) which is a more recognized technique for work function extraction at the interface with vacuum [124]. UPS Spectroscopy is based on the phenomenon of photoemission in which a light source which could be gas discharge lamp, synchrotron radiation source or an X-ray tube, impinges on a sample. The light impingement would excite electrons which will be characterized by an analyzer with respect to their kinetic /binding energy [125]. A typical UPS spectrum is shown in Fig. 6.2.

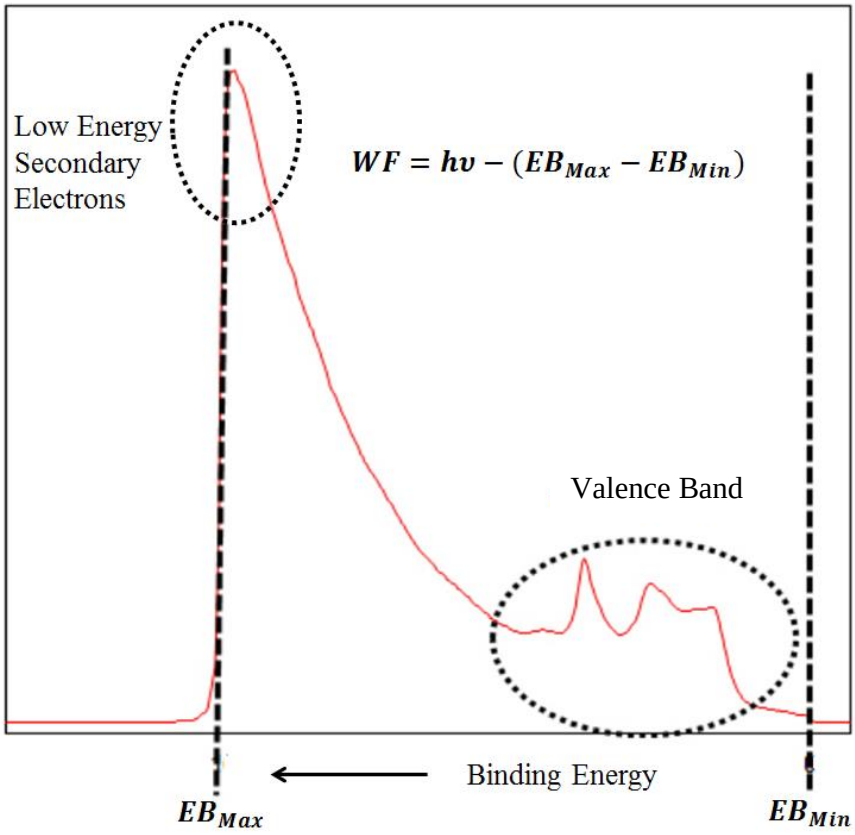

Fig 6.2: A typical UPS spectrum

As it is shown in Fig. 6.2, work function (WF) is calculated as:

$$WF = h\upsilon - (EB_{Max} - EB_{Min}) \qquad eq.6.3$$

Where $h\upsilon$ is the photon energy that bombards the sample, EB_{Max} is the maximum measured binding energy (secondary electron cut-off), and EB_{Min} is the minimum measured binding energy [132].

6.2.3 TLM Method

The last method measures the work function with the aid of specific contact resistance (ρ_c) of the printed nanocomposite-Gate on a substrates. ρ_c is measured experimentally using the Transmission line model (TLM) technique [133] with the structure shown in Fig. 6.3. W is the width of p-type or n-type layer and Z is the width of contacts. R_{ti} is the total resistance between contact i and i+1 which is equal to

$$R_{ti} = \frac{R_{sh} d_i}{W} + 2R_c \qquad eq.6.4$$

R_{sh} is the sheet resistance of the n-layer, d_i is the distance between contacts and R_c is the contact resistance between the contact and the n-layer. The specific contact resistivity ρ_c is calculated using eq. 6.5 as [134]:

$$\rho_c = R_c L_T W \qquad eq.6.5$$

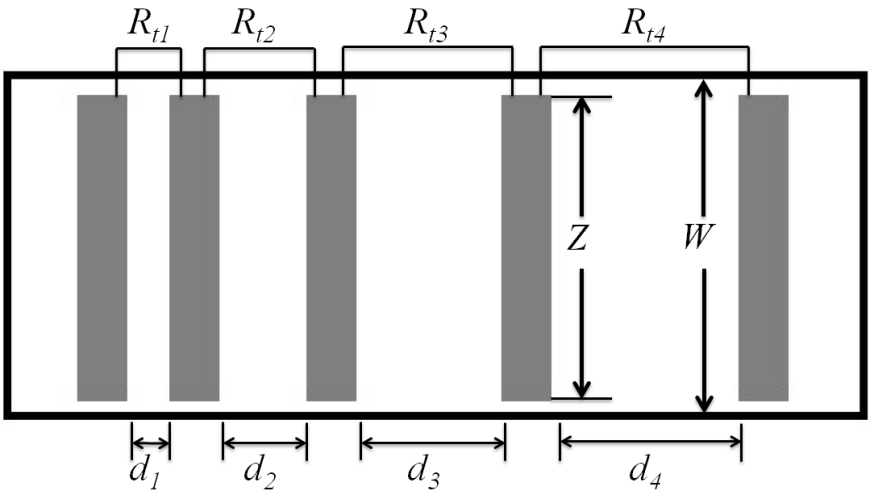

Fig 6.3: TLM test structure

By utilizing the theoretical equation for specific contact resistivity in the field emission regime [134] and finding the contact barrier height, Work function of the nanocomposite gate is calculated.

6.3 Experimental Procedures

As explained in chapter 4, the nanocomposite was prepared starting from a standard conductive silver epoxy (ECA) from Transene used as the matrix, and Graphene nano-flakes (Graphene Supermarket) with an average flake thickness of 12nm were used as the additives to form composites with 1 wt.% graphene content (NCOMP-1wt%GN). The mixture was mechanically stirred for 20 min in a Vortex mixer followed by 1 h of sonication in a Cole-Parmer ultrasonic bath to disperse the graphene flakes uniformly in the paste. Fig 6.4 shows Graphene nano-flakes

interconnecting silver particles in a cross-sectional SEM image of a printed NCOMP-1wt%GN film. This has been reported previously in chapter 4 to improve the bulk conductivity of the film.

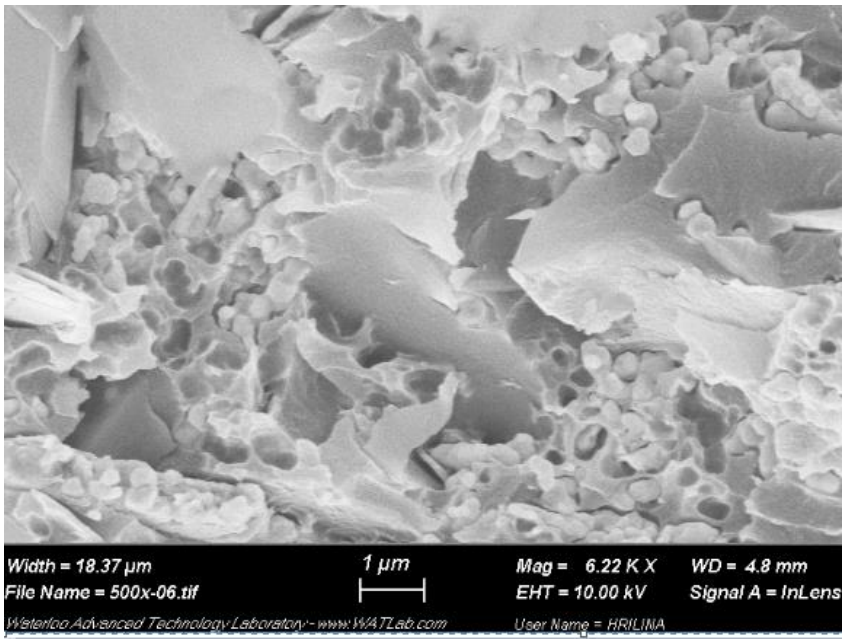

Fig 6.4: Cross sectional Scanning electron micrograph of NCOMP-1wt%GN nanocomposite showing graphene flakes and silver particles

6.3.1 IV Technique

To make the nanocomposite devices to be used with the IV technique, 4" phosphorous doped n-type silicon wafers with (100) surface orientation and 4 Ω.cm resistivity were first passed through standard cleaning steps. A dilute hydrofluoric acid dip was done immediately prior to loading the wafers into a Rapid Thermal Processor (RTP600S, Modular Process Technology Corp.) for thermal silicon dioxide growth. Oxide was then grown with a 2 min ramp to 850°C in N_2 ambient, then a 65 sec hold at 850°C in pure O_2. This was then followed by a 60 sec ramp to 1000°C in N_2 and a 60 sec hold at 1000C in N_2 ambient. Sample was then cooled down to room temperature in N_2 ambient in 2 minutes. The oxidation profile is shown in Fig. 6.5. Oxide thickness was determined using ellipsometer to be 32.5 A.

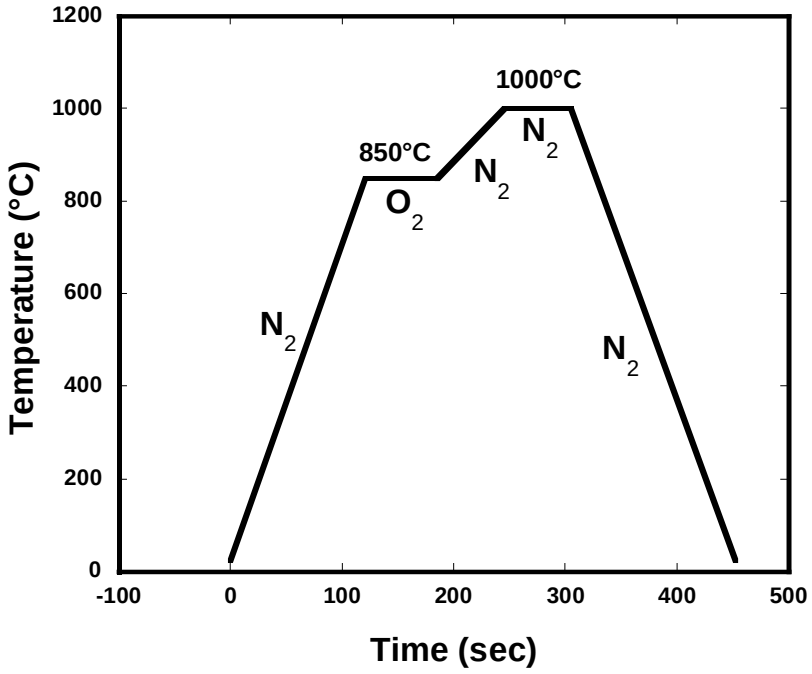

Fig 6.5: RTP oxidation profile

The oxide was then removed from the back side of the wafers in 2% hydrofluoric acid solution using a PTFE holder that seals one side of the wafer using o-rings. A 1µm thick aluminum was then deposited on the back side using an e-beam evaporator (Intlvac, NCII-6EB-T) to form the cathode. The back contact was then sintered in forming gas at 450°C for 30min. The NCOMP-1wt%GN nanocomposite pads, with various sizes down to 50µm^2, were then screen printed on the prepared substrates using a Dek 248 screen printer. The nanocomposite was then cured at 150°C for 10 minutes in an oven in air ambient. The fabricated MOS device is shown in Fig. 6.6 schematically.

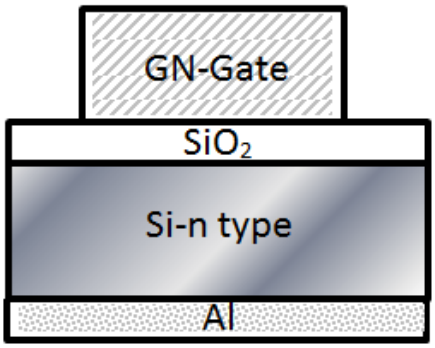

Fig 6.6: A schematic illustration of the fabricated MOS device

Current-voltage measurements of these devices were then performed on an aluminum chuck with embedded heaters at 25ºC and 105ºC using an Agilent 4155 semiconductor parameter analyzer. Voltage on the nanocomposite was swept from 0V to +5V, making it the anode, while the substrate was held at 0V. Each current-voltage sweep was applied on a fresh NCOS device for parameter extraction as the oxide would breakdown by end of each sweep.

6.3.2 UPS Technique

To prepare the samples for UPS spectroscopy, 5mm×5mm pads of nanocomposite with a thickness of around 1mm were doctor bladed through a stencil on a pre-cleaned non-stick PTFE sheet with smooth surface. The substrate was then cured at 150ºC for 10 minutes in an oven in air ambient. Cured nanocomposite was then detached from the substrate. The UPS measurements were done on the surface of the nanocomposite that was in contact with the substrate using a Thermo Fisher Scientific ESCALAB 250Xi that uses a He I (21.22 eV) discharge lamp. The spectrometer was calibrated using XPS with monochromatic Al Kα (hν = 1486.7 eV) and then samples were sputter cleaned with 2 keV Ar ion beam for 40 s in the analysis chamber. To separate the sample and the secondary edge of the analyzer, a bias of −10 V was applied.

6.3.3 TLM Method

To calculate the specific contact resistance (ρ_c) in the TLM method, contacts were printed on a highly doped p- layer ($5x10^{19}$ cm^{-3}) with the sheet resistivity of 50 Ω/□. High temperature quartz furnaces with thin circular disks of Boron sources were used for P-type diffusion. Current-voltage

measurements of the devices were then performed on an aluminum chuck using an Agilent 4155 semiconductor parameter analyzer. Nanocomposite was then doctor bladed through a stencil to fabricate the TLM test structure. Z and W (Fig. 6.3) are considered to be equal to each other (15 mm) to minimize the induced lateral currents.

ρ_c obtained from TLM method is used to calculate the effective work function of the graphene decorated nanocomposite contacts. ρ_c is defined as [135]:

$$\rho_c = \left[\frac{A^* \pi q T}{k \sin(\pi c k T)} exp\left(\frac{-\varphi_{bs}}{E_{00}}\right) - \frac{A^* q}{c k^2} exp\left(\frac{-\varphi_b}{E_{00}} - c u_f\right)\right]^{-1} \quad eq.6.6$$

where

$$E_{00} = \frac{\hbar}{2}\sqrt{\frac{N}{\epsilon_s m^*}} \quad eq.6.7$$

And

$$c = \frac{1}{2E_{00}} ln\left(\frac{4\varphi_{bs}}{u_f}\right) \quad eq.6.8$$

Where $A^*$is Effective Richardson constant, φ_{bs} is the barrier height, k is the Boltzmann constant, $\hbar$ is the Plank's constant, u_f is the distance between Fermi level and band edge, N is doping concentration, ϵ_s is semiconductor permittivity and m^* is the electron effective mass. As it can be seen in Eqs 6.6-6-8, ρ_c is strongly related to the doping concentration, effective mass and barrier height while effective mass is a function of doping type and doping concentration itself.

6.4 Results and Discussion

6.4.1 IV Technique

Fig.6.7 shows the IV characteristics of nanocomposite devices with 200μm^2 pad size at 25°C and 105°C. IV curves depict a similar trend with two voltages at which sudden increase in the current is evident. These voltages would manifest themselves as maxima in the ΔJ_V and ΔJ_T plots as shown in Fig. 6.8(a) and (b).

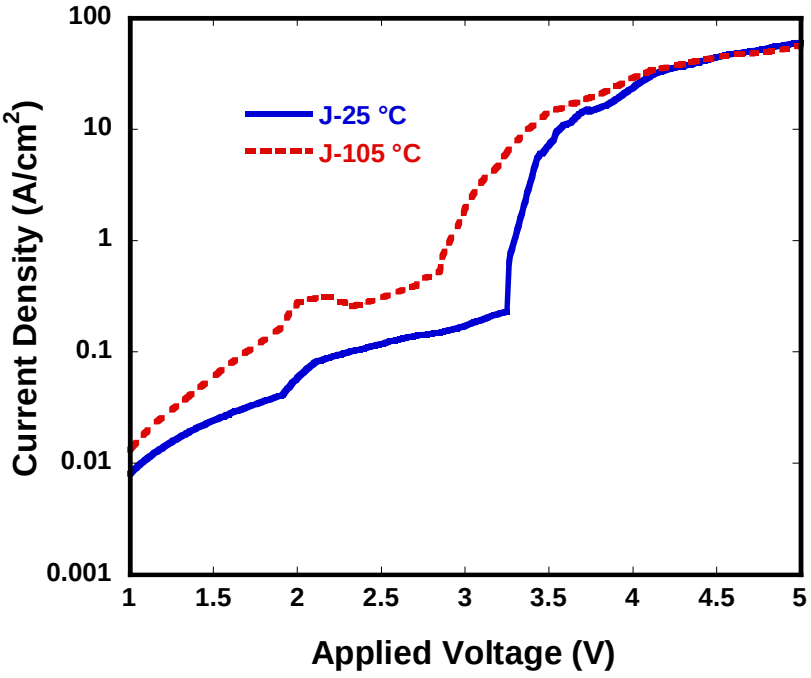

Fig 6.7: IV characteristics of NCOS devices at room temperature and 105°C

The first peak that appears around 1.8-2V is likely due to a defect level within the oxide band gap. Note that this peak is also visible on the control structures that were made with pure evaporated silver as the anode and can't be attributed to the multi-material nature of the nanocomposite. However, the second peak that happens at voltages slightly above 3V is an indicative of the onset of FN tunneling and is the voltage from which the barrier height at the nanocomposite (anode) side of the device can be deduced.

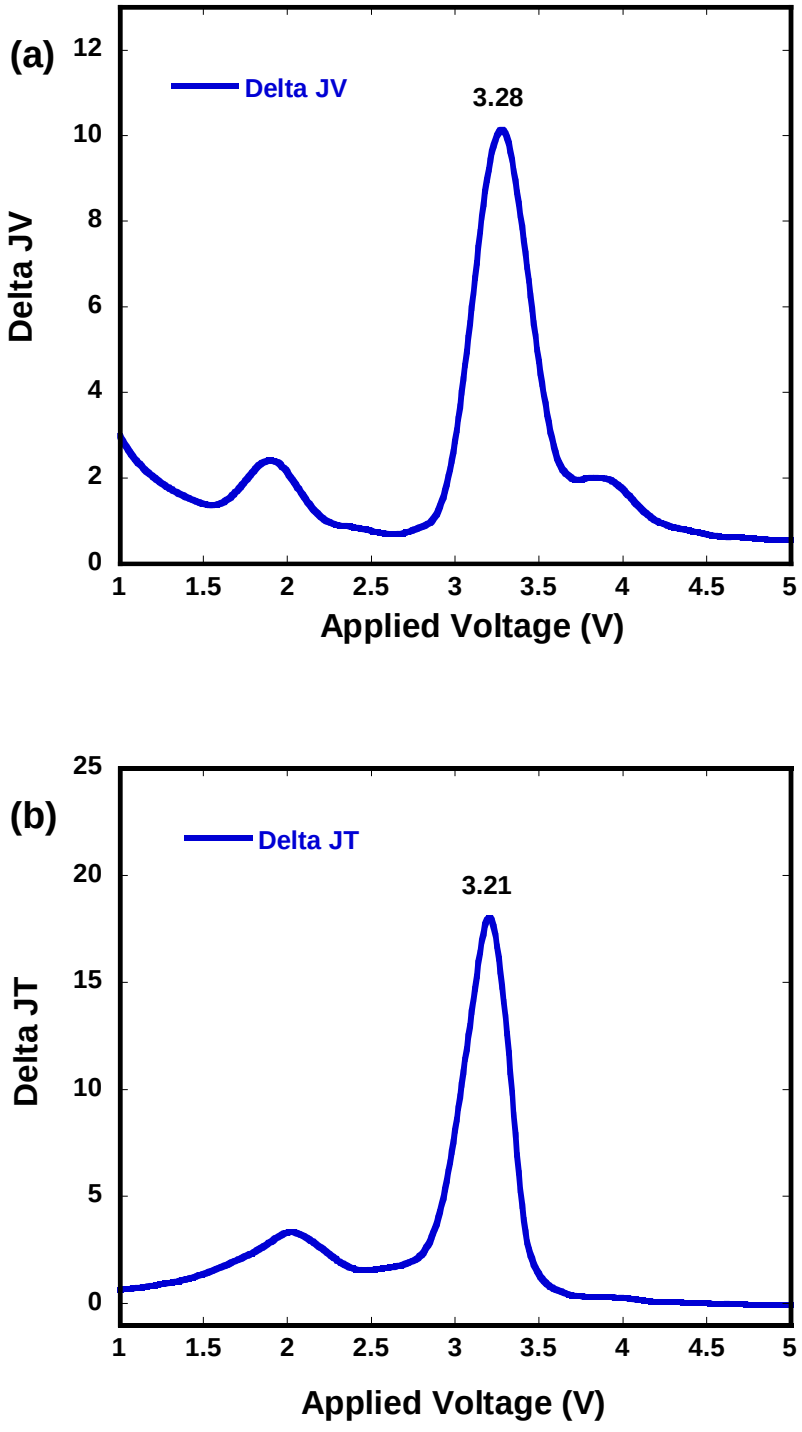

Fig 6.8: ΔJ_V and ΔJ_T vs. applied voltage for the nanocomposite devices derived from the IV measurements.

Both curves exhibit peaks in the range of 3.21 - 3.28 V which is an acceptable level of agreement and verifies that tunneling is in fact the dominant current conduction mechanism. A value of 3.25±0.03eV, averaged over many measurements, was taken as the barrier height at the anode (φ_b). The effective work function of the graphene doped nanocomposite (W_g) can then be calculated to be 4.15±0.06 eV which is the sum of the measured barrier height and the electron affinity of the oxide (X_{ox}=0.9 eV) as shown in the band diagram of the NCOS device in Fig. 6.9.

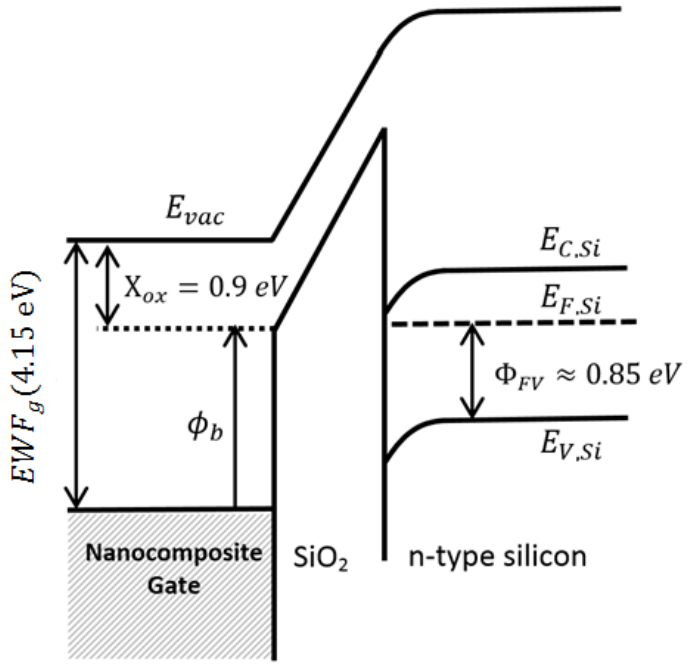

Fig 6.9: Band diagram of the NCOS device at the onset of FN tunneling.

6.4.2 UPS Technique

Fig. 6.10 (a) shows the UPS spectroscopy measurements of the graphene doped nanocomposites (NCOMP-1wt%GN). EB_{Max} and EB_{Min} are extracted by drawing tangents on base line as well as the rising and falling cut offs on the UPS spectrum as it is shown in Fig. 6.10 (b) and (c). A value of 4.52eV was extracted for the effective work function (EWF) of the nanocomposite.

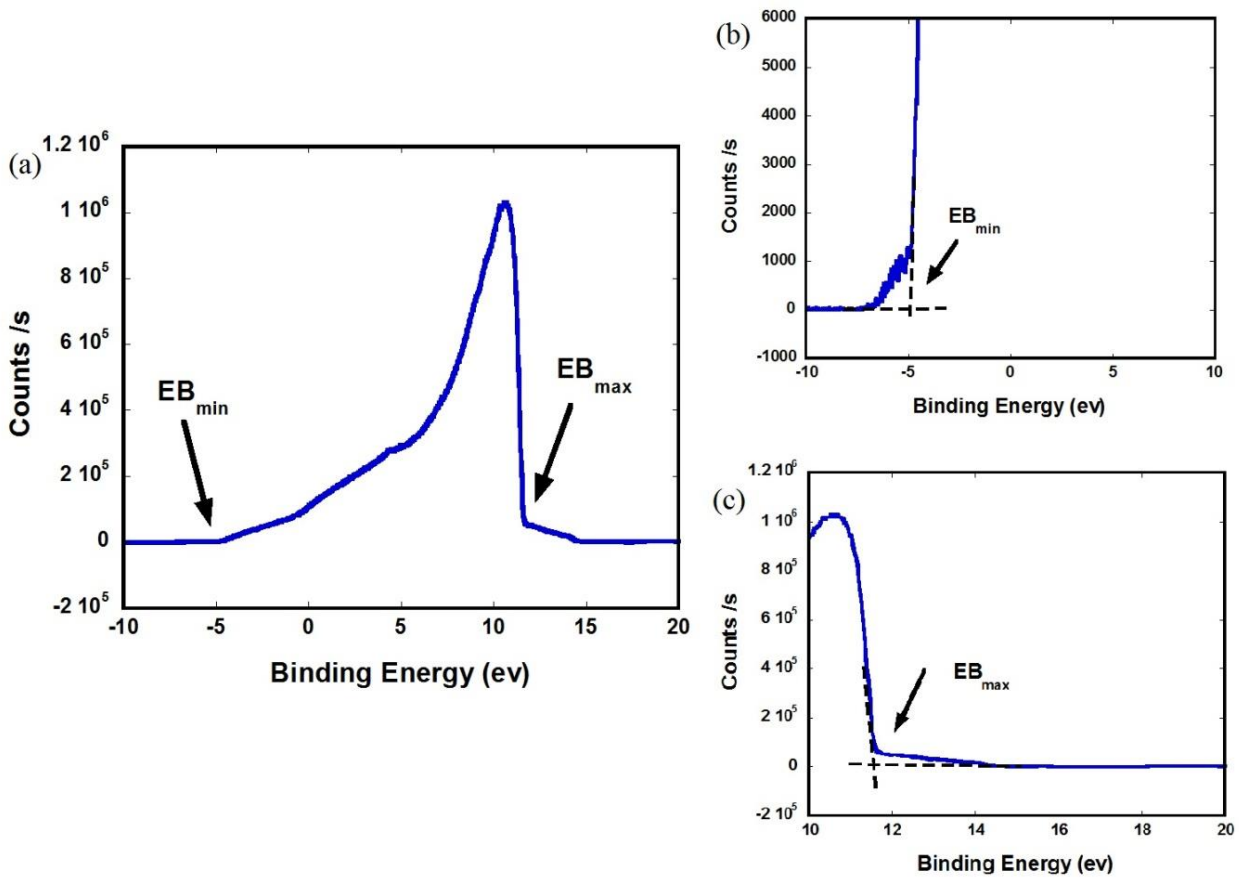

Fig 6.10: Typical UPS spectroscopy measurement results of the graphene doped nanocomposite

The XPS spectroscopy was also performed on the UPS samples to characterize the components at the interface with vacuum and as it is shown in Fig 6.11, the amount of carbon at the interface is much larger than Silver and even though a portion of the signal could represent the graphene nanoparticles, the majority of it is showing the role of epoxy organic materials in the measured bulk work function of the nanocomposite. This also confirms the importance of using an effective work function definition due to the multi-phase nature of the nanocomposite.

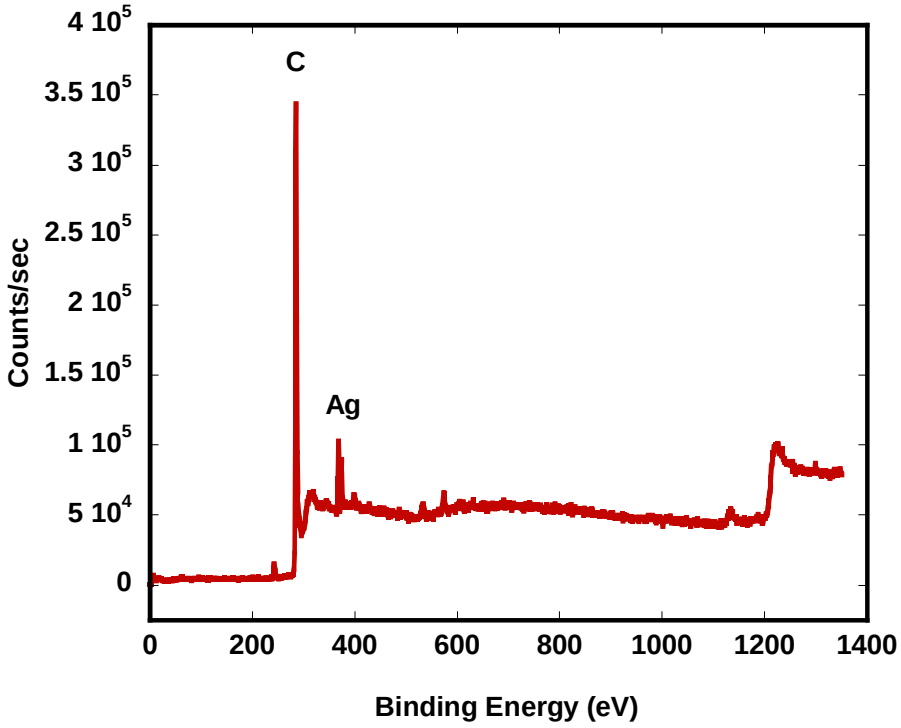

Fig 6.11: XPS spectroscopy of the NCOMP-1wt%GN

6.4.3 TLM Method

Fig. 6.12 shows the measured R_{ti} vs d_i based on the TLM test structure and a best linear fit is generated to calculate contact resistance (R_c) and current transfer length (L_T). Using Eq. 6.4 and the generated equations for the linear fit shown in Fig. 6.12, R_c would be equal to 0.13 Ω. The generated R_{ti} line is extrapolated (shown in Fig. 6.12 by dashed lines) to determine the point of intersection at the d_i axis which is equal to $2L_T$ and the value of L_T is measured to be 6.15×10^{-3} mm. Using Eq. 6.5 and the above determined values for R_c and L_T, the specific contact resistance (ρ_c) is measured to be 1.19×10^{-4} Ω.cm^2.

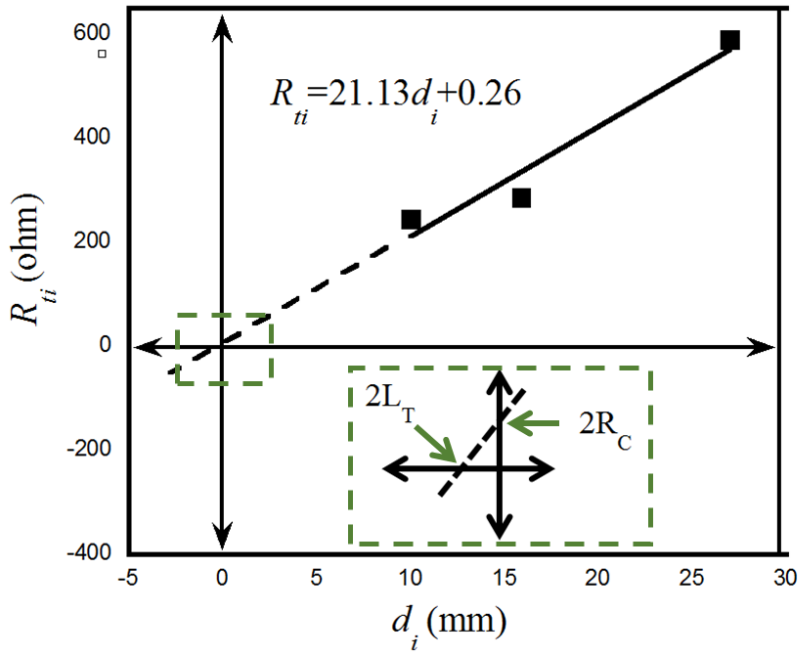

Fig 6.12: Plot of total resistance (R_{ti}) as a function of contact spacing (d_i) for NCOMP-1wt%GN

Using the above measured ρ_c and numerically calculated specific contact resistivity using equations 6.6-6-8 for different barrier heights (φ_{bs}) based on doping concentration for highly doped p-type <100> Si [135], φ_{bs} is obtained to be 0.8 eV. Considering the schematic band diagram of the Nanocomposite-gate/semiconductor under equilibrium shown in Fig. 6.13:

$$EWF_g = E_{g,Si} + X_{Si} - \varphi_{bs} \qquad eq.6.9$$

Where X_{Si} is the electron affinity of the silicon and $E_{g,Si}$ is the band gap of the silicon (Table 6.1). By substituting the $X_{Si}$and $E_{g,Si}$ from Table 6.1 and the obtained value for φ_{bs} in Eq.6.9, EWF_g is obtained to be 4.39 eV.

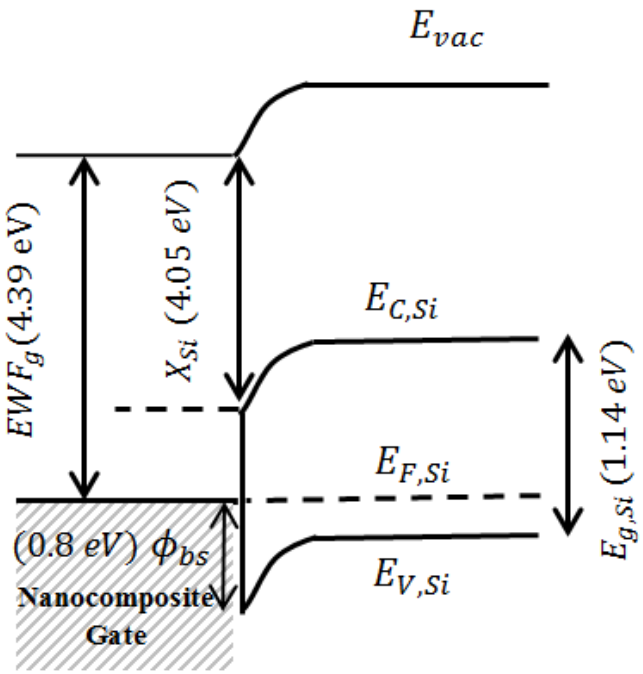

Fig 6.13: Schematic band diagram of the Nanocomposite gate/semiconductor

There is a small but notable difference between the extracted EWF values from all three methods which can be partly attributed to the nature of each measurement technique and the interface structure. IV and TLM measurements are giving lower EWF values which could be due to the fact that both techniques are relying on tunneling current transfer between the nanocomposite electrode and Silicon oxide/ highly doped silicon while UPS method depends on electron excitement by photo emission. Therefore, measurement results from IV and TLM techniques are extremely dominated by the most conductive element (silver with WF of ~4.26 eV) which makes intimate contact with the oxide and P+ layer but UPS method is insensitive to the conductivity level of the material and all the components of the nanocomposite contribute to the measured effective work function value. It should be noted the other main element in the graphene decorated nanocomposite is carbon with WF of ~5 eV which is potentially the reason in the slight increase in the extracted EWF from the UPS method.

Table 6.1: General parameter Values

Parameter	Value
$E_{g,Si}$ (eV)	1.14
X_{Si}(eV)	4.05

It should also be noted that dependence of reported values of work function on the measurement method is not uncommon [144]and a contributing factor could be the sensitivity of each of these measurement methods to different forms of impurities and potential chemical reactions at the interface. The observed difference suggests that an effective range of 4.15eV to 4.52 eV for the work function is to be expected that can possibly be dependent on the type of structure this nanocomposite is used in. It also confirms the necessity of using effective work function definition for the electrodes with multiphase nature.

6.5 Conclusion

In summary, Effective Work Function (EWF) was introduced for the multi-phase nanocomposite electrodes being used as electrodes in electronic devices. Based on the theoretical studies on tunneling phenomenon and the potential barrier height measurement analysis on MOS devices, IV method was illustrated and used for the first time to measure the EWF of the multi-phase nanocomposite electrodes. The results were verified using two other techniques: UPS spectroscopy and TLM. The results from all measurements are in reasonable agreement however a small difference between the UPS technique and the other two exists. The difference is attributed to the heterogeneous nature of the nanocomposite and the difference in the sensitivity of each measurement method to the surface structure. These observations indicate that a possibly device-dependent effective value for the work function is worthy to be expected.

Chapter 7

Solar Cell Fabrication with New Developed Conductive Nanocomposite as Rear Contacts

7.1 Introduction

Electronic conductive adhesives (ECA) have been reported to be used in solar industry as an interconnection between the cells in modules with back contact cells as well as the modules made by shingling technology [135-139] [138]; however, ECAs have never been used as the main front or back contact in the solar cell itself to the best of author's knowledge. This chapter will present the solar cell fabrication process step by step and the newly developed and characterized graphene decorated nanocomposite will be used as the back contact. As it was previously reviewed, utilizing the newly developed nanocomposite in the cell contacts will reduce the processing temperature and consequently the amount of induced residual stress and cell bowing. This will enable the industry to use ultra-thin silicon substrates which normally cannot tolerate high stress levels and might cause failure. Therefore, Low temperature firing of the newly developed nanocomposite could be very beneficial for developing ultra-thin solar cells to lower cost and increase yield performances.

7.2 Materials Used

To fabricate the Solar cell, n-type silicon substrate (100) with phosphorus dopant concentration of 5×10^{15} cm^{-3} were used. Ag was used for front contact while Al and graphene-decorated nanocomposite (NCOMP-1wt%GN) were used for the back contact. For the doping step, BN-975 and PH-950 from Saint-Gobain ceramic materials are considered as the P-type and N-type sources, respectively.

7.3 Fabrication Process

7.3.1 Primary cleaning and preparation

A diamond scriber was used to engrave sample numbers on the wafers. Wafers are first RCA1 cleaned for 13 minutes in 5:1:1 combination of DI water: Ammonium hydroxide: hydrogen peroxide at 75-85° C. RCA2 cleaning was performed immediately after RCA1 and wafers were cleaned for 13 minutes in 10:2:1 combination of DI water: hydrogen peroxide: Hydrochloric acid at 75-85° C. Wafers were washed thoroughly with DI water and they were dipped in 2% Hydrofluoric acid for 60 seconds to remove the native oxide. After the HF dip, wafers were washed with DI water and dried with nitrogen.

7.3.2 Developing the n^+ layer at the back

After the substrates were HF dipped and dried, they were loaded in the diffusion furnace to diffuse phosphorus at the back to create an n^+ layer. The purpose of having the n^+ layer is to keep the minority careers away from getting recombined at the rear contact. A phosphorus dopant material on an inert silicon carbide substrate was used as N-type diffusion solid dopant. Furnace was first ramped up from 400° C to 950° C for 40 mins and then phosphorus was diffused at 950°C for 45 minutes at 3 lit/min N2 flow. After the doping is finished, the furnace is ramped down back to standby temperature (400° C). Due to the design of the furnaces, the ramp down time is much longer (around 4 hours). After the diffusion, wafers were etched for 2 minutes in 10% Hydrofluoric acid to remove the thin glass layer deposited on both sides of the wafer during the diffusion process. Also, there is some dopant diffusion at the front side of the substrate even though it is not directly facing the dopant source which is removed by acid etch back. To remove the layer, front side of the samples were etched for 5 mins using 5%HF and 95% HNO3. A PTFE holder was used to cover the back side from the etchant. Samples were then dried to be ready for the next step.

7.3.3 Depositing SiONx at the back

To protect the N+ layer, substrates were loaded in the PECVD to grow SiONx film on the back side of the silicon wafers using a standard parallel plate capacitively coupled PECVD system developed by Trion Technology (Orion III). The PECVD deposition conditions are shown in Table 7.1.

Table 7.1: PECVD deposition conditions for $SiON_x$ Protection layer

Film	Pressure	power	SiH4	N2O	Temp.	Duration	Film thickness
SiONx	10 mT	10	15sccm	100sccm	400	13 min	120 nm

7.3.4 Junction formation

After wafers were unloaded from PECVD, they were RCA1 and RCA2 cleaned as described in section 7.3.1. Wafers were washed thoroughly with DI water and they were dipped in 2% Hydrofluoric acid for 15 seconds to remove the native oxide and then were loaded in the diffusion furnace. It should be noted that substrates should not be HF dipped for a long time as HF would etch the $SiON_x$ layer at the back. So, once the front side gets hydrophobic, HF dip process should be stopped. Junction was formed using dopant diffusion in high temperature quartz furnaces with solid dopant sources. Boron diffusion sources need to be activated in oxygen ambient to form a B2O3 layer on the solid sources which will act as the dopant source for P-type diffusion. For P-type diffusion, the furnace was ramped up from 400° C to 950° C for 40 mins and then boron was diffused at 950°C for 30 minutes at 3 lit/min N_2 flow. After the doping is finished, furnace is ramped down back to standby temperature (400° C). Due to the design of the furnaces, the ramp down time is much longer (around 4 hours).

After the diffusion, wafers were etched for 30 seconds in 10% Hydrofluoric acid to remove the thin glass layer deposited on front sides of the wafer during the diffusion process. Extra care needs to be taken at this step to make sure back side is still hydrophilic which means it is still protected by $SiON_x$. Afterwards, front side of the samples were etched for 35 seconds in 0.5%HF and 99.5% HNO3 to make the emitter layer slightly thinner to reduce the number of electron hole pairs created in it and decrease the chance of their recombination. Then wafers were etched for 2 minutes in 10% Hydrofluoric acid to remove the $SiON_x$ protection layer followed by 25 seconds of etching in the 0.5%HF and 99.5% HNO3 solution. Now substrates are ready for next step which is Anti-Reflection Coating (ARC) deposition.

7.3.5 Anti-Reflection Coating (ARC)

SiN is selected to be used as anti-reflection coating due to its proper surface passivation properties **[143]**. The same PECVD system mentioned in 7.3.3 was used to deposit the anti-

reflection coating. First, samples were dipped in 2% Hydrofluoric acid for 1 minute to remove the native oxide layer and then were quickly loaded to PECVD. The PECVD deposition conditions are shown in Table 7.2 and a schematic illustration of the device before photolithography is shown in Fig. 7.1.

Table 7.2: PECVD deposition conditions for ARC layer

Film	Pressure	power	SiH4	NH3	Temp.	Duration	Film thickness
SiN	10 mT	10	10 sccm	200sccm	400	9 min	80 nm

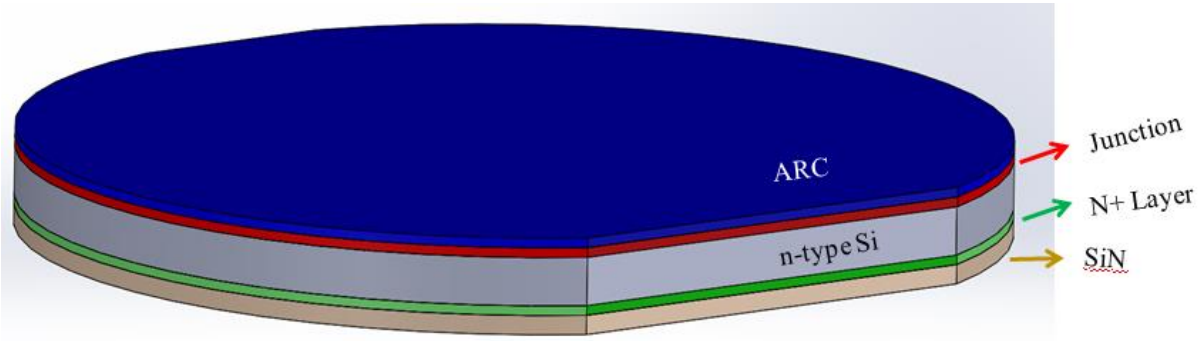

Fig 7.1: Schematic Illustration of the cell before patterning

7.3.6 Patterning the Anti-Reflection Coating (ARC)

A negative photoresist (AZ nLOF 2035) and a mask with 1cm x 1cm cells shown schematically in Fig. 7.2 were used to pattern the ARC layer. Patterning was conducted using the following conditions:

- Photoresist spin coating at 3000 RPM for 60 seconds
- 1 min of hard bake at 110°C
- UV exposure for180 seconds at 60mWcm^{-2}
- 1 min of hard bake at 110°C
- Developing in AZ-MIF Developer for round 120 seconds

Samples were etched in Buffered Hydrofluoric acid (BHF) for 70 seconds to remove the SiN after the photoresist is patterned. Then Samples were dried and loaded into electron beam evaporation system to deposit the front contact.

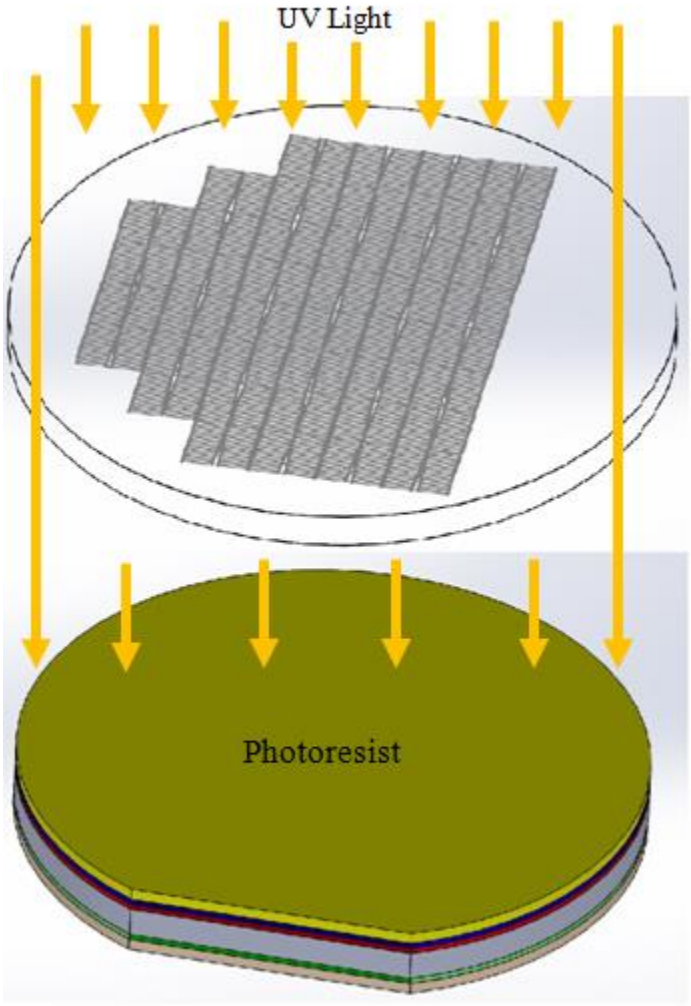

Fig 7.2: A schematic illustration of the mask used to pattern the cell with negative photoresist

7.3.7 Front Contact Deposition

As mentioned in the previous section, samples were loaded in to the electron beam evaporation chamber right after they were BHF dipped to deposit the front contact. After chamber reached to the base pressure of around 10^{-7}Torr, first 100 nm of Titanium is deposited to prevent the diffusion of Ag during the forming gas annealing and then 1µm if Ag was deposited afterwards. After the samples were unloaded from ebeam, the metal lift-off process was performed by submerging the samples in to high purity acetone for 3 hours. Evaporated Ag front contact on 10mm x 10mm cell is shown in Fig. 7.3

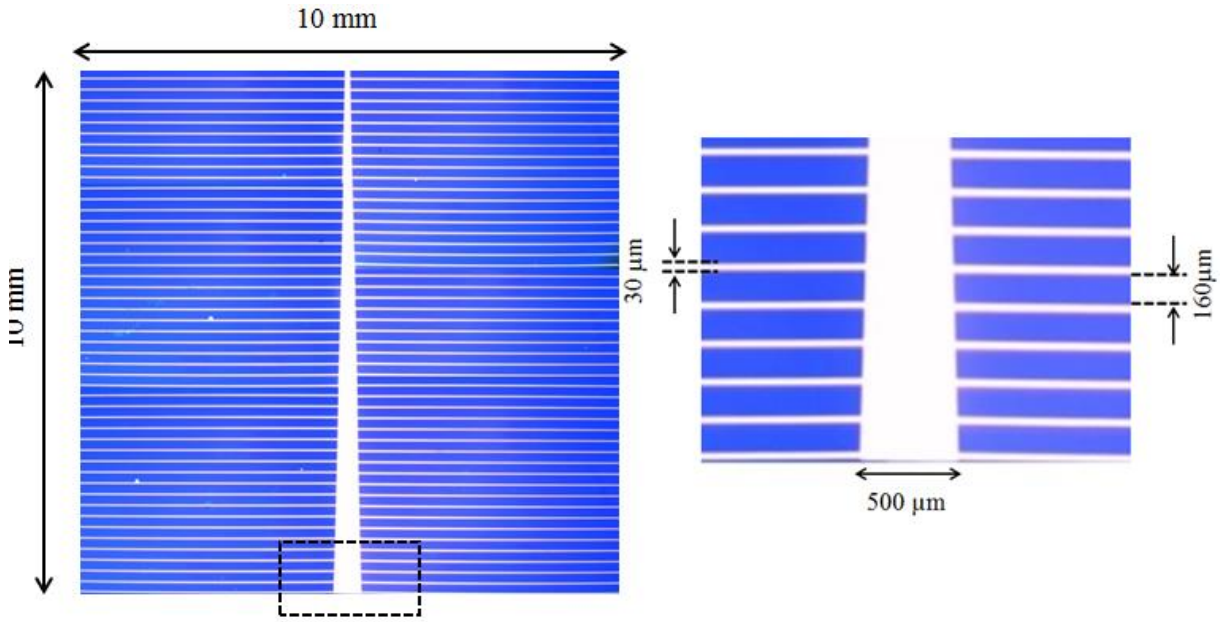

Fig 7.3: Evaporated Ag front contact

After the metal is completely lifted off, samples are annealed in forming gas (10% H2, 90% N2) at 350°C for 10 minutes at 3 lit/sec to improve the quality of electrical contact between emitter and the metal layer.

7.3.8 Back Contact Deposition

Back side of one sample was etched in 2% Hydrofluoric acid for 1 minute to remove the native oxide layer and again loaded back into the Ebeam to deposit 1µm of Al as the back contact. This reference sample is going to be used for the comparison purpose to evaluate the properties of the cell with the NCOMP-1wt%GN back contact.

A screen-printing system (AMI model MSP-485) accommodating screen frames with the maximum size of 12" ×12" and maximum print area of 8" ×8" was used to print the NCOMP-1wt%GN back contact on the samples. Printer setup was prepared first, then back side of the samples was etched in 2% Hydrofluoric acid for 1 minute and then the NCOMP-1wt%GN was screen printed on the back side. The nanocomposite printed cell was then cured at 150°C for 10 minutes in an oven in air ambient.

7.4 Characterization Methods

Following different characterization methods available in CAPDS lab are used to study the performance of fabricated solar cells.

7.4.1 Measurement of reflection spectra

This characterization technique will be used to measure the amount of the input light entering the device as well as the amount being reflected. In this technique, a monochromator is used to produce light with determined wavelengths. The reflected light is collected and directed to a sensing photo-detector. The amount of reflected light would be the ratio of the signal at sensing photo-detector to the signal at the input light monitoring detector. To perform above measurements, a PerlinElmer Lambda 1050 UV/VIS/NIR spectrometer is used.

7.4.2 Internal and External Quantum Efficiency

Measuring the Internal Quantum Efficiency (IQE) is the most reliable method of evaluating the performance of the fabricated cells, but this quantity cannot be measured directly. In fact, IQE can be calculated using the results of the reflection spectra measurement and the External Quantum Efficiency (EQE) as below:

$$IQE = \frac{EQE}{1 - Reflection} \qquad eq.7.1$$

The spectral measurement system made by PV measurements, Inc. is used to perform EQE measurement.

7.4.3 Dark and Illuminated current-voltage measurements

I-V measurements give important information about the junction quality, actual output power of solar cells and its performance under a standard illumination. Dark IV is used to extract the junction parameters such rectification ratio and ideality factors while performed under absolute darkness to eliminate the effects of carrier generation due to the light. A light-tight housing containing the sample and the probing station is used for dark IV measurement setup. An Agilent HP4155C semiconductor parametric analyzer in CAPDS lab is used to measure the dark IV behavior of the fabricated solar cells

To study the performance of the solar cells under the standard AM1.5 illumination, illuminated IV curves are going to be measured using a setup available in CAPDS which was made by PV measurements, Inc.

7.5 Results and Discussion

7.5.1 Reflection spectrum

The front side reflection spectrum for both reference cell (Ref-Cell) and cell with NCOMP-1wt%GN (NCOMP-GN-Cell) is shown in Fig. 7.4. As shown in Fig 7.4 the minimum reflection of 17.33% was observed at wavelengths of 590 nm. As per the optical rules, refractive index of the ARC layer (n_{ARC}) multiplied by its thickness (d_{ARC}) should be equal to one quarter of the incoming wavelength (λ) to minimize the light loss due to reflection. This can be shown as below:

$$d = \frac{\lambda}{4n_{ARC}} \qquad eq.7.2$$

n_{ARC} can be calculated as below:

$$n_{ARC} = \sqrt{n_{Si}n_i} \qquad eq.7.3$$

Where n_{Si} and n_i are refractive index of Si and surrounding medium. Assuming n_{Si} and n_i are equal to 3.5 and 1, n_{ARC} would be calculated as 1.87. Bu substituting the obtained n_{ARC} and the wavelength at the minimum reflection points in Eq.7.2, the required thickness of the ARC layer should be around 78 nm which is very close to the thickness of the ARC deposited using PECVD. It should be noted that reflectance of these cells is slightly large mainly due to the absence of the texturing in the front side.

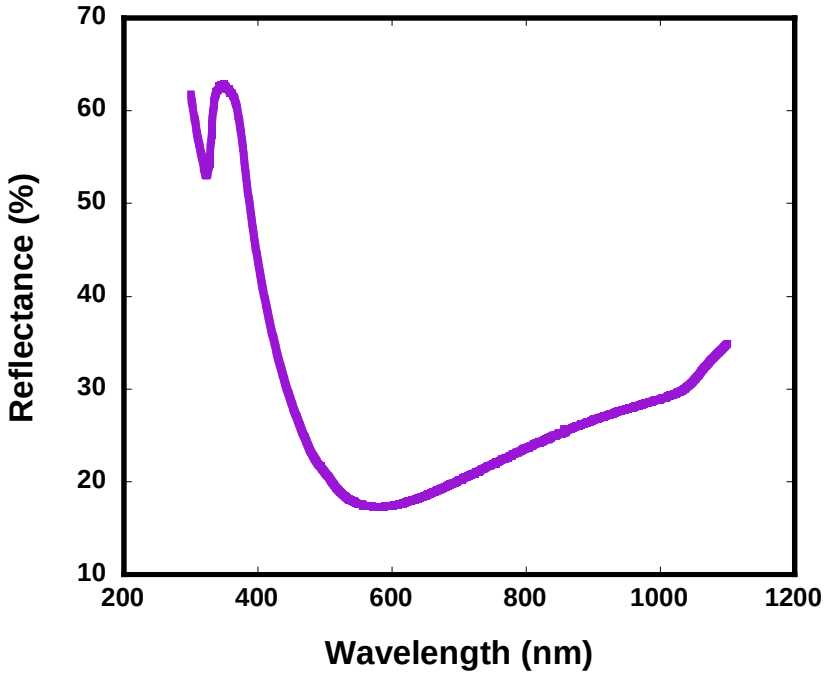

Fig 7.4: Front side reflection spectrum for both cells

7.5.2 Internal and External Quantum Efficiency

The internal and external quantum efficiency graphs of the Ref-Cell and NCOMP-GN-Cell are shown in Fig. 7.5 (a) and (b). As it is shown in Fig 7.5, both cells are showing a very good performance as their IQE is higher than 90 % for a large portion of the spectrum and it reaches to almost 100% at the middle of the spectrum. It should be noted that the thickness of the substrates used for both cells is more than 500µm which has affected the red response of the devices. Also, the lower blue response could be mainly due to not having texturing at the front side.

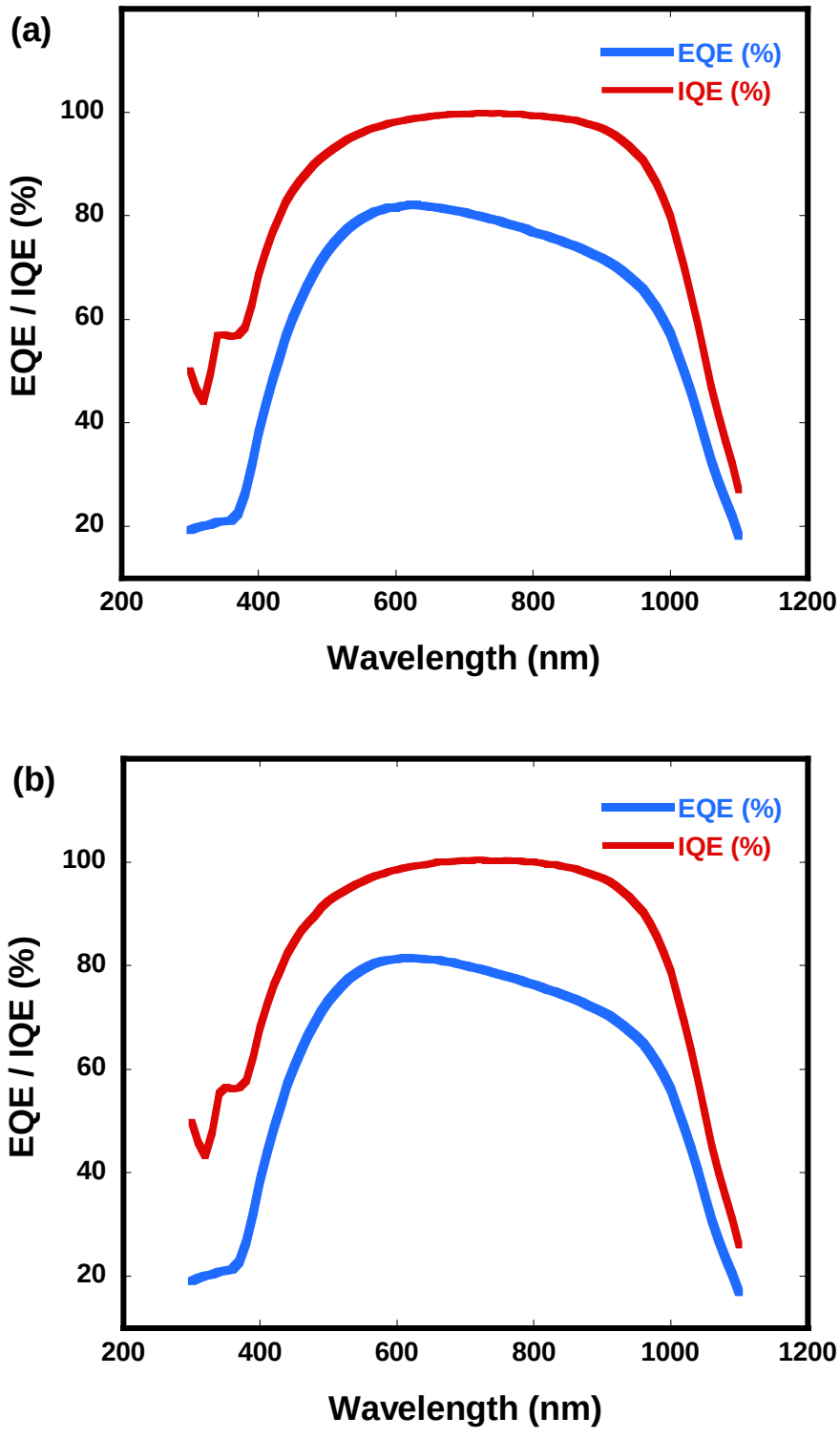

Fig 7.5: EQE and IQE of the (a) Ref-Cell and (b) NCOMP-GN-Cell

Fig. 7.6 shows a comparison between the IQE of both cells in which it can be seen that both curves are almost sitting on each other confirming the fact that using NCOMP-1wt%GN nanocomposite instead of Al for the back contact wouldn't degrade the performance of the cell.

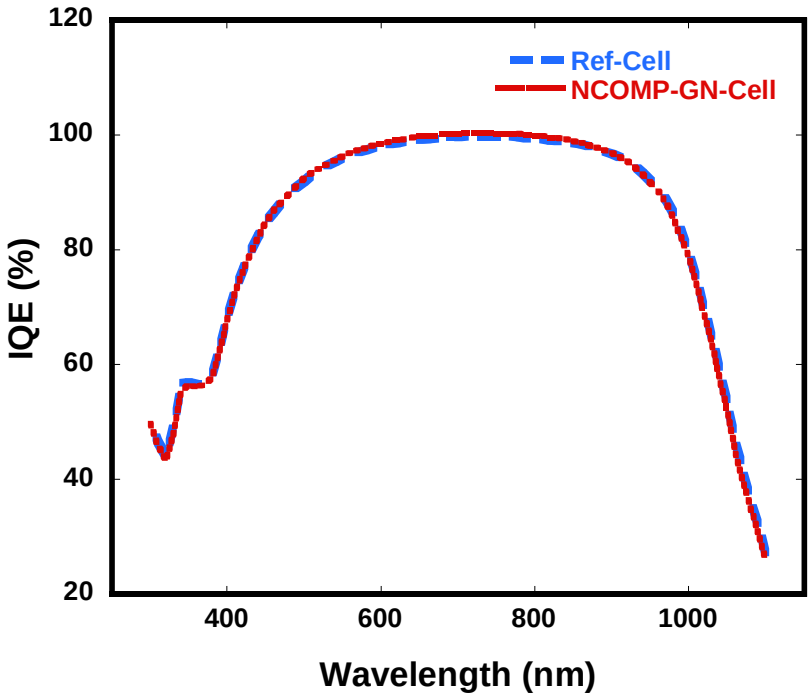

Fig 7.6: IQE comparison between Ref-Cell and NCOMP-GN-Cell

7.5.3 Dark and Illuminated Current-Voltage Results

The dark I-V characteristics of the Ref-cell and NCOMP-GN-Cell are shown in Fig 7.7. In dark IV analysis, both solar cells show typical diode behaviour. Rectification ratio is approximately $7.2\times10^{2}$and 3.4×10^{2} at ±0.74 V for Ref-cell and NCOMP-GN-Cell respectively. Reverse saturation current is obtained to be 7.8×10^{-6} A and 9.6×10^{-6} for Ref-cell and NCOMP-GN-Cell respectively. Using double-diode model, the ideality factors n_1 and n_2 of the solar cells obtained to be 2.7 and 3.12 for the Ref-Cell and 3.21 and 3.40 for the NCOMP-GN-Cell. Despite the fact that ideality factors in NCOMP-GN-Cell are slightly larger than Ref-Cell, both cells are showing large ideality factors which is mainly due to quality of the wafer substrate.

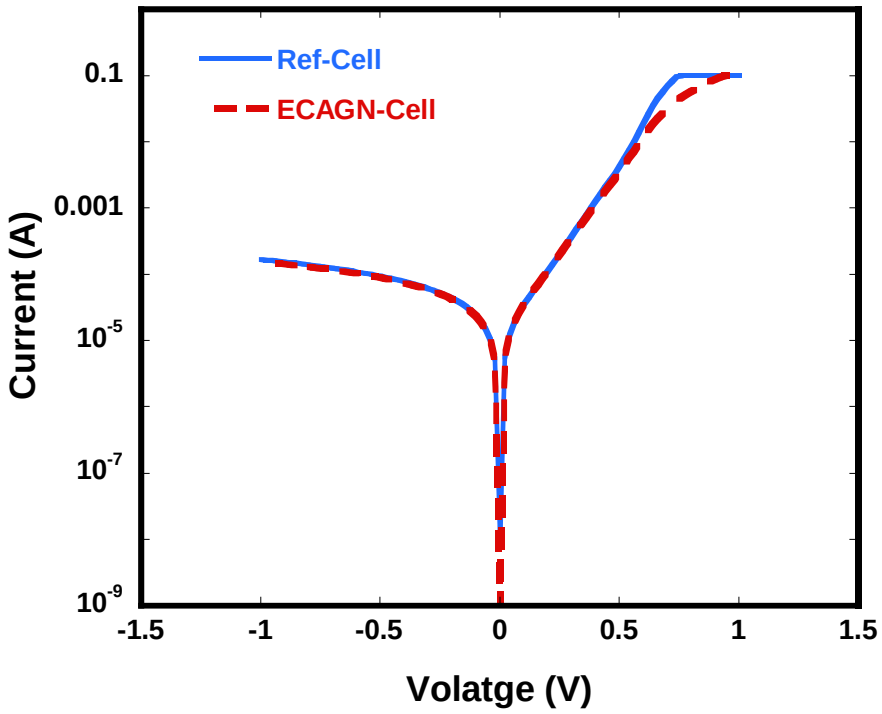

Fig 7.7: Dark IV comparison between Ref-Cell and NCOMP-GN-Cell

Fig 7.8 and 7.9 show the performance report of the illuminated I-V analysis performed under 100mW/cm^2 (AM1.5 standard spectrum) for both Ref-Cell and NCOMP-GN-Cell.

A good short circuit current density (28 mA/cm^2 and 30 mA/cm^2 for Ref-Cell and NCOMP-GN-Cell, respectively) is achieved which indicates that despite not having texturing at the front contact, the anti-reflection layer is very effective and the diffused junction is strong. The Open circuit voltage is around 590 mV for both cells which is relatively low and is again believed to be due to the quality of the starting wafers specially their low carrier life time as observed in the obtained high ideality factors. The same effect has been seen in the previous research works in this group[145].

The measured Fill Factor (FF) is reported to be around 62% and 67% for Ref-Cell and NCOMP-GN-Cell, respectively which is also a bit low compared to the conventional high efficiency solar cells. This could be due to front contact designs and the limitations regarding photolithography and evaporation processes. All that being said, the main purpose of this cell fabrication is to compare the performance of cells with metallic and nanocomposite back contacts fabricated with same

process limitation and material issues. The above cell performance results as well as almost equal obtained efficiencies (around 11%) for both cells are very close and decent comparable values which are a very satisfactory achievement for a standard technology baseline development.

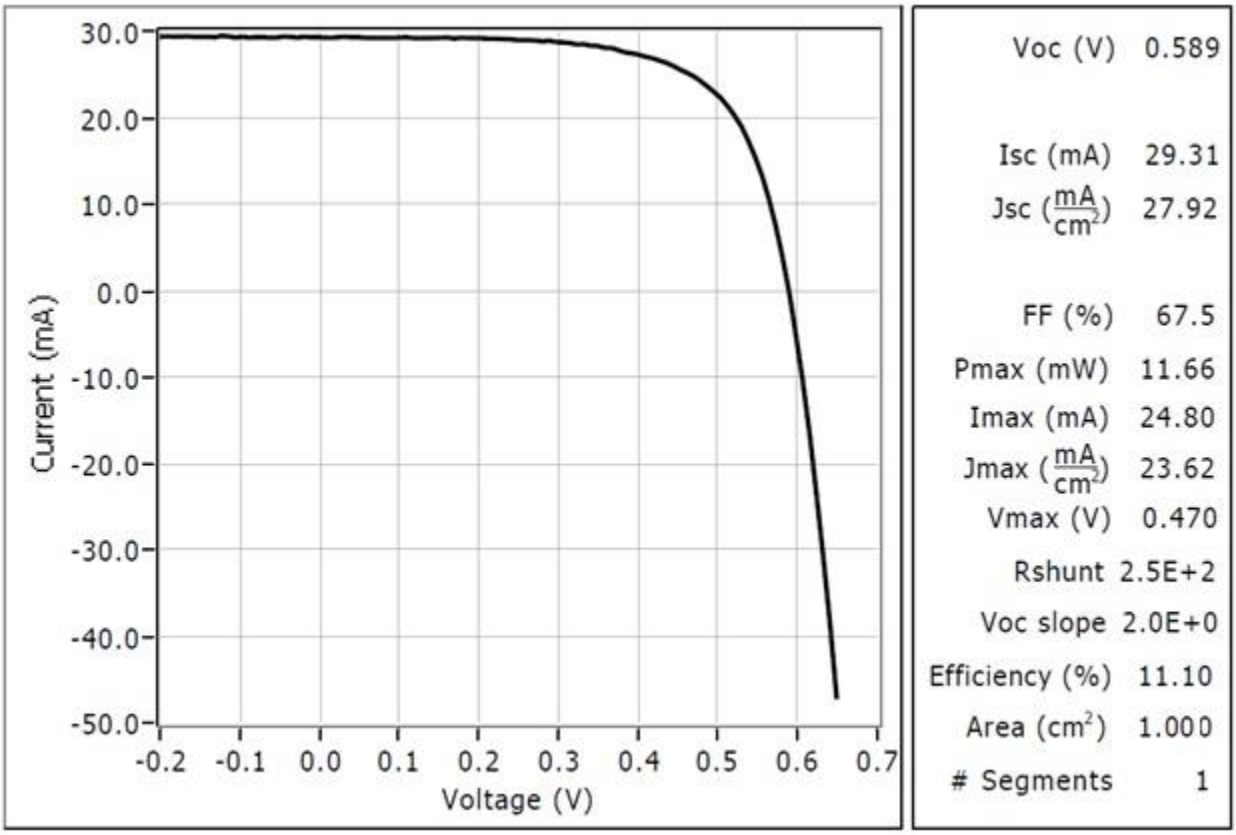

Fig 7.8: Performance report of the illuminated I-V analysis foe Ref-Cell

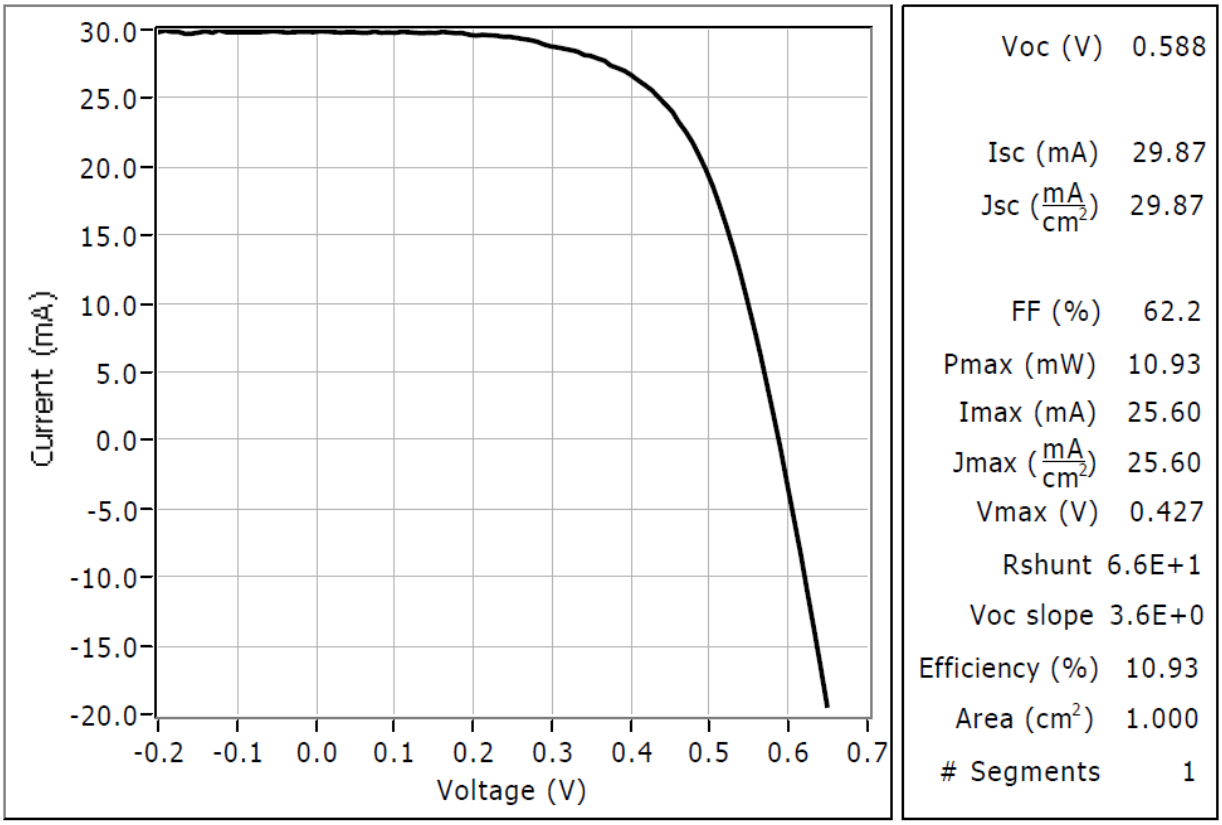

Fig 7.9: Performance report of the illuminated I-V analysis for NCOMP-GN-Cell

7.6 Conclusion

Two Solar cells with different back contacts (Ref-Cell and NCOMP-GN-Cell) are fabricated using 4 inch wafers. All the fabrication process were kept same and consistent except for the back contact material and deposition technique. Evaporated Al was used as the back contact for Ref-Cell while a newly developed graphene decorated nanocomposite (NCOMP-1wt%GN) was used as the back contact for NCOMP-GN-Cell. Cells were completely characterized using different techniques. Quantum efficiency results from NCOMP-GN-Cell were in an excellent agreement with the Ref-Cell while both cells showed slightly large ideality factors and low Fill Factors (FF). The large ideality factors and low Fill Factors (FF) are mainly related to the quality of the starting wafers specially their low carrier life time as well as front contact designs and process limitations. In general, the obtained performance results for both cells were very close to each other and both

devices showed almost equal efficiencies which is a very satisfactory achievement for a standard technology baseline development.

Chapter 8

Conclusion and Future Work

8.1 Conclusion

A screen printing process was established by designing masks compatible to both conventional metallic pastes as well as ECAs. To set up of the screen printer, a conventional highly conductive metallic paste was utilized to print on silicon wafers. The Printed patterns were characterized and results confirmed the proper printing quality. A microstructural analysis was done on the interface to investigate the curing profile. The presence of the three different interfaces Ag/thin glass layer/Si, Ag/thick glass layer/Si and Ag/Si confirmed that all the required chemical reactions and phase transformation have happened during the curing.

After establishing the screen printing process, different conductive nanocomposites (NCOMP-0.05wt%Ag and NCOMP-0.1wt%Ag) were synthesized using ECA as the matrix and silver nanowires as conductivity reinforce. Conductivity measurements revealed that addition of silver nanowires could decrease the resistivity and improve the conductivity of the nanocomposite (61% and 69% for adding 0.05wt% and 0.1wt% of Ag nanowires, respectively). Morphology characterization analysis confirmed the influence of silver nanowires in improving the electrical properties of the paste due to their breakage and scattering among silver flakes. SEM images as well as conductivity measurements also showed the conductive mechanism could be tunneling effect between small silver particles.

To reach to a comparable conductivity with conventional metallic pastes, two dimensional graphene sheets that have outstanding electrical and structural properties were used to improve the electrical properties of the ECAs. Different screen printable nanocomposites (NCOMP-1wt%GN and NCOMP-3wt%GN) were developed by introducing graphene nanopowders into the ECA to achieve higher conductivity. Material synthesis and curing profile are optimized to improve the electrical property of the developed nanocomposites and resulted in the highest boost in conductivity, over 2 orders of magnitude of ECA, bringing it comparable to metal pastes. A high degree of curing was obtained when the samples were sintered at 150°C for 10 min. The thermal stability of the NCOMP-GN nanocomposites was investigated using thermogravimetric analysis

and results showed that the temperatures for onset of decomposition in nanocomposites are higher than their corresponding T_g showing their excellent thermal resistance.

A detailed residual stress analysis was also conducted on all developed nanocomposites as well the metallic pasted printed substrates and results revealed that the amount of residual stress induced in substrates was much lower in nanocomposite and ECA printed wafers in comparison with metallic printed ones. Also, the amount of increase in residual stress by decreasing the wafer thickness was small in the case of using nanocomposite and ECA paste compare to the metallic paste. Moreover, it was shown that the amount of bending increased with decreasing the thickness of substrate in all three cases; however, it was much lower in nanocomposite printed wafers confirming that the new developed nanocomposites could be a promising alternative in screen printing metallization.

To evaluate the electrical properties of the highly conductive screen-printable graphene-decorated conductive nanocomposite at the interfaces, Effective Work Function (EWF) was introduced for the multiphase nanocomposite. Based on the theoretical studies on tunneling phenomenon and the potential barrier height measurement analysis on MOS devices, IV method was illustrated and used for the first time to measure the EWF of the multi-phase nanocomposite electrodes. The results were verified using two other techniques: UPS spectroscopy and TLM. The results from all measurements are in reasonable agreement however a small difference between the UPS technique and the other two exists. The difference is attributed to the heterogeneous nature of the nanocomposite and the difference in the sensitivity of each measurement method to the surface structure. These observations indicate that a possibly device-dependent effective value for the work function is worthy to be expected.

Finally, highly conductive screen-printable graphene-decorated conductive nanocomposite as well as evaporated Al was used as the back contact of two solar cells (NCOMP-GN-Cell and Ref-Cell). Solar cells were fabricated and completely characterized using different techniques. Quantum efficiency results from the NCOMP-GN-Cell were in an excellent agreement with the Ref-Cell while both cells showed slightly large ideality factors and low Fill Factors (FF) which is mainly related to the quality of the starting wafers specially their low carrier life time as well as front contact designs and process limitations. In general, the obtained similar performance results and efficiencies for both cells confirmed a very satisfactory achievement for a standard technology baseline development.

8.2 Future Work

- In this research a highly conductive nanocomposite was developed and it was utilized as the back contact in Solar cell. However, this material was not properly studied to be used as the front contact due to some process and equipment limitations which can be overcome in future.
- As a future work, the reliability of the cells could be analyzed by encapsulating one of the fabricated cells and performing reliability experiments such as:
    - Damp test
    - Thermal cycle test
    - Thermal shock test
- Another interesting application for the newly developed nanocomposite would be using at as an interconnection between cells in shingled module technology

Bibliography

[1]. Yadav, A. and Kumar, P. (2015) Enhancement in Efficiency of PV Cell through P&O Algorithm. International Journal for Technological Research in Engineering, 2, 2642-2644

[2]. K. Sopian, S. L. Cheow, S. H. Zaidi, "An overview of crystalline silicon solar cell technology: Past present and future", *Proc. AIP Conf.*, 2017.

[3]. Choubey, P.C., Oudhia, A. and Dewangan, R. (2012) A Review: Solar Cell Current Scenario and Future Trends. Recent Research in Science and Technology, 4, 99-101.

[4]. Srinivas, B., Balaji, S., Nagendra Babu, M. and Reddy, Y.S. (2015) Review on Present and Advance Materials for Solar Cells. International Journal of Engineering Research-Online, 3, 178-182.

[5]. https://en.wikipedia.org/wiki/Growth_of_photovoltaics

[6]. https://www.lesker.com/newweb/news/jpg/bpsolarsidhu_4-13-2010.pdf

[7]. L. Geerligs, C. Tool, R. Kinderman, I. Röver, K. Wambach, R. Kopecek, T. Buck, J. Libal, R. Petres, P. Fath, P. Sanchez-Friera, J. Alonso, M. Acciarri, S. Binetti, S. Pizzini, "N-type solar grade silicon for efficient p+n solar cells: Overview and main results of the EC NESSI project", Proceedings of the 21st european Photovoltaic Solar Energy Conference, pp. 566-569, Dresden, Germany, 2006.

[8]. S.B Rane, P.K Khanna, T Seth, G.J Phatak, D.P Amalnerkar, B.K Das, "Firing and processing effects on microstructure of fritted silver thick film electrode materials for solar cells", Materials Chemistry and Physics, Volume 82, Issue 1, 28 September 2003, Pages 237-245

[9]. M. M. Fouad, Lamia A. Shihata, El Sayed I. Morgan, "An integrated review of factors influencing the perfomance of photovoltaic panels", Renewable and Sustainable Energy Reviews, Volume 80, December 2017, Pages 1499-1511.

[10]. Dipankar Deb, Nisarg L. Brahmbhatt, "Review of yield increase of solar panels through soiling prevention, and a proposed water-free automated cleaning solution", Renewable and Sustainable Energy Reviews, Volume 82, Part 3, February 2018, Pages 3306-3313.

[11]. Morris, J. E., Lee, J., & Liu, J. "Isotropic Conductive Adhesive Interconnect Technology in Electronics Packaging Applications "5th Intemational Conference on Polymers and Adhesives in Microelectronics and Photonics, PP. 45-52, 2005.

[12]. Hilali, M. M., Nakayashiki, K., Khadilkar, C., Reedy, R. C., Rohatgi, A., Shaikh, A., et al. "Effect of Ag Particle Size in Thick-Film Ag Paste on the Electrical and Physical Properties of Screen Printed Contacts and Silicon Solar Cells". *Cell*, 5-11, 2005.

[13]. Wales, N. S., “Screen and Stencil Print Technologies for Industrial N-Type Silicon Solar Cells”,*Philosophy*, (March), 2008.
[14]. A. Hobby, “Screen printing for the industrial user”, DEK printing machines Ltd., 1997.
[15]. Y. Li, D. Lu, C.P. Wong, “Electrical Conductive Adhesives with Nanotechnologies, (Springer New York Dordrecht Heidelberg London, 2010.
[16]. http://www.kuroda-electric.eu/photosensitive-emulsions
[17]. Dobrzański, L. A., Musztyfaga, M., Drygata, A., Panek, P. “ Investigation of the screen printed contacts of silicon solar cells using transmission line model”, . *Manufacturing Engineering*, *41*, 57-65, 2010.
[18]. J. Hoornstra, A. Weeber, H. de Moor, W. Sinke, Proceedings of the 14th European Phovoltaic Science and Engineering Conference, Barcelona, Spain, pp. 823-826,1997.
[19]. Wales, N. S., “Screen and Stencil Print Technologies for Industrial N-Type Silicon Solar Cells”,*Philosophy*, (March), 2008.
[20]. J. F. Nijs, J. Sclufcik, J. Poortmans, S. Sivoththaman, and R. P. Mertens, IEEE Trans. on Elect. Dev. 46, 1948-1969,1999.
[21]. G. Schubert, F. Huster, and P. Fath, PVSEC-14, 441-442, 2003.
[22]. D. L. Meier and D. K. Schroder, IEEE Trans. on Elect. Dev. 31, 647-653, 1984.
[23]. J. Zhao, A. Wang, M. A. Green, Sol. Energy Mater. and Sol. Cells 66, 27-36, 2001.
[24]. O. Schultz, S.W. Glunz, 19th EU PVSEC,2004.
[25]. S. Wenham, Prog. in Photovoltaics, 1, 3-10, 1993.
[26]. J. H. Wohlgemuth, S. Narayanan, and R. Brenneman, Proc. 21st IEEE PVSC, 221-226, 1990.
[27]. L. Frisson, G. Cheek, R. Mertens, and R. Van Overstraeten, Commission Eur. Commun. Report. EUR, 1002-1006, 1984.
[28]. Honsbergand, C., Bowden, S., PVCDROM, 2010.
[29]. Narayanan, S., J. Zolper, F. Yun, S. R. Wenham, A. B. Sproul, C. M. Chong, and M. A. Green, , Twenty First IEEE Photovoltaic Specialists Conference, vol. 1, pp. 678-680, 1990.
[30]. Einhaus, R., E. Vazsonyi, J. Szlufcik, J. Nijs, and R. Mertens, Twenty Sixth IEEE Photovoltaic Specialists Conference, New York, NY, USA, pp. 167-170, 1451, 1997.
[31]. Stocks, M. J., A. J. Carr, and A. W. Blakers, Solar Energy Materials and Solar Cells, vol. 40, no. 1, pp. 33 - 42, 1996.
[32]. Fukui, K., Y. Inomata, and K. Shirasawa, Twenty Sixth IEEE Photovoltaic Specialists Conference, New York, NY, USA, pp. 1451, 47-50, 1997
[33]. Szlufcik, J., Sivoththaman, S., Nijs, J. F., Mertens, R. P., & Overstraeten, R. V. A. N“Low-Cost Industrial Technologies of Crystalline Silicon Solar Cells”,*Renewable Energy*, *85*(5), 711-730, 1997.

[34]. Doktorgrades, E. Rapid Thermal Processing of Silicon Solar Cells - Passivation and Diffusion, 2003.

[35]. A.G. Aberle, R. Hezel, Progress in low-temperature surface passivation of silicon solar cells using remote – plasma silicon nitride, Progress in Photovoltaics 5, 29-50, 1997.

[36]. S. Dauwe, A. Metz, and R. Hezel, "Low temperature rear surface passivation schemes for >20% efficient silicon solar cells", Proceedings of the 16th European Photovoltaic Solar Energy Conference, 2001.

[37]. Tao, Y., "Screen-Printed Front Junction n-Type Silicon Solar Cells", In Printed Electronics-Current Trends and Applications; Yun, I., Ed.; InTech: Rijeka, Croatia, 2016; Chapter 4.

[38]. G. Yao, PhD Thesis, University of New South Wales, 2005.

[39]. Sopori, B., Mehta, V., Rupnowski, P., Appel, J., Romero, M., Moutinho, H., et al., 17th Workshop on Crystalline Silicon Solar Cells & Modules: Materials and Processes, 2007.

[40]. C. Lin, S.P. Hsu, W.C. Hsu, "Solar Cells - Silicon Wafer-Based Technologies", edited by L. A. Kosyachenko, ISBN 978-953-307-747-5, PP. 93-110, 2011.

[41]. M. Ghannam, S. Sivoththaman, J. Poortmans, J. Szlufcik, J. Nijs, R. Mertens, R. Van Overstraeten, "Trends in industrial silicon solar cell processes", Sol. Energy, 59 (1997), pp. 101-110

[42]. Schneider, A., Gerhards, C., Fath, P., Bucher, E., Young, R.J.S., Raby, J.A., Carrol, A.F., 2002. Bow reducing factors for thin screen-printed mc-Si solar cells with Al BSF. In: Proceeding of the 29th IEEE photovoltaic specialists conference, New Orleans, LA, pp. 336339

[43]. S. Reber, A. Hurrle, A. Eyer, G. Willeke, "Crystalline silicon thin-film solar cells – recent results at Fraunhofer ISE", Sol. Energy, 77 (2004), p. 865875

[44]. J. R Lim, S Kim, H Ahn, H Son, G H Kang, "Analysis of the Bowing Phenomenon for Thin c-Si Solar Cells using Partially Processed c-Si Solar Cells", Energies 2019, 12, 1593; doi:10.3390/en12091593

[45]. Chen CH, Hu HT, Lin FM, et al., 2017. Residual stress analysis and bow simulation of crystalline silicon solar cells. Journal of Zhejiang University-SCIENCE A (Applied Physics & Engineering), 18(1):49-58. https://doi.org/10.1631/jzus.A1500279

[46]. P. Yoon, T. Baek, H. Chung, H.-E. Song, S. Shin, "Numerical simulation of bowing phenomenon in ultra-thin crystalline silicon solar cells", Sol. nergy, 105 (2014), pp. 705-714

[47]. Esfahani SN, Asghari S, Rashid-Nadimi S (2017) A numerical model for soldering process in silicon solar cells. Sol Energy 148:49–56

[48]. S. Kim, A. Shaikh, S. Sridharan, C. Khadilkar, T. Pham: "Aluminum Pastes for Thin Wafers", 19thEPVSEC, Paris (2004),1289 – 1291.

[49]. A. Schneider, C. Gerhards, F. Huster, W. Neu, M. Spiegel, P. Fath, E. Bucher, " AL BSF for thin Screenprinted Multi-crystalline Si Solar Cells", 17th EPVSEC, Munich (2001), 1568-1571.

[50]. Schiele, Y., Book, F., Seren, S., Hahn, G., Terheiden, B., "Screen-Printed Al-Alloyed Rear Junction Solar Cell Concept Applied to Very Thin (100 μm) Large-Area n-Type Si Wafers*", Energy Procedia* 2012, **27**, 460

[51]. Frisson, L., Lauwers, P., Mertens, R., Van Overstraeten, R., & Govaerts, R.,"Screen Printed Metallization of Silicon Solar Cells",Active and Passive Electronic Components, 7(1-3), 107-111, 1980.

[52]. Cheek, G., Mertens, R., Overstraeten, R., and Frisson, L. "Thick-Film Metallizatiora for Solar Cell Applications" IEEE Transactions On Electron Devices Ed-31, 602-609 1984.

[53]. Ballif C., D. M. Huljić, G. Willeke, and A. Hessler-Wysser,"Silver thick-film contacts on highly doped n-type silicon emitters: structural and electronic properties of the Binterface", Applied Physics Letters, Vol. 82, pp. 1878-1880, 2003.

[54]. M.M. Hilali and A. Rohatgi"A Review and Understanding of Screen-Printed Contacts and Selective – Emitter Formation", 14th workshop on crystalline silicon solar cells and modules, National Renewable Energy Laboratory,2004.

[55]. Schubert G., F. Huster, P. Fath, "Current Transport Mechanism in printed Ag Thick Film Contacts to an n-type Emitter of a Crystalline Silicon Solar Cell", Proceedings of 19th European Photovoltaic Solar Energy Conference, Paris, France, pp. 813-817, 2004.

[56]. Schubert G., F. Huster, and P. Fath,"Physical understanding of printed thick-film front contacts of crystalline Si solar cells—Review of existing models and recent developments", Solar Energy Materials & Solar Cells, Vol. 90, pp. 3399-3406, 2006.

[57]. Lin C.-H., S.-Y. Tsai, S.-P. Hsu, and M.-H. Hsieh,"Investigation of Ag-bulk/glassy- phase/Si heterostructures of printed Ag contacts on crystalline Si solar

[58]. S.M. Sze, Physics of Semiconductor Devices, second ed., Wiley, New York, 1981.

[59]. Hilali, M. M., Nakayashiki, K., Khadilkar, C., Reedy, R. C., Rohatgi, A., Shaikh, A., et al. "Effect of Ag Particle Size in Thick-Film Ag Paste on the Electrical and Physical Properties of Screen Printed Contacts and Silicon Solar Cells". *Cell*, 5-11, 2005.

[60]. Thuillier, B., Berger, S., Boyeaux, J. P., Laugier, A., Physique, L. D., Matibre, D., et al. Observation of mechanisms of screen printed contact FORMATION DURING HEAT TREATMENT ON MULTICRYSTALLINE SILICON SOLAR CELLS BY TRANSMISSION ELECTRON MICROSCOPY, 1-3, 2000.

[61]. Anizan, S., Leong, C. S., Yusri, K. L., Amin, N., Zaidi, S., & Sopian, K. "The Effect of Rapid Thermal Annealing Towards the Performance of Screen-Printed Si Solar Cell". American Journal of Applied Sciences, *8*(3), 267-270, 2011.

[62]. Doktorgrades, E."Rapid Thermal Processing of Silicon Solar Cells - Passivation and Diffusion", 2003.

[63]. J. Hoornstra, , G. Schubert, K. Broek, F. Granek, , C. LePrince, Conference Record of the Thirty-first IEEE Photovoltaic Specialists Conference, 1293, 2005.

[64]. I. Mir, D. Kumar. Journal of Applied Physics, 28, 362, 2008.

[65]. S. Xu, D. A. Dillard, J. G Dillard, Journal of Adhesion, 23, 235, 2003.

[66]. H. Wolfson. G. Elliott, Electrically Conducting Cements Containing Epoxy Resins and Silver, Patent No.: 2 774 747 (Dec. 1956).

[67]. J. Liu,Z. Lai, H. Kristiansen, Proceedings of the third international conference on adhesive joining and coating technology in electronics manufacturing, 1, 1998.

[68]. J.C. Jagt, P.J.M. Beris, G.F.C.M. Lijten,IEEE Trans Component PackagManuf Technol, B, 18 (2), 292, 1995.

[69]. J.C. Jagt, IEEE transactions on components, packaging, and manufacturing, 21(2), 215, 1998.

[70]. M. A. Lutz and R. L. Cole, Hybrid Circuits, 23, 27, 1990.

[71]. J. M. Pujol, C. Prud'homme, M. E. Quenneson, and R. Cassat, Journal of Adhesion, 27, 213, 1989.

[72]. S. Xu, "Evaluating Thermal and Mechanical Properties of Electrically Conductive Adhesives for Electronic Applications", Doctoral dissertation, 2002.

[73]. J. Lovinger, Journal of Adhesion, 10, 1, 1979.

[74]. P. Wong, D. Lu, L. Meyers, S. A. Jr. Vona, and Q. K. Tong, Proceedings 1st IEEE International Polymeric Electronics Packaging, 80, 1997.

[75]. D. Lu, Q. K. Tong, C. P. Wong, Packaging (Boston, Mass.), 22(3), 365, 1999.

[76]. G. R. Ruschau, S. Yoshikawa, R. E. Newnham, Journal Applied Physics, 72(3), 953, 1992.

[77]. D. Lu, C. P. Wong, Journal Of Adhesion, 20), 189, 2000.

[78]. H. Wu, X. Wu, J. Liu, G. Zhang, Y. Wang, Y. Zeng, " Development of a novel isotropic conductive adhesive filled with silver nano wires", Journal of Composite Materials. 1961, 2006.

[79]. L. Li, J. E. Morries, "electrical conduction models for isotropically conductive adhesives", Journal of electronics manufacturing, 5, 4, 289-296, 1995.

[80]. Li, Y., Moon, K.-sik J., & Wong, C. P. (n.d.). Nano-conductive Adhesives for Nano-electronics Interconnection.

[81]. Tan, F., Ã, X. Q., Chen, J., & Wang, H. "Effects of coupling agents on the properties of epoxy-based electrically conductive adhesives". *Journal Of Adhesion*, *26*, 406-413, 2006.

[82]. D. Lu, C. P. Wong, Advanced Packaging, 295, 1999.

[83]. Y. Li, K. Moon, A. Whitman, C. P. Wong, Packaging 29(4), 758, 2006.

[84]. Lee, H.-hsuen, Chou, K.-sen, & Shih, Z.-whie. "Effect of nano-sized silver particles on the resistivity of polymeric conductive adhesives",*Film*, *25*, 437-441, 2005.

[85]. Ye, L., Lai, Z., & Liu, J. "Effect of Ag Particle Size on Electrical Conductivity of Isotropically". *October*, *22*(4), 299-302, 1999.

[86]. Fan, L., Su, B., Qu, J., & Wong, C. P.,"Electrical and Thermal Conductivities of Polymer Composites Containing Nano-Sized Particles". *Components*, 148-154, 2004.

[87]. Jiang, H., Moon, K.-sik, Li, Y., & Wong, C. P. "Surface Functionalized Silver Nanoparticles for Ultrahigh Conductive Polymer Composites". *Society*, (3), 2969-2973, 2006.

[88]. M. Law, D. J. Sirbuly, J. C. Johnson, J. Goldberger, R. J. Saykally and P. Yang, "Nanoribbon waveguides for subwavelength photonics integration", Science 305, 1269, 2004.

[89]. R. C. Jin, Y.W. Cao, C. A. Mirkin, K. L. Kelly, G. C. Schatz and J. G. Zheng, "Photoinduced Conversion of Silver Nanospheres to Nanoprisms", Science 294, 1901 2001.

[90]. Y. Huang, X. F. Duan,Q.Q.Wei andC.M.Lieber, "Directed Assembly of One-Dimensional Nanostructure into Functional Networks", Science 291, 630, 2001.

[91]. Novák, I., Krupa, I., & Chodák, I."Electroconductive adhesives based on epoxy and polyurethane resins filled with silver-coated inorganic fillers". *Measurement*, *144*, 13-19, 2004.

[92]. Grujicic, M., & Cao, G. "A computational analysis of the percolation threshold and the electrical conductivity of carbon nanotubes filled polymeric materials", *9*, 4441 – 4449, 2004.

[93]. Tang H., Chen, X.F. and Lou, Y.X. "Conductivity Mechanism Study and Electrical Resistivity Calculation of Carbon Black filled Polymers", Polym. Mat. Sci. Eng., 12(2): 1–7, 1996.

[94]. Zhang, Z., Chen, X., Yang, H., Fu, H., & Xiao, F.. Electrically Conductive Adhesives with Sintered Silver Nanowires. *Packaging Technology*, 834-837, 2009.

[95]. Z. Zhang, X. Chen, F. Xiao, "The sintering behavior of electrically conductive adhesives filed with surface modified silver nanowires", Journal of Adhesion Science and Technology 25, 1465–1480, 2011.

[96]. S. Iijima, Iijima 1991, Helical microtubules of graphitic carbon.pdf, Nature. 354 (1991) 56–58

[97]. N. Saifuddin, A. Z. Raziah, and A. R. Junizah, "Carbon Nanotubes: A Review on Structure and Their Interaction with Proteins," Journal of Chemistry, vol. 2013, Article ID 676815, 2013.

[98]. K.S. Novoselov, a K. Geim, S. V Morozov, D. Jiang, M.I. Katsnelson, I. V Grigorieva, et al., Two-dimensional gas of massless Dirac fermions in graphene., Nature. 438 (2005) 197–200. doi:10.1038/nature04233

[99]. W. Choi, I. Lahiri, R. Seelaboyina, and Y. S. Kang, Synthesis of graphene and its applications: a review, Crit. Rev. Solid State Mater. Sci. 35, 52 (2010)

[100]. J. Lu, I. Do, L.T. Drzal, R.M. Worden, I. Lee, Nanometal-decorated exfoliated graphite nanoplatelet based glucose biosensors with high sensitivity and fast response., ACS Nano. 2 (2008) 1825–32. doi:10.1021/nn800244k.

[101]. A.S. Wajid, H.S.T. Ahmed, S. Das, F. Irin, A.F. Jankowski, M.J. Green, High-Performance Pristine Graphene/Epoxy Composites With Enhanced Mechanical and Electrical Properties, Macromol. Mater. Eng. 298 (2013) 339–347. doi:10.1002/mame.201200043.

[102]. L. Xuechun, L. Feng, The improvement on the properties of silver-containing conductive adhesives by the addition of carbon nanotube, in: Proc. Sixth IEEE CPMT Conf. High Density Microsyst. Des. Packag. Compon. Fail. Anal. (HDP '04), Ieee, 2004: pp. 382–384. doi:10.1109/HPD.2004.1346734

[103]. F. Marcq, P. Demont, P. Monfraix, a. Peigney, C. Laurent, T. Falat, et al., Carbon nanotubes and silver flakes filled epoxy resin for new hybrid conductive adhesives, Microelectron. Reliab. 51 (2011) 1230–1234. doi:10.1016/j.microrel.2011.03.020.

[104]. V.H. Luan, H.N. Tien, T.V. Cuong, B. Kong, J.S. Chung, E.J. Kim, et al., Novel conductive epoxy composites composed of 2-D chemically reduced graphene and 1-D silver nanowire hybrid fillers, J. Mater. Chem. 22 (2012) 8649. doi:10.1039/c2jm16910j.

[105]. Y. Oh, D. Suh, Y. Kim, E. Lee, J.S. Mok, J. Choi, et al., Silver-plated carbon nanotubes for silver/conducting polymer composites., Nanotechnology. 19 (2008) 495602. doi:10.1088/0957-4484/19/49/495602.

[106]. H. Wu, X. Wu, M. Ge, G. Zhang, Y. Wang, J. Jiang, Properties investigation on isotropical conductive adhesives filled with silver coated carbon nanotubes, Compos. Sci. Technol. 67 (2007) 1182–1186. doi:10.1016/j.compscitech.2006.05.010.

[107]. Y. Oh, K.-Y. Chun, E. Lee, Y.-J. Kim, S. Baik, Functionalized nano-silver particles assembled on one-dimensional nanotube scaffolds for ultra-highly conductive silver/polymer composites, J. Mater. Chem. 20 (2010) 3579–3582. doi:10.1039/c0jm00086h.

[108]. N.-W. Pu, Y.-Y. Peng, P.-C. Wang, C.-Y. Chen, J.-N. Shi, Y.-M. Liu, et al., Application of nitrogen-doped graphene nanosheets in electrically conductive adhesives, Carbon N. Y. 67 (2014) 449–456. doi:10.1016/j.carbon.2013.10.017.

[109]. E.E. Tkalya, M. Ghislandi, G. de With, C.E. Koning, The use of surfactants for dispersing carbon nanotubes and graphene to make conductive nanocomposites, Curr. Opin. Colloid Interface Sci. 17 (2012) 225–232. doi:10.1016/j.cocis.2012.03.001.

[110]. C. Bao, Y. Guo, L. Song, Y. Kan, X. Qian, Y. Hu, In situ preparation of functionalized graphene oxide/epoxy nanocomposites with effective reinforcements, J. Mater. Chem. 21 (2011) 13290–13298. doi:10.1039/c1jm11434d.

[111]. H. Kim, Y. Miura, C.W. Macosko, Graphene/Polyurethane Nanocomposites for Improved Gas Barrier and Electrical Conductivity, Chem. Mater. 22 (2010) 3441–3450. doi:10.1021/cm100477v.

[112]. R. Pasricha, S. Gupta, A.K. Srivastava, A facile and novel synthesis of Ag-graphene-based nanocomposites., Small. 5 (2009) 2253–9. doi:10.1002/smll.200900726.

[113]. X. Peng, F. Tan, W. Wang, X. Qiu, F. Sun, X. Qiao, et al., Conductivity improvement of silver flakes filled electrical conductive adhesives via introducing silver–graphene nanocomposites, J. Mater. Sci. Mater. Electron. 25 (2014) 1149–1155. doi:10.1007/s10854-013-1671-7.

[114]. Meschi Amoli, B., Trinidad, J., Hu, A. et al., Highly electrically conductive adhesives using silver nanoparticle (Ag NP)-decorated graphene: the effect of NPs sintering on the electrical conductivity improvement, J Mater Sci: Mater Electron (2015) 26: 590. doi:10.1007/s10854-014-2440-y

[115]. M. M. Hilali, J. M. Gee, & P. Hacke, Solar Energy Materials and Solar Cells, 91(13), 1228, 2007.

[116]. S. Kim, I. Lee, S. Eom, J. Park, S. Lee, K. Chai, J. Lee, Proceeding of 10th IEEE international conference on nanothecnology joint symposium

[117]. N. Bakhshizadeh, S. Sivoththaman, "New screen-printed metal paste options for PV manufacturing", MRS Proceedings, 1447, 2012.

[118]. D. Perloff, Sol. State. Electronics 20, 681 (1977).

[119]. D. Wang, J. Mater. Chem.A 3, 21907 (2015).

[120]. M. M. Hilali, J. M. Gee, & P. Hacke, Solar Energy Materials and Solar Cells, 91(13), 1228,2007.

[121]. Freeouf J L and Woodall J M, "Schottky barriers: An effective work function model", 1981*Appl. Phys. Lett.* **39** 727

[122]. E. H. Nicollian and J. R. Brews, MOS Physics and Technology (Wiley Interscience, New York, 1982).

[123]. D. K. Schroder, Semiconductor Material and Device Characterization (Wiley Interscience, New York, 1990)
[124]. Hüfner S. Photoelectron Spectroscopy: Principles and Applications, 2ed edn, (Heidelberg: Springer, 1996) pp.5-6. DOI 10.1007/978-3-662-03209-1
[125]. Hertz, H., 1887, Ann. Phys. (Leipzig) 17, 983.
[126]. R. Stratton, J. Phys. Chem. Solids 23, 1177 (1962)
[127]. J. G. Simmons, Appl. Phys. Lett. 35, 2655 (1964)
[128]. S. Zafar, C. Cabral, R. Amos, and A. Callegari, "A method for measuring barrier heights, metal work functions and fixed charge densities in metal/SiO2/Si capacitors," Appl. Phys. Lett., vol. 80, no. 25, pp. 4858– 4860, Jun. 2002.
[129]. S. Zafar, E. Cartier, and E. P. Gusev, "Measurement of barrier heights in high permittivity gate dielectric films," Appl. Phys. Lett., vol. 80, no. 15, pp. 2749–2751, Apr. 2002.
[130]. S. Zafar, V. Narayanan, A. Callegari, F. R. McFeely, P. Jamison, E. Gusev, C. Cabral, and R. Jammy, "HfO2/metal stacks: Determination of energy level diagram, work functions & their dependence on metal deposition," in VLSI Symp. Tech. Dig., 2005, pp. 44–45.
[131]. N. Klein and H. Gafni, "The Maximin Dielectric Strength of Thin Silicon Oxide Films," I€€€ Trans. Elec. Devices, D-13, pp. 281-289, Feb. 1966.DOI: 10.1109/T-ED.1966.15681
[132]. Helander, M. G., Greiner, M. T., Wang, Z. B. & Lu, Z. H. Pitfalls in measuring work function using photoelectron spectroscopy. Appl. Surf. Sci. 256, 2602–2605 (2010).
[133]. H. Murrmann, D. Widmann, "Current Crowding on Metal Contacts to Planar devices," IEEE Trans. Electron Dev. ED-16, 1022-1024, Dec. 1969.
[134]. C.Y. Chang, Y.K. Fang, S.M. Sze, "Specific contact resistance of metal-semiconductor barriers", Solid-State Electronics, Volume 14, Issue 7, July 1971, Pages 541-550
[135]. Ng KK, Liu R (1990) On the calculation of specific contact resistivity on ⟨100⟩ Si. IEEE Trans Electron Devices 37(6):1535–1537
[136]. E. Lipp, Z. Shahar, B. C. Bittel, P. M. Lenahan, D. Schwendt, H. J. Osten, and M. Eizenberg, J. Appl. Phys., vol. 109, no. 7, pp. 073724–1-073724-6, Apr. 2011.
[137]. YU, A.Y.C.: 'Electron tunneling and contact resistance of metal- silicon contact barriers', Solid-State Electron., 1970, 13, pp. 239- 247
[138]. Gee, J.M.,Garrett S. E. and Morgan W.P.., "SimplifiedModule AssemblyUsing Back-ContactSilicon SolarCells," 26'h IEEE Photo. Spec. Conf., pp. 1085-1088(1996).

[139]. Gee, J.M, Smith, D.D, , Garrett S. E, Bode M. D, and Jimeno J. C, “Back-Contact Crystalline-Silicon Solar Cells and Modules,” NCPV Program Review Meeting, S-11 Sepfember 1998, Denver, CO

[140]. Chapin, D.M., Fuller, C.S., Pearson, G.L. 1954, “A new silicon p-n junction photocell for converting solar radiation into electrical power”,J. Appl. Phys., Vol. 25, No. 5, p. 676

[141]. G. Beaucarne, “Materials challenge for shingled cells interconnection”, Energy ProcediaVolume 98, November 2016, Pages 115-124

[142]. D. Tonini, G. Cellere, M. Bertazzo, A. Fecchio, L. Cerasti, and M. Galiazzo, “Shingling Technology for Cell Interconnection: Technological Aspects and Process Integration”, Proceedings of the 33rd EUPVSEC, Amsterdam, The Netherlands, 2017, p. 38–41

[143]. J. Schmidt and M. Kerr, "Highest-quality surface passivation of low-resistivity p-type silicon using stoichiometric PECVD silicon nitride," SOLAR ENERGY MATERIALS AND SOLAR CELLS, pp. 585-591, 2001

[144]. Y. Park, V. Choong, Y. Gao, B. R. Hsieh, C. W. Tang,“Work function of indium tin oxide transparent conductor measured by photoelectr on spectroscopy”, Appl. Phys. Lett.1996, 68, 2699, 1996

[145]. Z. Gao, “Silicon Based Heterojunction Solar Cells and Photodetectors”, University of Waterloo, 2017.